WARSAW UNIVERSITY OF TECHNOLOGY

DISCIPLINE OF SCIENCE - CHEMICAL ENGINEERING /
FIELD OF SCIENCE - ENGINEERING AND TECHNOLOGY

Ph.D. Thesis

Nina Helena Borzęcka, M.Sc.

Numerical and experimental studies on kinetics of sol-gel transition during the synthesis of organoalkoxysilane-based alcogels

Supervisor
Jakub M. Gac, Prof. WUT, Ph.D., D.Sc.

WARSAW 2024

FUNDING

The research included in this thesis was funded by POB *Technologie Materiałowe* of Warsaw University of Technology within the Excellence Initiative: Research University (IDUB) programme.

I acknowledge to the COST Action CA18125 "*Advanced Engineering and Research of Aerogels for Environment and Life Sciences*" (AERoGELS), funded by the European Commission, for the granted Short Term Scientific Mission to perform the "*Investigation of hydrolysis and condensation reactions as the initial steps of the mechanism of MTMS based aerogel synthesis*" in the University of Debrecen, Hungary.

ACKNOWLEDGMENTS

I would like to express my sincere gratitude to everyone who supported this research, especially the supervisor of the thesis, professor Jakub Gac. Thank you for your supervision and the encouragement to modelling and simulations of sol-gel systems. Furthermore, I would like to thank Dr Bartosz Nowak, for encouraging me to study aerogels, your support and insightful discussions.

Moreover, I would like to express my gratitude to professor József Kalmar and Dr Attila Forgacs from University of Debrecen for your guidance with NMR experiments, as well as for the warm welcoming to your lab, even during the pandemic.

I would like to appreciate the help and support from my colleagues from Warsaw University of Technology and collaboration with BSc and MSc students: Rafał Pakuła, Aleksandra Pisarek, Robert Przewodzki and Paulina Witalewska.

At last, special thanks to people who supported me personally: my family and my beloved friends: Agata Kisielewska, Agnieszka Hahaj, Anna Rymuszka and Julia Bień. Thank you for your unwavering understanding and support.

To Ariadna Subotkiewicz

ABSTRACT

The objective of this thesis is to experimentally and numerically investigate the kinetics of sol-gel transition during the synthesis of organoalkoxysilane-based alcogels. The research aims at better understanding of the imposition of chemical reaction and physical phenomena occurring during sol-gel synthesis, such as miscibility gap driven phase separation, polymerization induced phase separation and Brownian motion-driven aggregation. The main goal was to establish analytically a description of gelation kinetics in organoalkoxysilane (methyltrimethoxysilane) based system and to develop a numerical model that would provide an insight into both formation kinetics and gel micro-structure evolution.

Nuclear magnetic resonance (NMR) was employed for methyltrimethoxysilane (MTMS) hydrolysis investigation. Experiments were designed to confirm the protonation as the first step of the hydrolysis reaction and to designate its rate constant. Subsequently, the hydrolysis conversion ratio could have been assumed as constant, and the focus of the thesis could be shifted to following the process of organoalkoxysililane gelation.

Further work resulted in development of analytical model describing condensation kinetics, and identification of dominant gelation mechanisms through the three distinguished phases of the process. The dependence of aerogel mass on time was obtained by two methods: spectrophotometrically and by collecting gelled product, deposited on a cellulose filter during the condensation reaction providing additional, quantitative understanding of the organoalkoxysilane gelation.

The thermodynamics of the sol-gel system based on chosen organoalkoxysilanes (methyltrimethoxysilane, vinyltrimethoxysilane and a mixture of co-precursors: methyltrimethoxysilane with dimethyldimethoxysilane) was investigated experimentally by preparation of ternary plots (precursor-solvent-antisolvent) and analysis of polymerization induced phase separation mechanisms – nucleation and growth (N&G) and spinodal decomposition (SD). Based on microstructure analysis performed with scanning electron microscopy, samples could be identified as obtained due to either metastable (N&G) or unstable thermodynamic conditions (SD). Additionally, a ternary plot is an excellent study case for the three-ingredient synthesis, as it provides information about each component's influence on the properties of final structure and kinetics of its formation. Moreover, a new method of analysis of condensation process registered spectrophotometrically was proposed, based on kinetics data interpolation and calculation of first derivative corresponding to the value of condensation rate.

An aggregation model was developed and implemented as a cellular automaton. Model's applicability was verified in terms of providing an insight into gelation kinetics and micro-structure evolution during the sol-gel transition. Based on the interpretation of Arrhenius equation, a novel method of correlation between experimental conditions and model parameters was proposed and validated with experimental data.

This thesis advances the current state of the art with an in-depth and comprehensive understanding of phenomena occurring during the sol to gel transition of organoalkoxysilanes, The results of this thesis enable better prediction of (aero)gels properties, as well as kinetics of gelation, which is especially important while upscaling the synthesis process. The main novelty of this thesis lies in validation of the aggregation model, which was not reported in literature before. Furthermore, dominant mechanisms occurring during condensation phases were identified, providing better understanding of the organoalkoxysilane-based system kinetics.

The presented work is complementary to the one of the current directions of chemical engineering – the synthesis of novel, porous materials that can be tailored for very specific applications, such as silica aerogels. This research proposes and validates the thorough description of organoalkoxysilanes gelation. The determination of kinetic parameters of hydrolysis and gelation is an important step towards upscaling and sustainable synthesis of aerogels.

Keywords: *sol-gel, organoalkoxysilanes, silica aerogels, gelation kinetics, cellular automaton, numerical modelling*

POLISH ABSTRACT (*STRESZCZENIE*)

Celem tej pracy jest eksperymentalne i obliczeniowe zbadanie oraz analiza kinetyki kondensacji podczas syntezy zol-żel wykorzystywanej do otrzymywania alkożeli na bazie organoalkoksysilanów. Badania celują w opracowanie lepszego opisu teoretycznego tego procesu, opartego na równoległej reakcji chemicznej polikondensacji i zjawisk fizycznych, takich jak rozdział faz napędzany luką mieszalności, polimeryzacją oraz agregacja cząstek na skutek ruchów Browna. Celem pracy było zarówno opracowanie analitycznego opisu kinetyki żelowania wybranego organoalkoksysilanu (metylotrimetoksysilanu) jak i modelu numerycznego dostarczającego informacji zarówno na temat kinetyki formowania jak I morfologii mikrostruktury żelu.

Wykorzystano metodę magnetycznego rezonansu jądrowego (NMR) do rejestrowania przebiegu reakcji hydrolizy w celu potwierdzenia protonacji jako jej mechanizmu oraz określenie stałej szybkości tej reakcji. Dzięki uzyskanym wynikom, stopień przereagowania po zadanym czasie prowadzania hydrolizy dla wybranych próbek mógł zostać uznany za stały oraz nie wpływający na przebieg drugiego etapu syntezy – kondensacji. Dzięki uzyskanym informacjom, dalsze badania mogły zostać skupione na kinetyce kondensacji organoalkoksysilanów, bez rozpatrywania wpływu stopnia przemiany reakcji hydrolizy na dalsze wyniki.

Dalsza część pracy zaowocowała opracowaniem modelu analitycznego opisującego kinetykę kondensacji oraz identyfikacją mechanizmów żelowania dominujących podczas trzech wyróżnionych faz tego procesu. Otrzymano analityczną zależność masy wyżelowanego

produktu od czasu, w oparciu o dwie eksperymentalne metody pomiarowe: spektrofotometryczną oraz opartą o filtracji żelującej zawiesiny.

Termodynamika układu opartego na wybranych organoalkoksysilanach (metyltrimetyksosilanie, winylotrimetyksosilanie oraz mieszaninie koprekursorów metylotrimetoksysilanu i dimetylodimetoksysilanu) została zbadana poprzez opracowanie trójskładnikowych diagramów fazowych i przeanalizowanie występujących mechanizmów rozdziału faz na skutek polikondensacji – nukleacji i wzrostu (N&D) lub rozpadu spinodalnego (SD). Na podstawie mikroskopowej analizy mikrostruktur próbki mogły zostać zakwalifikowane jako otrzymane na skutek metastabilnych (N&D) lub niestabilnych warunków termodynamicznych (SD). Dodatkowo, diagramy fazowe są bogatą bazą danych eksperymentalnych, dostarczającą informacji na temat wpływu każdego składnika na zmiany w układzie – strukturę (wysuszonych) żeli oraz kinetykę ich formowania. Zaproponowano nową metodę analizy procesu żelowania rejestrowanego spektrofotometrycznie, opartą na interpolacji i różniczkowaniu danych kinetyki w celu otrzymania zależności szybkości procesu od czasu jego trwania.

Model numeryczny agregacji cząstek został zaimplementowany poprzez automat komórkowy. Jego stosowalność została zweryfikowana pod kątem dostarczania informacji na temat kinetyki żelowania oraz procesu formowania mikrostruktury podczas przejścia zolu w żel. Zaproponowano nowatorską metodę korelacji parametrów modelu z warunkami syntezy w oparciu o równanie Arrheniusa i poddano walidacji przy użyciu danych doświadczalnych.

Przedstawiona praca uzupełnia obecny stan wiedzy na temat aerożeli i ich kinetyki kondensacji dzięki dogłębnemu i wyczerpującemu przeanalizowaniu zjawisk zachodzących podczas syntezy zol-żel materiałów na bazie organoalkoksysilanów. Wyniki umożliwiają lepsze przewidywanie właściwości (aero)żeli oraz kinetyki ich żelowania, szczególnie istotnej przy zwiększaniu skali procesu. Innowatorskość pracy opiera się na walidacji modelu opartego na agregacji cząstek, której nie odnotowano do tej pory w literaturze. Dodatkowo, identyfikacja dominujących mechanizmów występujących podczas poszczególnych faz kondensacji zapewnia lepsze zrozumienie kinetyki i termodynamiki układu kondensujących organoalkosysilanów.

Opisane badania są spójne z jednym z aktualnych kierunków inżynierii chemicznej – syntezy aerożeli krzemionkowych: innowacyjnych, porowatych materiałów, dopasowanych pod konkretne zastosowania. Ta praca proponuje i weryfikuje dokładny opis żelowania organoalkoksysilanów. Wyznaczenie stałych kinetycznych reakcji hydrolizy i kondensacji jest

istotnym krokiem w kierunku zrównoważonego sposobu prowadzenia syntezy zol-żel w większej skali.

Słowa kluczowe: *zol-żel, organoalkoksysilany, aerożele krzemionkowe, kinetyka żelowania, automat komórkowy, modelowanie numeryczne*

TABLE OF CONTENTS

LIST OF SYMBOLS

Latin alphabet symbols

A	Arrhenius constant; absorbance; integration constant in the Eq. 4.12
a	parameter in Eq. 6.9
A_A	constant in linearised Arrhenius equation
B	integration constant in the Eq. 4.12
C	integration constant in the Eq. 4.12
c	concentration; concentration of secondary particles (as a model parameter in the Chapter 6)
c_0	initial concentration of a precursor
c_b	concentration beyond the diffusion layer
c_i	interface concentration
c_{NH_4OH}	ammonia solution concentration
c_r	solubility
D	the diffusion coefficient
$\bar{d}$	mean diameter of a secondary particle
Da	Damköhler number
$\frac{dC}{dx}$	concentration gradient
$(dm/dt)_{max}$	maximum condensation rate
dt	time step
E	activation energy
$\bar{G_i}$	

J	total flux of the monomers
k	reaction rate
k_0	reaction rate constant
K_a	protonation constant
k_b	Boltzmann constant
k_{hydr}	observed hydrolysis reaction rate
L	linear dimension of the particles
m	mass
m_0	initial mass of the condensing (alcogel) product
m_s	mass of a dried sample
m_{sp}	single secondary particle mass
N	number of particles
n	moles number; number of dimensions; a parameter in Eq. 6.9
n_i	moles number of component *i*
n_j	moles number of component *j*
n_{MTMS}	number of moles of MTMS
n_{NH_4OH}	number of moles of ammonia base
P	pressure; probability
p	exponent in the gel formation equation (Eq. 4.5); probability rate
P_D	probability of motion (diffusion)
R	precusor/water mass ratio; universal gas constant
r	radius; $H_2O/MTMS$ molar ratio

$\bar{r}$	mean distance of each particle to the mass centre of an aggregate
Re	Reynolds number
T	temperature
t	time
t_1	time of the gelation first phase (nucleation of solid phase)
t_2	time of the gelation second phase (the intensive growth phase/microscopic phase separation(
T_g	temperature of gelation
t_g	time of gelation
V	volume
V_{ae}	volume of a dried sample
V_{al}	volume of an alcogel
V_s	volume shrinkage
V_{sp1}	single secondary particle volume
x	the distance from a particle surface

Greek alphabet symbols

α	parameter in equation Eq. 4.7
β	kinetic constant in Eq. 4.21
γ	surface energy
ΔG	Gibbs free energy
ΔG_{crit}	the critical free energy
ΔG^E	excess free Energy

ΔG^{IS}	free energy for ideal solution
ΔG^{mix}	mixing free energy
ΔH^{mix}	mixing enthalpy
ΔS^{mix}	mixing entropy
δ	diffusion layer width
ε	porosity
η	dynamic viscosity
λ	wavelength
μ_i	chemical potential of component *i*
v	molar volume
ρ_{env}	envelope density
ρ_s	structural density
σ	standard deviation

Other symbols

Đ	polydispersity index

LIST OF ABBREVIATIONS

AET WUT	Aerogel Engineering Team of Warsaw University of Technology)
APD	ambient pressure drying
CA	cellular automata/automaton
Cat.	catalyst
CTAB	cetrimonium bromide
DEM	discrete element method
DLA	diffusion limited aggregation
DLCA	diffusion limited cluster aggregation
DLR	German Aerospace Center
DMDMS	dimethylodimethoxysilane
FEM	finite element method
F-W	Finke-Watzky mechanism
IDUB	„Inicjatywa Doskonałości – Uczelnia Badawcza”
IUPAC	International Union of Pure and Applied Chemistry
LAMMPS	Large-scale Atomic/Molecular Massively Parallel Simulator
MeOH	methanol
MTMS	methyltrimethoxysilane
N&G	nucleation and growth
NA	nitric acid
NCBiR	„Narodowe Centrum Badań i Rozwoju”
NMR	nuclear magnetic resonance
PIPS	polymerization induced phase separation

PMSQ	poly(methylsilsesquioxane)
PP	primary particles
PS	phase separation
RLA	reaction limited aggregation
RLCA	reaction limited cluster aggregation
RVE	representative volume element
SCD	supercritical drying
SD	spinodal decomposition
SEM	scanning electron microscope/microscopy
SP	secondary particles
TD-D	the IV ternary diagram (for MTMS and DMDMS as coprecursors)
TD-M1	the I ternary diagram (for MTMS as precursor and variable base catalyst concentration)
TD-M2	the II ternary diagram (for MTMS as precursor and constant base catalyst concentration)
TD-V	the III ternary diagram (for VTMS as precursor)
TEOS	tetraethyl orthosilicate
TMOS	tetramethyl orthosilicate
UV-Vis	ultraviolet–visible
VTMS	vinyltrimethoxysilane
WUT	Warsaw University of Technology

1. AIM AND SCOPE OF THE THESIS

The aim of this thesis is to experimentally and numerically investigate the kinetics of sol-gel transition during the synthesis of organoalkoxysilane-based alcogels. This process is based on two chemical reactions (hydrolysis and condensation) and occurring parallelly imposition of physical phenomena, such as phase separation, Brownian motion, aggregation, which makes this system both complex and interesting. The importance of understanding this imposition lays in extraordinary potential of organoalkoxysilane-based alcogels. With an adequate drying procedure these gels can become aerogels – extraordinary, ultralight materials with outstandingly high porosity, sorption capacity and insulation properties. These properties make aerogels a perfect candidate to target even the most demanding applications, such as avionics or aerospace engineering. A comprehensive and in-depth understanding of formation of these materials could solve many challenges and issues that modern industry and technologies are facing nowadays.

The understanding of the sol to gel transition in an organoalkoxysilane-based system is provided by conducting a solid review of the state of the art within the introduction section and verifying four hypothesis stated as follows:

1st hypothesis

The hydrolysis of methyltrimethoxysilane in acidic conditions is based on a protonation mechanism, and this step occurs very

rapidly, thus, the time of conducting the hydrolysis reaction does not influence further stage of the sol gel synthesis: the gelation process and the gel-point value.

The 1st hypothesis may seem relatively straightforward – it is mostly based on verification of already known state of the art. Nevertheless, the rate of hydrolysis was unknown, verifying of the assumption, that hydrolysis is based on a very fast protonation was crucial for further research of this thesis and shifting its focus to the gelation kinetics.

2nd hypothesis

The condensation reaction of a chosen organoalkoxysilane (methyltrimethoxysilane) can be followed through UV-Vis spectrophotometric measurements, and the mass of the gel formed due to polycondensation reaction progress is directly proportional to the time-dependent absorbance of a sample. The condensation rate is dependent on the precursor and the base catalyst concentrations. Basing on the condensation kinetics curves, the gelation can be divided into three phases, and the dominant, mechanisms of these phases can be identified.

The second hypothesis verifies the applicability of the main experimental method (UV-Vis spectrophotometry) for following gelation kinetics. One of the main objectives of this research is to understand what are the steps during organoalkoxysilane gelation, and identify the dominant mechanisms during this process.

3rd hypothesis

With ternary diagrams based synthesis, one can establish the location of binode and spinode (the range of the metastable and unstable thermodynamic conditions on a ternary plot). Additionally, one can gain a comprehensive and extensive knowledge on impact of (i) molecular structure of precursor, (ii) chemical composition of the reaction mixture on: condensation kinetics, thermodynamic conditions as well as the aerogel morphology.

The third hypothesis is formulated in such a way to provide the most comprehensive and in-depth understanding of correlation between chemical composition of the initial synthesis mixture and thermodynamic conditions during gelation. This information is essential for understanding which phenomena are interfering with the gelation process and how the numerical model should be formulated. Working on this hypothesis provided also significant understanding of morphology, structural properties and kinetics in a system based on different chosen precursor, providing even more universal knowledge.

4^{th} hypothesis

A cellular automaton can be applied as a simplified representation of the gelation process, in particular for the aggregation of secondary organoalkoxysiloxane-based particles. The model parameters can be correlated with experimental synthesis conditions with the Arrhenius equation.

The fourth part of the research aims at creating a numerical model that could follow both gelation kinetics and structure evolution, preferably in a simplified and computationally efficient way. Among available modelling methods, an on-lattice aggregation model was chosen and implemented as a cellular automaton. The main challenge with this type of modelling is the fact, that this model does not provide a direct insight into process kinetics. This issue was solved by few authors, however the validity of this approach was never proven. The experimental verification of this approach is the most significant challenge and novelty within this thesis.

The four abovementioned hypotheses were to a certain extent verified in further chapters of this thesis. Any remaining questions, uncertainties, doubts and an outlook were discussed in the *Conclusions* section.

2. INTRODUCTION AND STATE OF THE ART

2.1 THE SOL TO GEL TRANSITION

The sol-gel process is a method of obtaining various solid, gel-derived materials, such as ceramic, xerogels and aerogels [1]. Innocenzi opens his book entitled "*The Sol-to-Gel transition*" with a sentence: *"Giving a clear and widely accepted definition in chemistry and physics is always a pretty difficult task, especially because the frontier of science is continuously moving"* [2]. Data presented in Fig. 1 proves that the number of publication with the keyword "sol-gel" has been rapidly increasing for over two decades (approximately since 1991) (data obtained from *Scopus* on 20th of May, 2024 [3]). Thus, it is one of the scientific fields for which providing a constant, solid definition can be a challenge. Nevertheless, when we speak about the sol-gel process or synthesis method we refer to a chemical-physical process of transition between sol system into a gel state, usually followed by the solvent evaporation, leading to obtaining dry, solid material. This process is of special relevance to the field of chemical engineering, and according to the data obtained from *Scopus*, this field is on the fifth position in terms of contributing to the state of the art (10.2% publications with keyword "sol-gel" were assigned to the field of chemical engineering).

International Union of Pure and Applied Chemistry (IUPAC) defines a sol as *"a fluid colloidal system of two or more components"* and a system can be considered as "colloidal" when we observe a state of subdivision, with dispersed molecules or polymolecular particles with at least one dimension roughly between 1 nm and 1 μm, or *"(...) a system discontinuities are found at distances of that order"* [4]. Innocenzi notices, that IUPAC definition excludes

the case of solid nanoparticles, which proves providing a consistent, coherent definition is a challenge [2]. Brinker and Scherer emphasise, that the size of dispersed particles in a sol has to be low enough, so the gravitational forces are negligible and particles can undergo Brownian diffusion. The interactions between particles are based on short-range forces, such as Van der Waals and electrostatic interaction due to surface charges or dipole moments. Additionally, it has to be noticed that in sols the medium is liquid, unlike aerosols, where particles are dispersed in a gas.

Further growth of dispersed in a sol phase, due to polycondensation or polymerization reactions leads to formation of a continuous solid phase – a gel. Quoting IUPAC definition: *"non-fluid colloidal network or polymer network that is expanded throughout its whole volume by a fluid"* [5]. Brinker and Scherer highlight that type of bonding responsible for solid skeleton formation can be covalent linking for polymer networks, in gelatine systems the network is formed due to an entanglement of chains and particulate gels are based on Van der Waals forces.

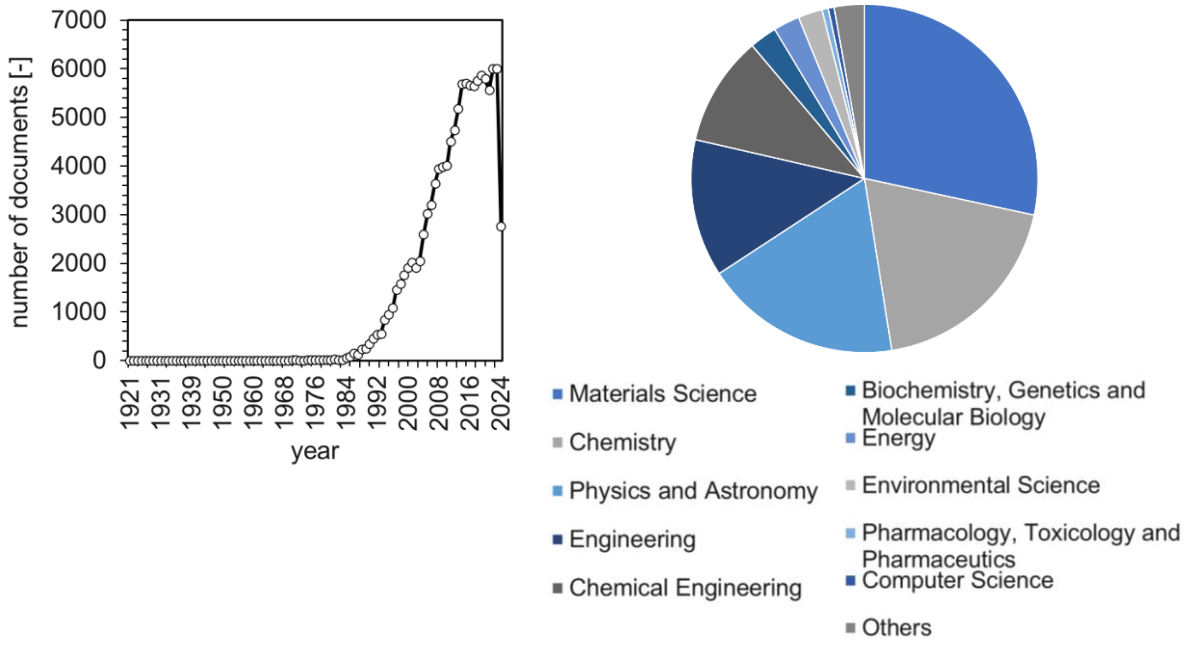

Fig. 1 (Left) Number of scientific publications per year with the keyword "sol-gel" ; (right) contribution of scientific fields to scientific publication with keyword "sol-gel" (data obtained from Scopus on 20th of May, 2024 [3]

The significance and interest of the scientific community in the sol-gel process lays in adaptability of this method for obtaining specific products with tailored properties. By controlling chemical composition of a synthesis, precursor selection and different post-processing of a gel we can obtain a very wide range of products: ceramics [6], glasses [7], coating films [8,9]. Depending on a material properties, it can find application in various fields,

such as adsorption [10], insulation [11], or as a catalysts supports [1,12,13], among many others. In Fig. 2 different routes of sol-gel technology are schematically presented [1].

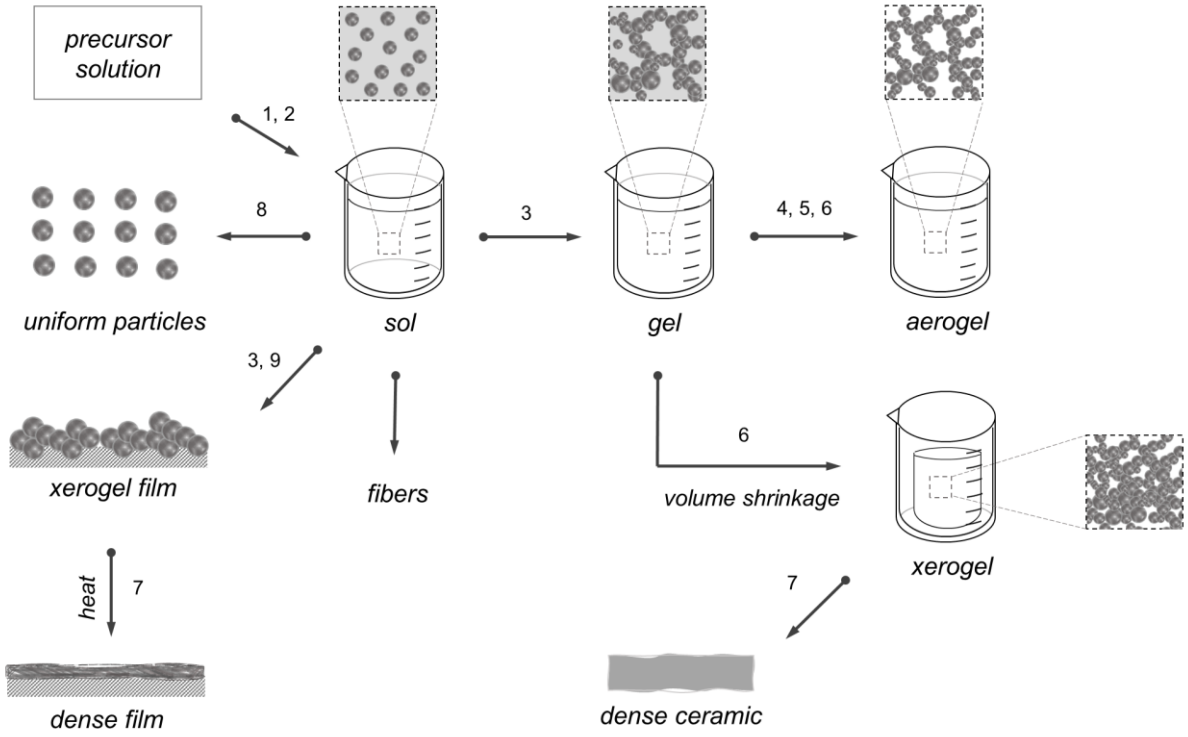

Fig. 2 Schematic routes of sol-gel technology (1 – hydrolysis, 2 – condensation, 3 – gelation, 4 – solvent extraction, 5 – aging, 6 – drying, 7 – sintering, 8 – precipitation, 9 – evaporation). Scheme based on [1]

2.1.1 Sol-gel processing of (organo-) alkoxysilanes

The sol-gel synthesis of silica gels can be based on an alkoxysilane or organoalkoxysilane precursor (or a mixture of co-precursors). This type of synthesis is the most related with the topic of this thesis.

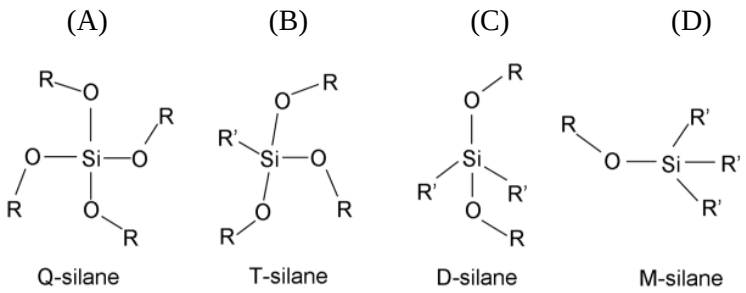

Fig. 3 Representative semi-structural formula of an organosilane (Q-silane) [14]

Alkoxysilanes include only alkoxy ($-OR$) groups (Fig. 3a), thus all the chemical substituent groups can be hydrolysed. In case of sufficient precursor to water molar ratio, the hydrolysis step leads to formation of fully hydrolysed precursor molecules ($Si(OH)_4$) (Eq. 2.1 and 2.3a). It affects the structure formation process of siloxane network in the next step – the condensation. Organoalkoxysilanes include alkyl substituent groups (R) (Fig. 3b and c). These groups do not participate during formation of oxygen bridges ($-O-$) between silica atoms and they remain within the molecular structure of the final gel network. The remaining alkyl groups determine properties of the skeleton in regards to such properties as hydrophobicity or flexibility. For example, a gel based on methyltrimethoxysilane as a precursor will maintain one methyl group ($-CH_3$) per silica atom within its structure, even after complete hydrolysis and condensation (Fig. 4).

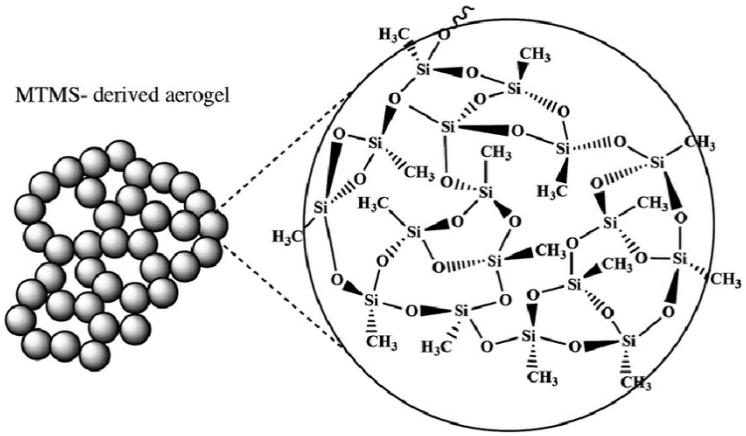

Fig. 4 Scheme of molecular structure of methyltrimethoxy-silane based (aero)gel [14]

$$\equiv Si - O - R_i + H_2O \rightarrow \equiv Si - OH + R_iOH \quad (2.1)$$

$$Si(OR)_4 + 4H_2O \rightarrow Si(OH)_4 + 4ROH \quad (2.2a)$$

$$(CH_3)Si(OR)_3 + 3H_2O \rightarrow (CH_3)Si(OH)_3 + 3CH_3OH \quad (2.2b)$$

There are many factors that can influence these reactions, such as pH value, type of used precursors, ratio of water to precursor, type of used solvent and its dilution, temperature and additives (surfactants and electrolytes, such as salts) [15].

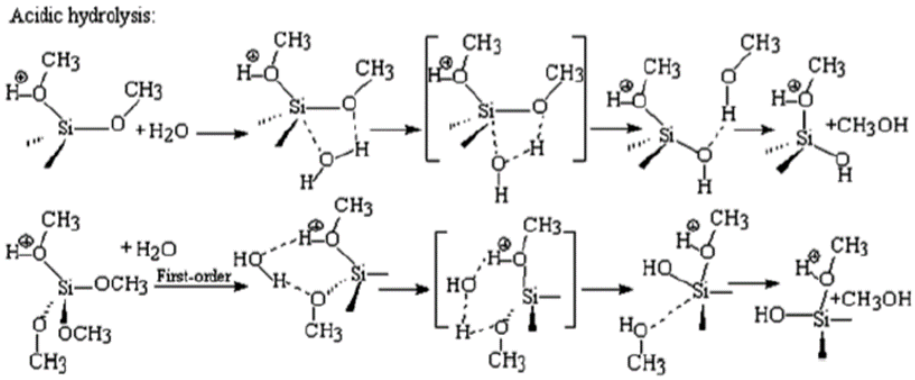

Fig. 5 The scheme of molecular mechanism for acidic pH value (pH < 7) [14]

The first step of the sol-gel process is the hydrolysis of the precursor. Depending on the pH value of the reaction mixture during this step the molecular mechanism of the chemical reaction will differ. Basing on the review paper of A.A. Issa et al. [14] the scheme of molecular mechanism for acidic pH value (pH < 7) is presented in Fig. 5. The mechanism in an acidic medium is the electrophilic addiction. The reaction is based on the fast protonation of an alkoxysilane. Subsequently, silicon atom becomes more electrophilic, which makes it more susceptible to the attack by water. Detachment of an alcohol molecule leads to the hydrolysis of the first alkoxy group within alkoxysilane (or organoalkoxysilane molecule). In alkaline conditions (pH >7) the mechanism is nucleophilic addition. The nucleophilic hydroxyl group attack the silicon atom in alkoxysilane.

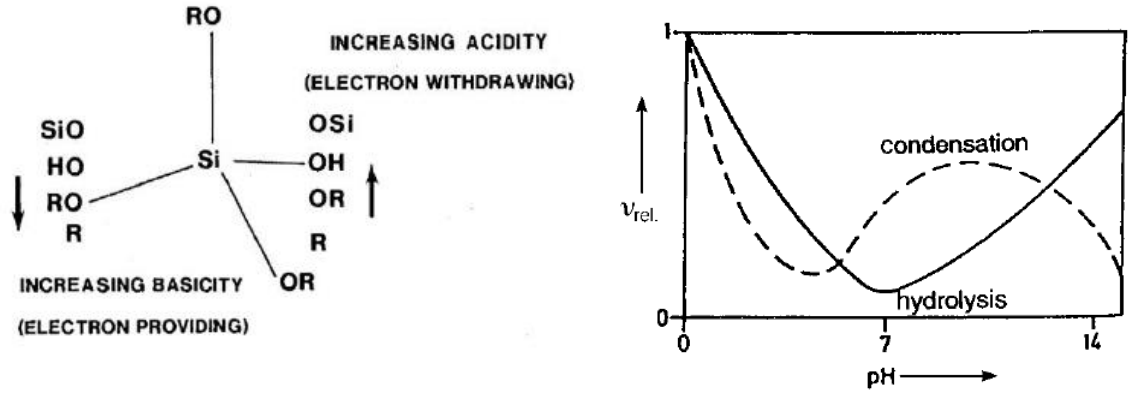

Fig. 6 The effect of substituents on basicity/acidity of a silanol (left), relative rate of condensation and hydrolysis reaction depending on the pH value (right) [16]

Zerda et al. reported that the protonated silanol preferably reacts (by the polycondensation reaction) with the least acidic silanol end groups (Fig. 6) which leads to less branched structures for condensation in acidic conditions. However, deprotonated silanol reacts with more acidic silanol groups which results in nicely branched clusters in the alkaline conditions [17–19].

The sol-gel process can be conducted as a one-step procedure usually in alkaline conditions, however, considering the above information, it can be easily understanded that the two-step synthesis, consisting of an acidic hydrolysis and alkaline condensation, seems as the most beneficial recipe, especially when the goal are nicely branched, highly porous structures. The relative rate of the reactions of hydrolysis and condensation dependence on the pH value is presented schematically in Fig. 6 [19]. The Fig. 7 shows reproduction of well-known in the sol-gel literature scheme, picturing the influence of pH conditions on condensation process pathways, such as formation of oligomers and creation of particle based open network [15].

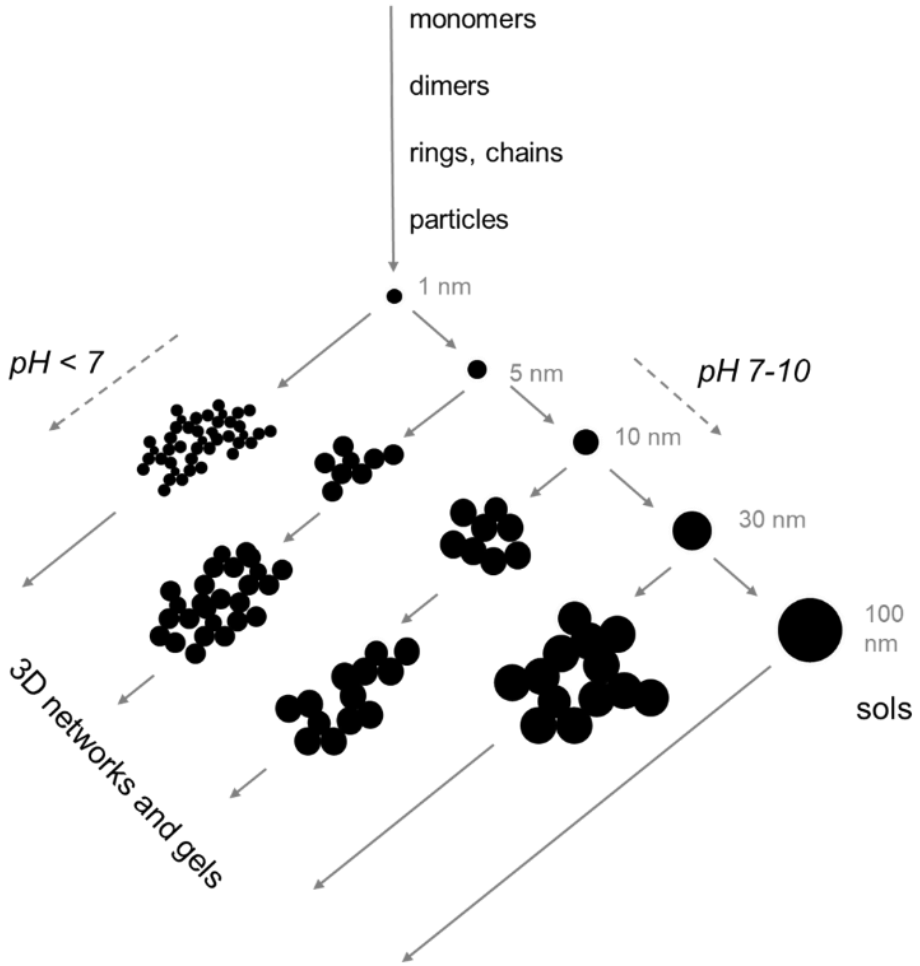

Fig. 7 Scheme of the pH influence on reactions pathways leading to formation oligomers, particles and network, based on [15]

2.2 THE PHASE SEPARATION DURING THE SOL-GEL TRANSITION

During the sol to gel transition the solidification of the precursor-based molecular network occurs. The morphology of this network based on the poly-condensed precursor molecules depends on the thermodynamic state of the system.

Partially miscible fluids (such as organoalkoxysilanes and water) do not mix in any proportions in any temperature. The range of the so called “miscibility gap”, showing the area chemical compositions exhibiting immiscibility, are presented in phase diagrams with binodal curves. Gibbs free energy (defined by Eq. 2.3, for not ideal system 2.4) in process ongoing under the conditions of constant temperature and pressure is equal to the maximum amount of non-volume expansion work in a closed system. Gibbs free energy is minimized when a system

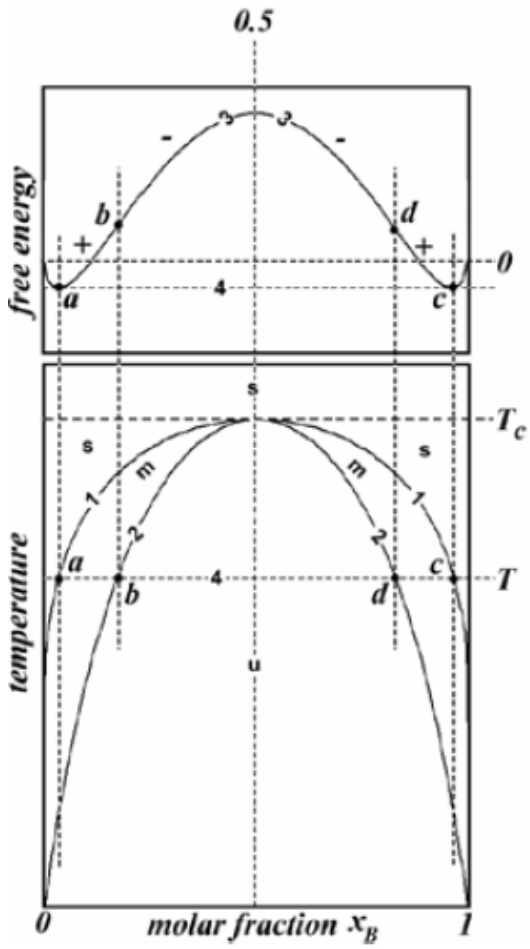

Fig. 8 Exemplary phase diagram and free energy diagram for 2 component system (polymer-solvent) [24]

reaches chemical equilibrium – chemical potentials of system ingredients are in a balance. Alternatively, we can interpret chemical potential as a partial molar Gibbs free energy, it informs, how the free energy of the system will change when i moles of the considered ingredient will be added (Eq. 2.5). Within the area defined by a binode, two types of thermodynamic conditions can occur – metastable (for the positive second derivative of the Gibbs free energy), unstable (for the second derivative less than zero) (Eq. 2.6-2.8). When the second derivative is equal to zero for a given chemical composition (molar fraction of a precursor of the polycondensation) the spinodal line is defined.

The phase separation due to polycondensation of precursor molecules (analogy to the polymerization of monomers) of gelling solutions is called a polymerization induced phase separation (abbreviated as PIPS) [20,21]. According to Flory-Huggins theory [22], Gibbs free energy of a system depends on the average degree of polymerization. When the polymer is dissolved in a solvent the Gibbs energy reaches its minimum and system remains homogenous. With progress of reactions (polymerization, polycondensation, cross-linking) the degree of polymerization increases. For sufficiently high values of this degree, two local minima occur (as presented in Fig. 8 on a free energy diagram [23]). As system tends towards minimising free energy, thus it decomposes into two individual phases with the polymer concentrations defined by the two local minima [24].

$$\Delta G^{mix} = \Delta H^{mix} - T\Delta S^{mix} \quad (2.3)$$

$$\Delta G^{mix} = \Delta G^{IS} - \Delta G^{E} \quad (2.4)$$

$$\mu_i = \overline{G_i} = \left.\frac{\partial G}{\partial n_i}\right|_{T,P,n_j} \quad (2.5)$$

$$\frac{d^2G}{dt^2} > 0 \quad \textit{metastable} \quad (2.6)$$

$$\frac{d^2G}{dt^2} < 0 \quad \textit{unstable} \quad (2.7)$$

$$\frac{d^2G}{dt^2} = 0 \quad \textit{spinodal curve} \quad (2.8)$$

The motion of droplets (or fluid elements) resulting in the phase separation has a rather deterministic than stochastic character [24,25] arising from the interfacial tension gradient – Marangoni force. This behaviour of a system – spinodal decomposition - can be described by the Cahn-Hilliard equation [26–28].

The phase separation can also occur according to nucleation and growth mechanism [29–33]. The classical theory [29] is well known, however for porous materials variation from classical nucleation pathways can be observed. Two types of nucleation can be distinguished – homogenous and heterogenous, depending on whether nuclei form uniformly within the parent phase, or at inhomogeneities, such as uneven surfaces, interphase between immiscible components, impurities and so on. The free energy of a nanoparticle is a sum of the surface free energy and the bulk energy. Differentiating Gibbs energy by a particle radius, and setting the derivative value to zero ($d\Delta G/dr = 0$) allows to designate the critical radius of a nuclei, which is minimum size of a stable particle, thus a particle of this size cannot longer redissolve. The rate of nucleation can be described according to Arrhenius equation (Eq. 2.9):

$$\frac{dN}{dt} = A\ exp\left(-\frac{\Delta G_{crit}}{k_b T}\right) \tag{2.9}$$

where N is the number of particles, t – time, A – Arrhenius constant, ΔG_{crit} – the critical free energy (value of energy needed to form stable particles within a solution), k_b – Boltzmann constant and T is the temperature.

Nuclei are a seed for the further growth. Once the particles reach their stable size, their further growth can be a consequence of two steps: monomers diffusion to the particle's surface and the surface reaction. This type of classical growth can be described by Fick's first law (2.10):

$$J = 4\pi x^2 D \frac{dC}{dx} \tag{2.10}$$

where J is the total flux of the monomers, D is the diffusion coefficient, r is the radius of a particle and x is the distance from a particle surface. Around a particle surface we observe a decrease of concentration of monomers, due to a surface reaction. This area is called the diffusion layer.

Integrating Eq. 2.10 for an assumed system with concentration c_i at the interface (particle surface – solution) which corresponds to $x = r$, and concentration c_b beyond the diffusion layer ($x = r + \delta$) leads to the following solution:

$$J = \frac{4\pi D r(r+\delta)}{\delta}(c_b - c_i) \tag{2.11}$$

The Damköhler number is defined as $Da = 2\gamma vk/Dk_bT$, where γ denotes the surface energy, v - molar volume and k - the surface reaction rate. The physical interpretation of this dimensionless number is the ratio of the reaction rate to the diffusive mass transport rate. The value of the Damköhler number indicates what is the limiting part of the overall process – whether it is the diffusion of monomers to a particle's surface ($D \ll 1$), or the surface reaction itself. For the diffusion limited process, the evolution of a particle size can be described by Eq. 2.12a, and in the case of the reaction limited process – Eq. 2.12b. Neutral case, when neither reaction or diffusion is the limiting factor is described by Eq. 2.13:

$$\frac{dr}{dt} = \frac{Dv}{r}(c_b - c_r) \qquad (2.12a) \qquad \frac{dr}{dt} = kv(c_b - c_r) \qquad (2.12b)$$

$$\frac{dr}{dt} = \frac{Dv(c_b - c_r)}{r + D/k} \qquad (2.13)$$

where c_r is the solubility of the particle. In case of the above considerations it was assumed that the reaction rate is independent on the particle size, however, the solubility of nanoparticles is strongly dependant on their size. The extra chemical potential of a spherical particle can be described according to Gibbs-Thomson relation $c_r = c_b exp(2\gamma v/rk_bT)$.

The size distribution of the particles is an important aspect, determining the kinetics of the growth, and also the properties of the final product. The differences between sizes of particles in a system can be caused by the effect of Ostwald ripening. The particles' growth rate is dependent on their solubility (c_r), which is dependant on this size according to the abovementioned Gibbs-Thomson relation. The smaller particle are, the better is the solubility and they possess higher surface energy. Thus, below a certain critical size corresponding to the critical value of the Gibbs energy (value of energy needed to form stable particles within a solution), they are more likely to redissolve. Redissolving of smaller particles provides both time and resources (monomers) for the bigger particles to continue their growth [34–36]. The opposite process, when the bigger particles redissolve and small particles grow at their expense, is called a digestive ripening [29,37].

In the 1950, V.K. LaMer divided the synthesis of sulphur sols into formation of monomer and subsequently a sol [38]. Basing on his description, the nucleation and growth process can be divided into three steps [39,40]. The first step is a rapid increase of free monomers concentration. This step is followed by a "burst-nucleation" which leads to drastic decrease of the monomer concentration in a solution. In this moment, the nucleation rate is assumed as an effectively infinite. Due to the sudden drop of the concentration, there is a pause in the nucleation process. The third step is a diffusion controlled growth based on the remaining

free monomers in the solution. This approach basically assumes the nucleation and growth as not simultaneous, but rather sequential steps.

Quite an opposite approach is the two-step Finke-Watzky mechanism [41]. In this theory, both nucleation and growth occur simultaneously. The authors proposed a formula describing the kinetics, which has been proven a good approximation in some metal systems, such as platinum, silver or gold nanoparticles formation [42–44]. The F-W mechanism mimics the sigmoidal kinetic curve, however it does not provide a description of particle size or the number of the nucleation events [45].

The formed particles can undergo coalescence (with no preference of attachment direction) or oriented attachments, as suggested by Li et al. due to Coulombic or Van der Waals interactions [29,46].

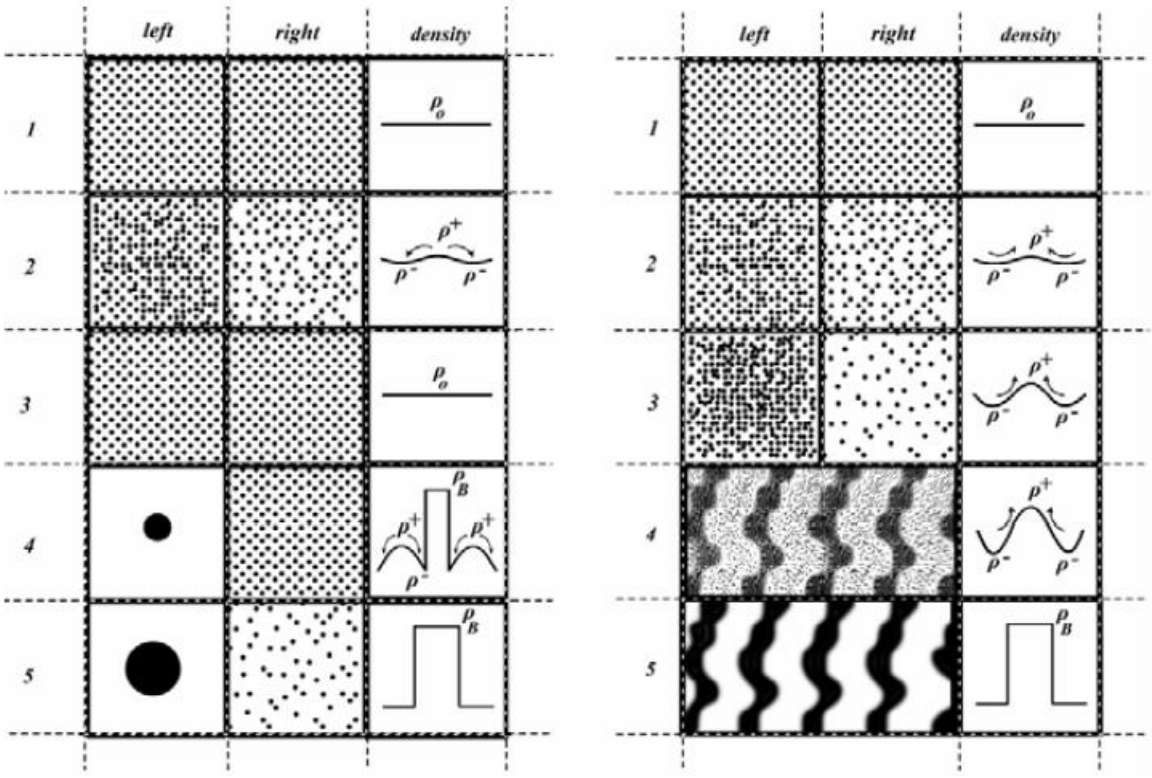

Fig. 9 Scheme of density fluctuations in a metastable (left) and an unstable (right) system [23]

Favvas et al. explained the correlation between density fluctuations in a metastable system (which leads to nucleation) and unstable system with schematic representation which is presented in Fig. 9. The first two columns represent a two adjacent representative elements of a solution (black dots represent monomers), and the third column represents a density profile at a given stage of a phase separation process. For the metastable system (presented in Fig. 9) the first three rows schematically represent a small fluctuation of density (or a monomer

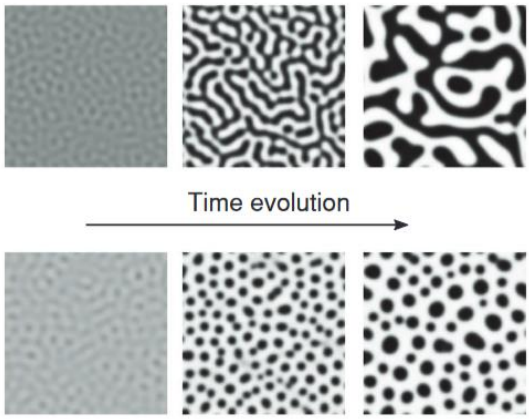

Fig. 10 Spinodal decomposition in concentrated (upper) and dilluted (bottom) system [24]

concentration). The system tends towards balance of chemical potentials of the ingredients, thus a diffusion of monomers occurs to even out the concentration (density) gradient. In case of a large density fluctuation, as a system is in metastable thermodynamic conditions, the gradient cannot be even out, and a formation of nucleus occurs (fourth and fifth row in the scheme Fig. 9).

In the case of a thermodynamically unstable system, any density fluctuation leads to the spinodal decomposition. Small fluctuation leads to a change in a density profile, however the mass transfer (diffusion) proceeds uphill, according to the Marangoni effect. As system tends towards minimising the free energy and balance of the components' chemical potentials, thus it decomposes into two individual phases with the polymer concentrations defined by the two local minima defined on the phase diagram (Fig. 8) [24].

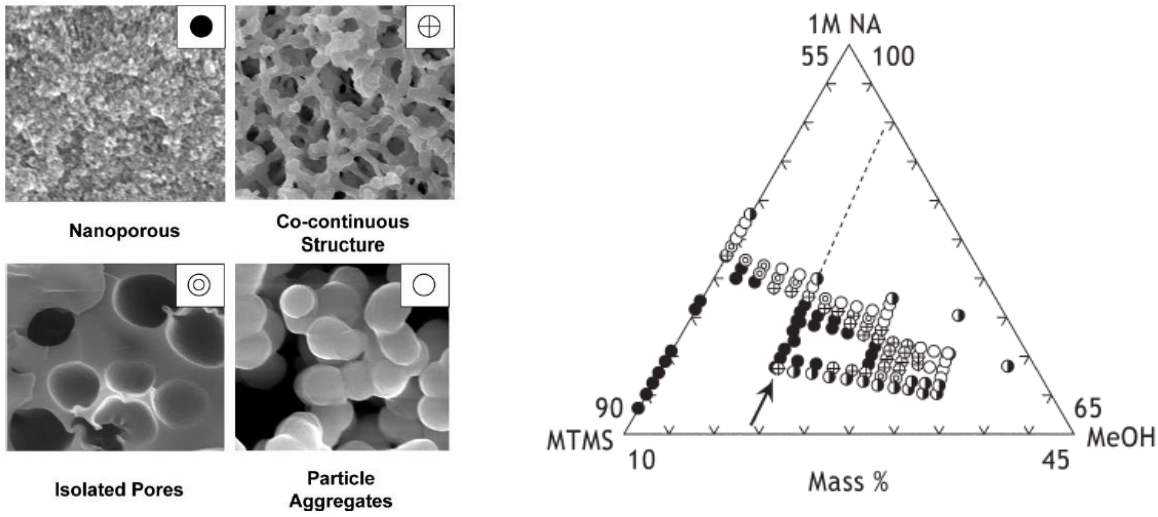

Fig. 11 Nakanishi's et. al studies on methyltrimethoxysilane (MTMS) ternary system with methanol as solvent (MeOH) and nitric acid (NA) as a catalyst [49]

This process can be described by the Cahn-Hillard equation [27] which correlates a given component gradient with the diffusion coefficient and chemical potentials. This equation can be solved analytically [26], however it can be also coupled with the Navier-Stokes equation and solved by means of e.g. Lattice-Boltzmann method [28,47,48]. A visualisation of this process is shown in Fig. 9 [24]. There is a comparison of phase separation progress depending on the concentration of the monomers. Spinodal decomposition in a concentrated

system will result in a co-continuous structures, while SD in diluted system will result in particles (Fig. 10 [24]). These structures and their location in an organoalkoxysilane-based system was studied by Nakanishi et al. [49]. The observed types of structures and their location on a ternary plot are presented in Fig. 11. Similar organoalkoxysilane-based ternary plots were used by other authors studying correlation between initial chemical composition of a reaction mixture and final system's properties, such as Itagaki et al. [50], Kaji et.al [21], Ivanov and Mazhorova [51] or Urikanu et al. [52].

It can be concluded, that the chemical composition of a sol-gel system is a crucial factor deciding on overall thermodynamics of a system, rate of the structure formation and morphology of the final product.

2.3 AEROGELS

Aerogels are a very diverse group of porous materials and very dynamically evolving field of research. According to data presented in Fig. 12 we can see the sudden growth of interest in this research was constantly growing since the nineties. Each year, the number of publications per year is constantly growing (data obtained from Scopus on 20th of May, 2024 [3]). The number was also analysed regarding the specific fields of research, and the Scopus data indicates high significance of these materials for the materials science (25.8%), chemistry (19.7%) physics and astronomy (13.5%) publications. The field of chemical engineering provides the 4th highest contribution to aerogels' state of the art (12.7%).

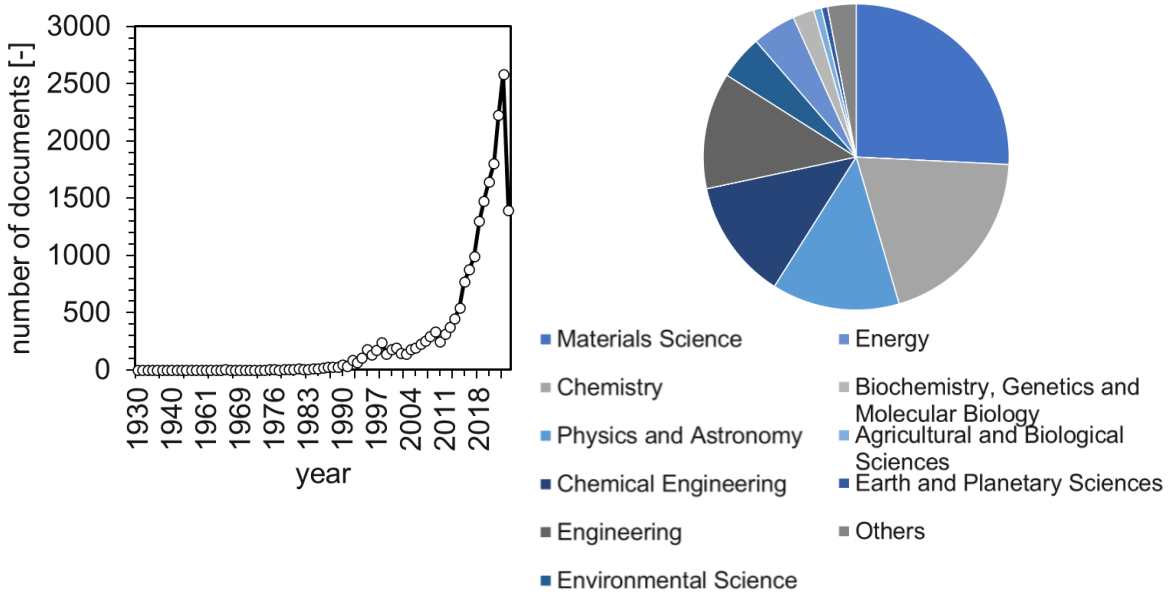

Fig. 12 (Left) Number of scientific publications per year with the keyword "aerogel" ; (right) contribution of scientific fields to scientific publication with keyword "aerogel" (data obtained from Scopus on 20th of May, 2024 [3]

The presented above data proves the ongoing, dynamic development of these materials, as well as a very interdisciplinary interest in aerogels. Due to these facts and various scientific backgrounds of researchers contributing to these field, creating a universal and consistent definition and terminology can be a challenge. Stephen A. Steiner III and Alain C. Pierre elaborate on this challenge in the Aerogel Handbook chapter "The story of Aerogel" and provide a minimum definition, which was well accepted in the community: *"aerogels are solid-phase, porous materials that possess a high degree of porosity arising from a finely divided pore structure"* [53]. However, the interpretation of the phrases as "high degree" or "finely divided" is left to individual interpretations. There is a definition provided by IUPAC (International Union of Pure and Applied Chemistry) which says aerogels are a gel comprised of a microporous solid in which the dispersed phase is gas, which is not entirely accurate [54].

Even the name "aerogels" used to raise a controversy in the community. For many years, aerogels by definition could be obtained only due to the supercritical drying of a gel. However, this method initially generated high costs of the process, and scientists devoted to developing methodology for other gel drying techniques that would allow to obtain highly porous final structures. An alternative method is ambient pressure drying, but these aerogels for many years has been referred as "xerogels". Another alternative is freeze drying technique, but then, many scientists would call the product a "cryogel". Many scientists work on these methods parallelly [55–58] . Over the years, the aerogel scientific community became not as strict with the semantics. An alternative definition to the one provided by the Stephen A. Steiner III in the Aerogel Handbook, a little more detailed one but still very flexible and open for various drying techniques, was the one proposed by Carlos García-González: *"aerogels can be defined as solid, lightweight and coherent open porous networks of loosely packed, bonded particles or nanoscale fibers, obtained from a gel following the removal of the pore fluid without significant structural modification"* [59].

Within this thesis, the term "aerogel" is used in regards to a material obtained due to drying of a gel (also with other methods than supercritical drying), in such a way to maintain relatively high porosity of an original gel structure. No strict definition of the "high porosity" value was applied, as this thesis describes investigation of the sol-gel processing of organoalkoxysilanes. Aerogels were simply a target final product of the gelation process, but it was their gelation kinetics which was the main focus of this study.

There are different types of aerogels, which are distinguished based on the used precursors. The main types 5 of aerogels are:

1. Inorganic aerogels (based on metaloxides or silica);

2. Organic-inorganic hybrid silica aerogels (based on organoalkoxysilanes);
3. (Bio)polymer aerogels (for example cellulose or alginate aerogels);
4. Phenolic aerogels (eg. resorcinol-formaldehyde based aerogels);
5. Carbon aerogels.

A picture of an exemplary aerogel macrostructures is presented in Fig. 13a, due to courtesy of German Aerospace Center (Institute of Materials Research, Department of Aerogels and Aerogel Composites, the authors: Nina Borzęcka, Adrian Denfeld, Ameya Rege). The aerogel was obtained based on tetraethyl orthosilicate (an alkoxysilane), indicates porosity of 95% and was obtained with supercritical drying resulting in 2% volume shrinkage. However, organoalkoxysilanes can be used to obtained flexible samples that can endure ambient pressure drying without high volume shrinkage, and very often they indicate better stability comparing to brittle, pure alkoxysilane aerogels. An exemplary organoalkoxysilane (methyltrimethoxysilane) based sample is presented in Fig. 13b.

The form of aerogel macrostructure depends mostly on the targeted application and preparation method, but for most types of aerogels we can obtain monoliths, composites (for example aerogel reinforced with different material [60–63]), sheets or beads.

(A) (B)

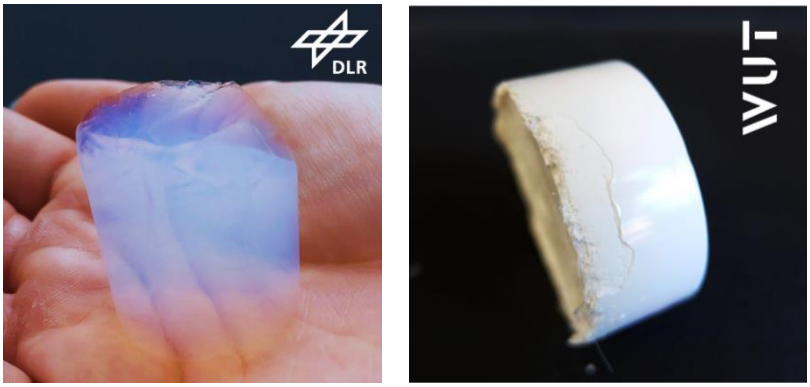

Fig. 13 Exemplary aerogels macrostructures. (A)alkoxysilane based aerogel, courtesy of German Aerospace Center, Institute of Materials Research, Department of Aerogels and Aerogel Composites (the authors: Nina Borzęcka, Adrian Denfeld, Ameya Rege). (B) organoalkoxysilane (methyltrimethoxysilane) based aerogel

The type of an aerogel system influences the description of the microstructure. The morphology strongly depends on the chemical composition of a reaction mixture, as the composition determines the thermodynamics of the polymerization induced phase separation (PIPS). For certain systems (for example organoalkoxysilanes) the PIPS can occur parallelly to the classic liquid-liquid phase separation (between precursor and anti-solvent),

according to the miscibility gap on the phase diagram for the investigated system. However, in most cases the morphology of aerogels resembles one of the three cases: particle based, fibrillar or cellular (Fig. 14).

The particle aggregates type of structure, very often in the literature is referred to as a hierarchical [64–66]. For years it was assumed, that the final particle matrix is formed due to polycondensation reactions between precursor molecules, which leads to formation of oligomers. According to the nucleation theory described in the previous section, above critical size the particles become stable and cannot be redissolved, and their growth starts to occur. At certain point, it was assumed, that these primary particles stop growing, and start aggregating with each other to form secondary particles – the final particles that can be seen in SEM pictures. However, this theoretical explanation was never completely proven, and it leaves certain questions: when and why the primary particles growth stops? Furthermore, for certain systems, for example alkoxysilane-based aerogels the particles can be as small as few nanometers, while precursor molecule, let's use tetraethyl orthosilicate as an example, has a size of few angstroms, which creates doubts about the hierarchy of the structures. Furthermore, for certain cases, spinodal decomposition can be more likely mechanism of particles formation, which is followed by their aggregation. In this case, is difficult to speak about hierarchical structure. Despite some initial doubts, this theory was adapted for this thesis, and further doubts will be discussed in the conclusions.

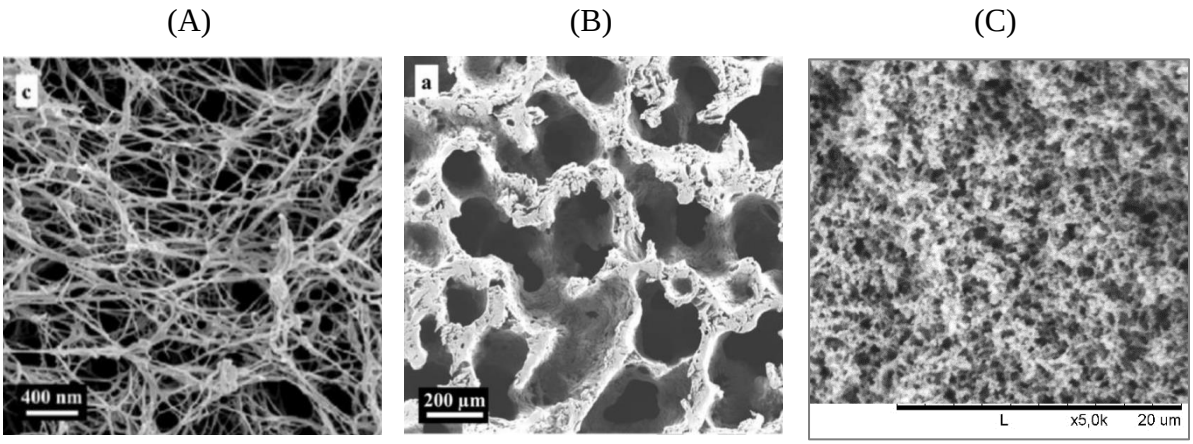

Fig. 14 Exemplary aerogels micro-structures (a, b) cellulose fibrillar and cellular structures (pictures from [67]), (c) organoalkoxysilane based very fine particle structure (own results)

This type of highly porous structure results in outstanding structural properties. First of all, such materials are incredibly light, which makes them very interesting for example for aviation and aerospace applications. The porosity also results in well-developed surface area and storage capacity, which makes aerogels perfect candidates for sorbents, active components

carriers and catalysts supports. Additionally, some aerogels, for example titanium-based aerogels, inhibit photocatalytic properties on their own [67].

These structural properties have even more incredible consequences. The most recognizable property for aerogels is their incredible insulation capability. Aerogels are solids, but due to the fact they can consist even up to 99.9% from air [53] both solid and gas conductivity. Due to very small contribution of solid within the structure, this mechanism does not play the primary role, while the gas conductivity is significantly limited because the pore sizes of aerogels usually are below the mean free path value ($0.6 \cdot 10^{-7} - 0.7 \cdot 10^{-7}$ $[m]$). Furthermore, the pore size distribution (to a certain extent) can be controlled with synthesis parameters, which provides excellent control over thermal insulation properties of aerogels. Similarly, aerogels exhibit very good acoustic (and electrical, depending on the type of structure and precursor(s)) insulation properties.

The main disadvantage of aerogels is a consequence of their extraordinary high porosity – the mechanical properties. Aerogels with good mechanical stability can be definitely obtained however usually it leads to compromising their other properties, such as porosity, insulation performance etc.

Nowadays, modern industry requires novel, sustainable materials that can be tailored for very specific applications. In these terms, aerogels are excellent candidates, which explains the interest in this materials and high number of research on optimising their synthesis, structure and properties.

2.4 MODELLING OF AEROGELS FORMATION

Due to the significant interest in the topic of aerogels a need for computational investigation has arisen. Especially that a lot of phenomena cannot be directly measured or observed experimentally, theoretical modelling and simulations for aerogels are in a high demand.

Different type of modelling and computational approach can be distinguished. The first division is regarding the scale of the considered phenomena (Fig. 15). If we look at aerogels structure, we can start to follow the process of gel formation at the atomistic scale to look into mechanisms of reactions of hydrolysis or condensation. We can also use coarse-grained model on molecular or meso-scale level to follow the evolution of particle-based system (for metastable thermodynamic conditions of nucleation and growth). For the thermodynamically unstable spinodal decomposition, a probabilistic method like Lattice Boltzmann method is more

applicable. One can use these approaches also to investigate the properties of a structure (such as mechanical behaviour, thermal conductivity, acoustic insulation etc.) however these studies make the most sense on the macroscale level, as for example, Young modulus for representative volume element of a microstructure will not scale directly to macroscopic sample behaviour. Thus, from potential application point of view, these studies have the most sense on the macro-scale level, using such methods as finite element method (FEM).

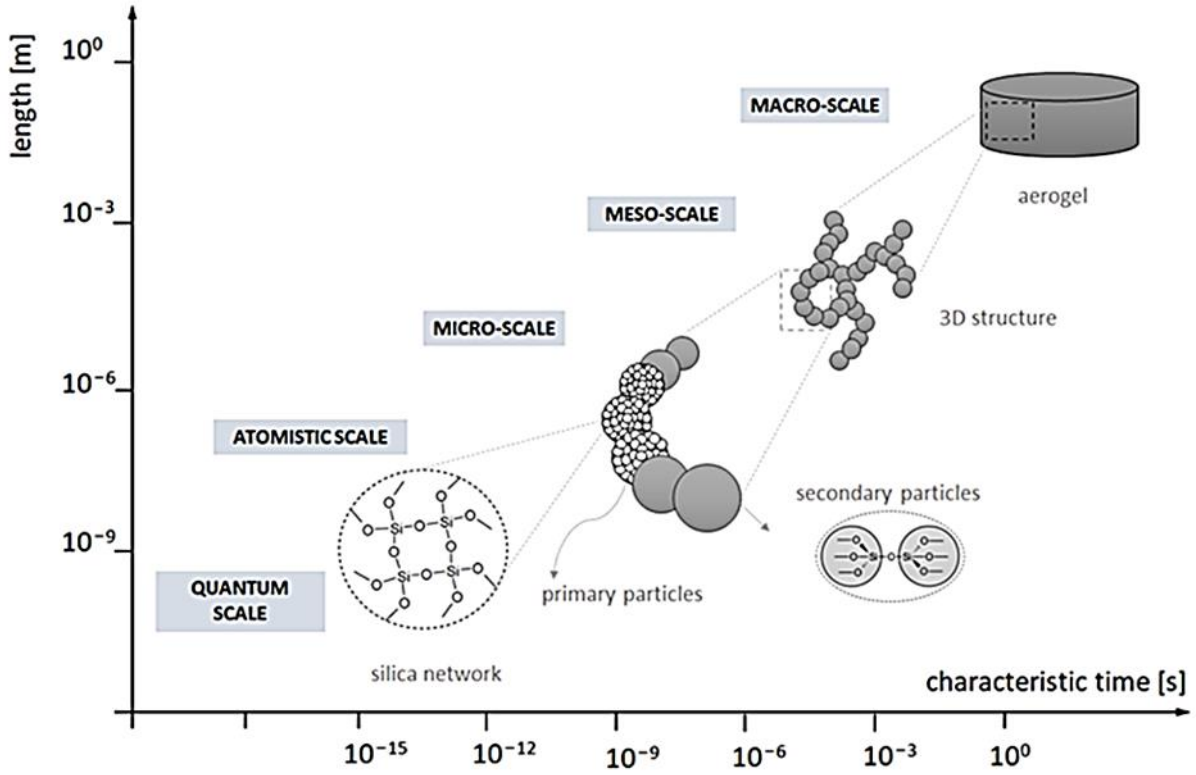

Fig. 15 Multiscale approach for modelling aerogel structure

Focusing on the modelling of structure formation process, the most popular methods are based on:

a) Smoluchowski equation [68–70];
b) discrete element method [71–75];
c) percolation theory [18,76];
d) aggregation models [77–83].

Each of these methods has different limitations – for example, the Smoluchowski equation is limited to capturing gelation kinetics, however it does not provide any insight into morphology evolution of the system with the gelation progress [84].

Discrete element method (DEM) is computationally very expensive, and in order to obtain valid results one has to establish a lot of physico-chemical constants of the system

[75,85]. However the system looks incredibly realistic (as an example, the work of Depta et al. [75]).

Percolation theory and aggregation model are easier in implementation comparing to the DEM method, provide insight into evolution of the microstructure and morphology, however they do not provide directly information about kinetics of the process. However, Hsieh et al. extracted kinetics information from an aggregation model [81]. Nevertheless, any validation of kinetics for this model was not provided in literature yet.

This thesis focus lies on the aggregation model. This approach is usually implemented off-lattice, inside a cubic representative volume element (RVE) with periodic boundary conditions. The essence of this group model is to track the motion (diffusive and other) of particles and then their aggregates, together with their aggregation - until the final structure is created: e.g. a gel. Some of the authors, e.g. Abdusalamov et al. applied specific case of the system with division of particles into “seeds” and “walkers” [83,86].

The different approaches for description of the sol-gel system can be implemented with different computational methods. The choice depends on the chosen scale (atomistic, molecular, micro or meso scale), the required information about the system and computational resources. Among available methods there is Monte Carlo [87], population balance [88], reactive or coarse-grained molecular dynamics [89–91]. Some of the approaches require using an additional software, for example molecular dynamics can be performed with LAMMPS (Large-scale Atomic/Molecular Massively Parallel Simulator) [92] and coarse-grained molecular dynamics with Musen [93].

Within this thesis main focus lies on aggregation model. It was chosen to implement the on-lattice variation with a cellular automaton approach. Cellular automata are used mostly for mechanical behaviour investigations [94,95], but also for processes based on aggregation due to diffusion, such as recrystallisation [96], flocculation [97], as well as for processes with chemical reaction [98].

3. KINETICS AND MECHANISM OF MTMS HYDROLYSIS

3.1 OBJECTIVE

While planning the sol-gel synthesis of silica aerogels, one must consider kinetics and the conversion ratio of hydrolysis. It has a significant impact on number of hydrolysed groups, thus, alcogel structure formation – process that mostly affects the final product properties and range of its potential applications. The goal of the first part of the research was to verify a relatively straightforward hypothesis, which was formulated as follows:

1st hypothesis

> *The hydrolysis of methyltrimethoxysilane in acidic conditions is based on a protonation mechanism, and this step occurs very rapidly, thus, the time of conducting the hydrolysis reaction does not influence further stage of the sol gel synthesis: the gelation process and the gel-point value.*

As it is mentioned in the stated above hypothesis, the mechanism of hydrolysis is already known according to the available literature, and was thoroughly described, for example in the review paper by Issa et al. [14]. Studies presented in this chapter were structured in such a way to verify the protonation as the mechanism of hydrolysis, verify that it is occurring rapidly, and confirm, that the time of the hydrolysis should not influence further research, which

is focused on the kinetics of subsequent structure formation (condensation) process, which is the main focus of this thesis.

The goal was also to develop a nuclear magnetic resonance (NMR) methodology for such investigations. There is literature available on this matter [99–102], however initial trials did not result in good quality data, due to technical problems, such as overlapping signals for hydrogen-1 (proton) and carbon-13 NMR, and too long measurements for silicon-29 to capture the kinetics. Thus, the verification of a relatively straightforward hypothesis became a complex task.

According to my best knowledge the MTMS hydrolysis was followed by hydrogen-1 measurements only by the work of Seddon et al. [103] (in most papers silicon-29 NMR was applied). The first research objective was verification of this paper's methodology. It was of special importance to use this specific technique (hydrogen-1 NMR), as the protonation is assumed to occur rapidly, and any measurements longer than for proton NMR, would not allow to follow reaction kinetics accurately in the studied system (for example, a single carbon-13 NMR measurement lasted more than one minute).

3.2 METHODOLOGY

In the investigated system methyltrimethoxysilane was used as precursor, methanol as solvent and aqueous solution of sulphuric acid as the catalyst of the hydrolysis reaction (scheme of complete hydrolysis is presented in Eq. 3.1). All of the reagents were purchased from Sigma Aldrich. Methanol, water and acid were used in their deuterated form ($CD_3OD,\ D_2O,\ D_2SO_4$), in order to avoid overlapping signals, and strictly follow only changes in precursor structure occurring with the reaction progress.

$$CH_3Si(OCH_3)_3 + 3H_2O \rightarrow CH_3Si(OH)_3 + 3CH_3OH \tag{3.1}$$

Nine samples with variable contribution of acid catalyst solution were chosen to follow kinetics of methyltrimethoxysilane (MTMS) hydrolysis. The precursor and methanol concentrations were constant ($2.12\ mol/dm^3$ and $7.85\ mol/dm^3$ respectively). Molar ratios of the reagents are presented in Table 1.

Following the measurement of the sample's ^{1}H background spectrum, the investigated samples (1-9) were prepared accordingly to contributions presented in the Table 1. Initially, a solution of MTMS in methanol was prepared and vigorously mixed mechanically for five minutes. Subsequently, the acid solution was added and the mixture was stirred for thirty seconds. A fixed volume of reaction mixture (0.5 ml) was inserted into a capillary tube.

The prepared sample was immediately inserted to the benchtop NMR device *Pulsar* $60MHz$. Before measurement, the device was calibrated with the dope water and 12% TMS in chloroform. The samples were measured in reference to a background sample (without catalyst of hydrolysis) with sixteen scans, three seconds delay between scans and 8192 points acquired per scan, with automatic lock and with manual shimming. Subsequently, series of ^{1}H spectra registered during hydrolysis reaction were obtained.

Table 1 Chemical compositions of the samples investigated by NMR

Sample denotation	***Molar composition***			
	MTMS:	*MeOD:*	*D_2O:*	*D_2SO_4*
1	1	3.71	7.14	0.85
2	1	3.71	7.79	0.64
3	1	3.71	8.44	0.42
4	1	3.71	8.76	0.32
5	1	3.71	9.08	0.21
6	1	3.71	9.40	0.11
7	1	3.71	9.54	0.06
8	1	3.71	9.64	0.03
9	1	3.71	9.73	0.00

3.3 SPECTRA ANALYSIS

Exemplary spectrum obtained by NMR spectroscopy is presented in Fig. 16. Two signals are visible – a singlet at frequency of $0.12\ ppm$ and a doublet at $3.4\ ppm$. The first peak ($0.12\ ppm$) is associated with methyl groups ($-CH_3$) within the structure of MTMS and the second peak ($3.4\ ppm$) with methoxy groups ($-O-CH_3$). The lack of other signals indicates the purity of the prepared sample and confirms that the signal from both types of protons within MTMS molecule can be observed (two groups of chemically equivalent protons were marked in Fig. 16).

During kinetics measurements of samples during hydrolysis reaction (after the addition of a given volume of the acidic catalyst) , a decrease of the $0.12\ ppm$ signal was observed. The signal is associated with methyl groups that do not participate in the hydrolysis reaction (Eq. 3.1). Similar observation was found in literature [103], identified as chemical cleavage, although our studies show that this decrease is acid catalyst concentration dependent. It became

a basis of our assumption, that kinetics of MTMS (in its non-hydrolysed form) concentration decrease can be determined based on the 0.12 *ppm* signal decrease.

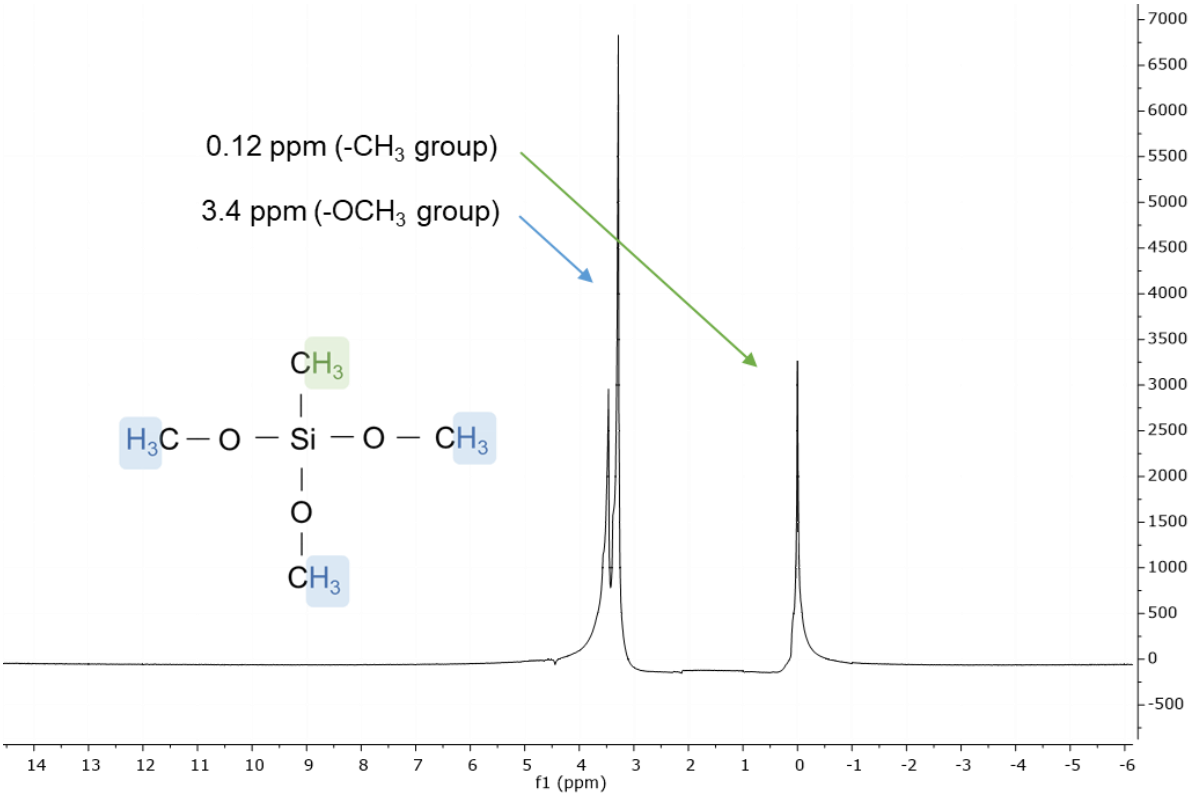

Fig. 16 Exemplary ^{1}H NMR spectrum of MTMS (vol. ratios 1:2:0.9, MTMS:MeOD:D_2SO_4 0.001M); the two groups of chemically equivalent protons within MTMS molecule (inset, marked as blue and green)

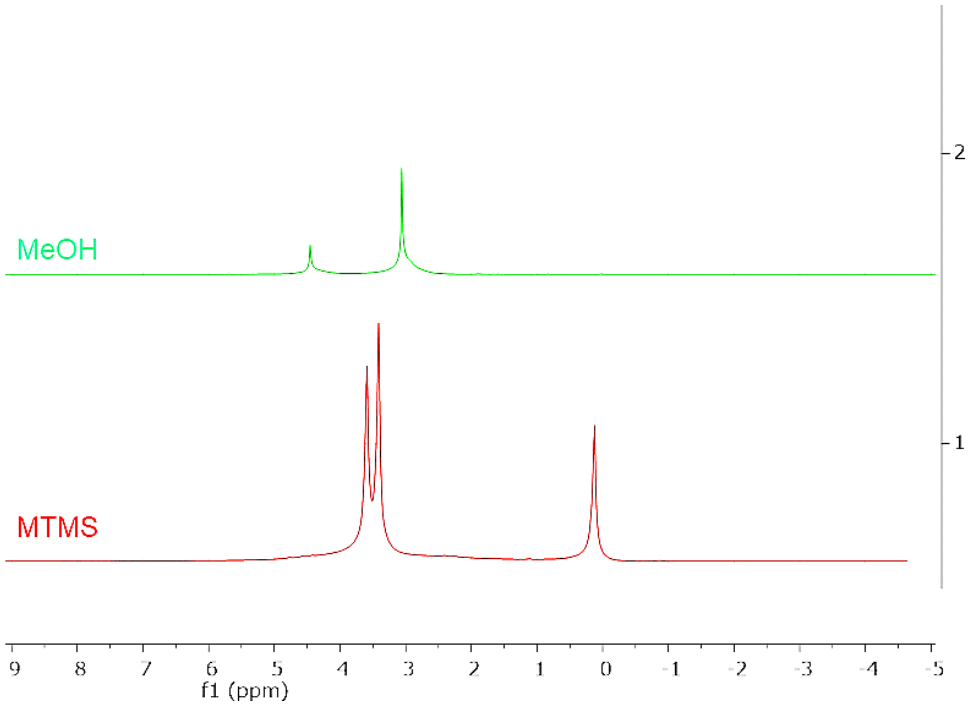

Fig. 17 Comparison of MTMS and methanol ^{1}H spectra

Furthermore, during the kinetics measurements, no other signals was present, even though it was expected to observe a new signal arising due to methanol production during hydrolysis reaction (according to Eq. 3.1), as it was observed by Seddon et al [103]. However, it is possible that the signal of the produced methanol is overlapping with alkoxy groups ($3.4\ ppm$, $-O-CH_3$). The comparison of MTMS and methaol ^{1}H spectra is presented in Fig. 17. The signals arising from methanol in MeOD solution are identified as: 3.3 ppm – methyl ($-CH_3$) groups and $4.5\ ppm$ hydroxyl groups ($-OH$), while alkoxy groups from MTMS molecule appear within the range of $3.4-3.5\ ppm$. Considering a possible change in the chemical environment, it is likely that the production of methanol during the conducted reaction was not visible due to overlapping signals of methanol's $-CH_3$ groups and precursors' $-O-CH_3$ groups.

The dependence of $0.12\ ppm$ signal intensity on time of the reaction, registered for the investigated samples (samples 1-9 included in the Table 1) is presented in Fig. 18. As it was expected, for the sample with no acid , the reaction does not occur, so the intensity for $0.12\ ppm$ remains approximately constant. With an increase of acid concentration, a decrease of the singlet intensity becomes more rapid. This result proves the dependence of the $0.12\ ppm$ signal intensity on the acid concentration. MTMS hydrolysis is, according to common knowledge and extensive research, the only possible reaction in the system.

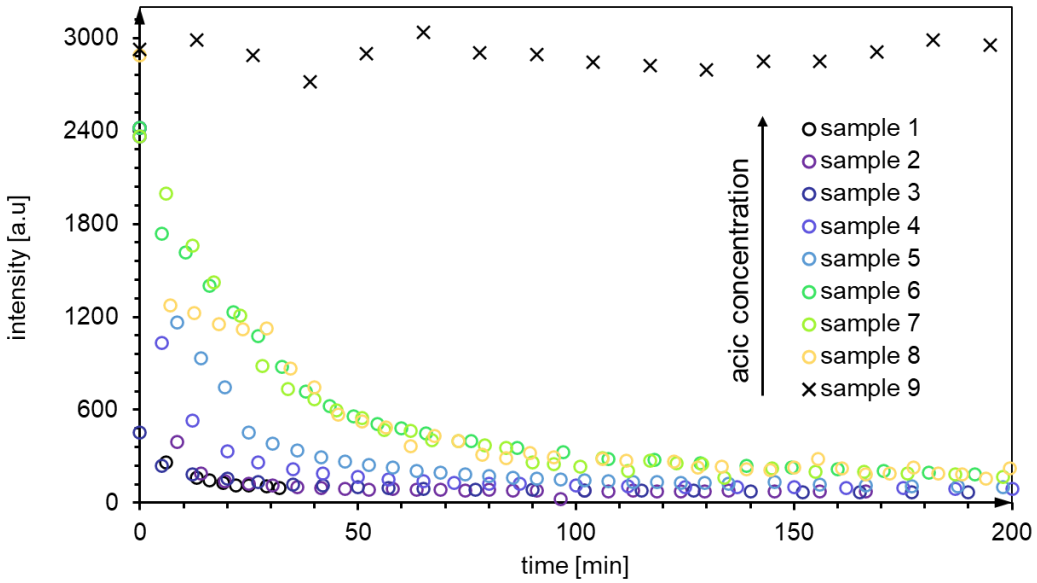

Fig. 18 The dependence of 0.12 ppm signal intensity on the time of hydrolysis reaction and the acid catalyst concentration

3.4 CALCULATION OF THE PROTONATION RATE

The first step of the hydrolysis reaction is protonation (according to Fig. 5 [14]) . Schematically, the course of hydrolysis, including the protonation step, can be written using the following equations:

$$\equiv Si - O - CH_3 + H^+ \rightleftarrows \equiv Si - O(H^+) - CH_3 \tag{3.2}$$

$$\equiv Si - O(H^+) - CH_3 \rightarrow \ hydrolysis\ products \tag{3.3}$$

In the above equations $\equiv Si - O - CH_3$ denotes the organosilicon precursor (MTMS in the considered investigations) and $\equiv Si - O(H^+)$ - protonated form, being a transient product of the reaction. The protonation constant is defined as an equilibrium constant of reaction (3.2), i.e.:

$$K_a = \frac{[\equiv Si - O(H^+) - CH_3]}{[\equiv Si - O - CH_3][H^+]} \tag{3.4}$$

With square brackets denoting the molar concentration. In (3.4) $[H^+]$, the concentration of hydrogen cation, is consistent with acid molar concentration (in this case, it has to be noted the sulfuric acid is a diprotic acid).

At the onset on the hydrolysis reaction the precursor can be in one of two forms - original or protonated (it can be assumed that hydrolysed forms have not yet appeared in the reaction system). Thus:

$$[\equiv Si - O - CH_3] + [\equiv Si - O(H^+) - CH_3] = c_0 \tag{3.5}$$

where c_0 denotes the initial concentration of precursor. Due to combining (3.4) and (3.5) the following form describing equilibrium constant can be obtained:

$$K_a = \frac{[\equiv Si - O(H^+) - CH_3]}{(c_0 - [\equiv Si - O(H^+) - CH_3])[H^+]} \tag{3.6}$$

Thus, the concentration of protonated form of precursor, $[\equiv Si - O(H^+) - CH_3]$, is given as:

$$[\equiv Si - O(H^+) - CH_3] = \frac{[H^+]}{K_a^{-1} + [H^+]} c_0 \tag{3.7}$$

Let's take into the consideration the two stages of the hydrolysis reaction, described by equations 3.2 and 3.3. The first equation (protonation) is a relatively fast reaction and leads to an immediate establishment of the chemical equilibrium described by equation (3.4). The kinetics of the second reaction can be described by the first order kinetic equation:

$$\frac{d[\equiv Si - O(H^+) - CH_3]}{dt} = -k[\equiv Si - O(H^+) - CH_3] \tag{3.8}$$

According to (3.5):

$$d[\equiv Si - O(H^+) - CH_3] = -d[\equiv Si - O - CH_3] \tag{3.9}$$

(while c_0 is constant) and finally the reaction rate formula is obtained:

$$\frac{d[\equiv Si - O - CH_3]}{dt} = k[\equiv Si - O(H^+) - CH_3] = k\frac{[H^+]}{K_a^{-1} + [H^+]}c_0 \tag{3.10}$$

On the other hand, the overall hydrolysis kinetics can be described with the equation stated below (3.11):

$$\frac{d[\equiv Si - O - CH_3]}{dt} = -k_{hydr}[\equiv Si - O - CH_3] \tag{3.11}$$

Where k_{hydr} is the observed (during NMR measurements) rate constant of the hydrolysis reaction. The decay rate of the precursor can be equated with the rate of decay of the $0.12\ ppm$ signal in the NMR spectrum. When taking the decay rate at the very beginning of reaction ($t = 0$) $[Si] = c_0$ and thus, from comparison of Eq. (3.10) and (3.11) a dependence between observed rate constant of the hydrolysis reaction k_{hydr}, the rate of reaction (3.3) k and protonation constant K_a is obtained in the following form:

$$k_{hydr} = -k\frac{[H^+]}{K_a^{-1} + [H^+]} \tag{3.12}$$

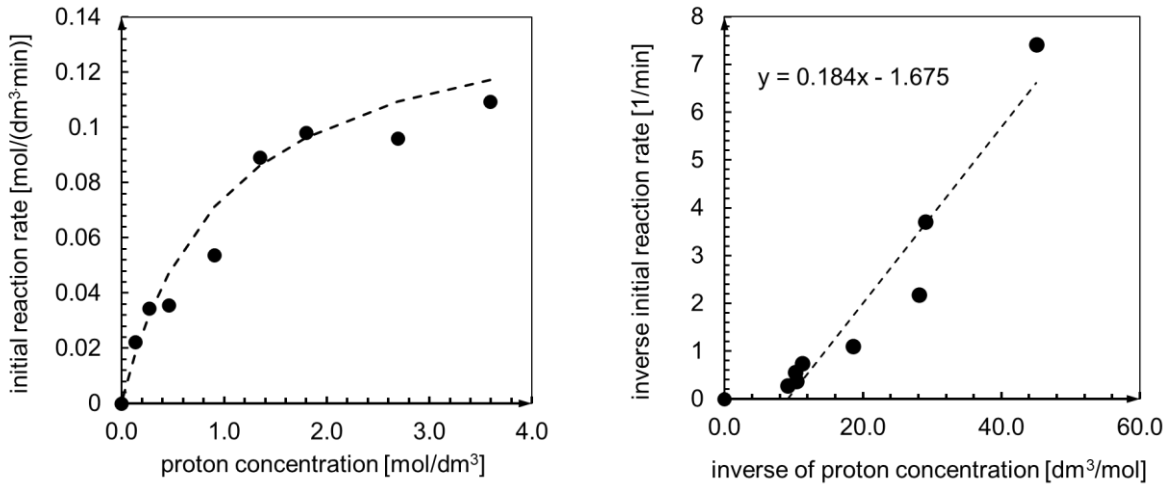

Fig. 19 Dependence of initial reaction rate on H^+ concentration (left) and representation of Eq. 3.13 (right)

This equation may be linearized in regards to the concentration of $[H^+]$ ions:

$$\frac{1}{k_{hydr}} = \frac{1}{kK_a}\frac{1}{[H^+]} - \frac{1}{k} \tag{3.13}$$

The above relation is shown in Fig. 19. Based on this formula, and the linear trendline's slope the protonation constant was determined as 9.1 $[dm^3/mol]$.

3.5 DISCUSSION AND CONCLUSSIONS

The main conclusion is that protonation was confirmed as a mechanism of acidic hydrolysis. Acid dissociation constant was designated as 9.1 $[dm^3/mol]$.

An unexpected conclusion is that the decrease of the signal arising from group was noticed to be dependent on acid concentration. Similar observation was found in the literature Seddon et al., however the authors did not observed the dependence of the signal decrease on acid concentration, and identified the phenomenon as a chemical cleavage [103].

The presented studies did not provide any information about the produced methanol (in contrary to work of Seddon et al.). In this specific system it was probably overlapping with the signal arising from protons included in the $-OCH_3$ groups. The decrease of the $3.4\ ppm$ signal was not observed, presumably due to the fact, that the same amount of methanol molecules is produced during the reaction, as $-OCH_3$ group molecules are consumed, thus the intensity remained approximately constant.

The results indicate a very fast protonation. Subsequently, time of gelation for different time of gelation of an exemplary sample was measured, to confirm the time of gelation in the studied range does not have any impact on the gelation kinetics.

The hydrolysis was conducted for $0.5, 1$ and $1.5\ [h]$. The time of gelation occurring for each of these experiments was not significantly different. Any variation was within standard deviation of the measurements Fig. 20.

Due to the confirmation of the first hypothesis (*"The hydrolysis of methyltrimethoxysilane in acidic conditions is based on a protonation mechanism, and this step occurs very rapidly, thus, the time of conducting the hydrolysis reaction should not influence further stage of the sol gel synthesis: the gelation process and the gel-point value."*) it could be assumed, that the reaction mixtures reaches maximum conversion ratio of hydrolysis reaction, thus, should not impact kinetics of the gelation, which was the main focus of this thesis.

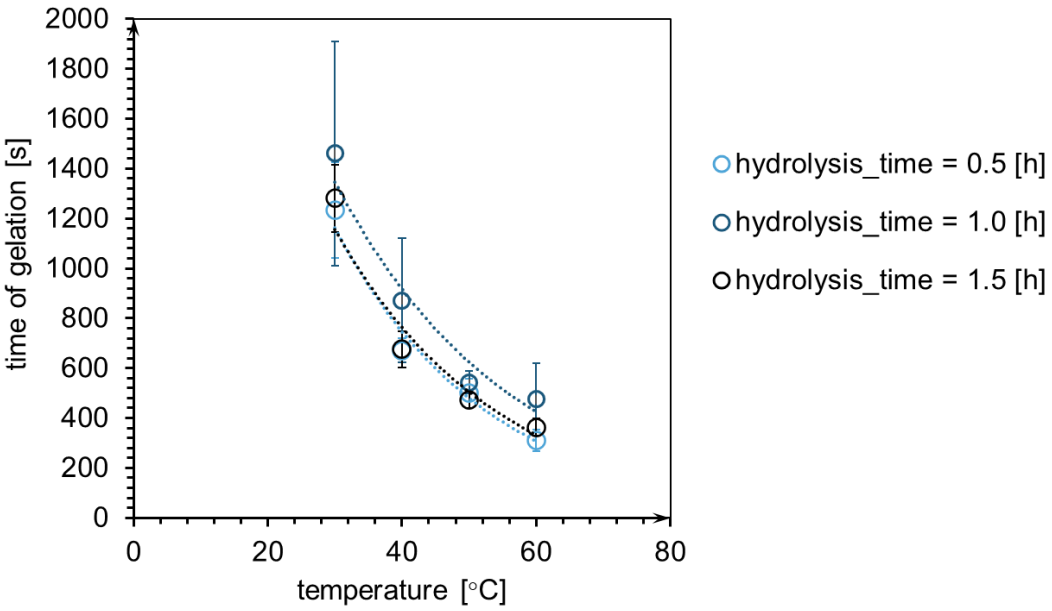

Fig. 20 Dependence of hydrolysis duration and time of gelation

4 ANALYTICAL MODEL OF ORGANOALKOXYSILANE GELATION KINETICS

4.1 OBJECTIVE

The third part of this thesis is focused on developing an analytical model of alcogels condensation kinetics. The model was developed for methyltrimethoxysilane gels formation, however the analytical description could be adapted for other organoalkoxysilanes as well. The goals of this part were as follows:

- developing methodology for experimental registering methyltrimethoxysilane gelation kinetics in basic conditions based on ultraviolet-visible (UV-Vis) spectrophotometry measurements;
- establishing dependence between changes of a sample's absorbance due to gelation progress and mass of condensing product (methyltrimethoxysilane-based alcogel);
- establishing dependence of product's mass on time of reaction and precursor and base catalyst concentration;
- identification of mechanisms of structure formation during an organoalkoxysilane condensation;

The hypothesis for this section was formulated as follows:

2^{nd} hypothesis

The condensation reaction of a chosen organoalkoxysilane (methyltrimethoxysilane) can be followed through UV-Vis spectrophotometric measurements, and the mass of the formed gel

formed due to polycondensation reaction progress is directly proportional to the time-dependant absorbance of a sample. The condensation rate is dependent on the precursor and the base catalyst concentrations. Basing on the condensation kinetics curves, the gelation can be divided into three phases, and the dominant, mechanisms of these phases can be identified.

4.2 METHODOLOGY – EXPERIMENTAL

4.2.1 Synthesis

Methyltrimethoxysilane based alcogel samples were prepared according to synthesis procedure analogical as in Chapter 3. The two step acid-base sol-gel method was applied, according to chemical reactions:

$$\equiv Si - OR \; + \; H_2O \; \rightleftarrows \equiv Si - OH \; + \; R - OH \tag{4.1}$$

$$\equiv Si - OH \; + \; HO - Si \equiv \rightleftarrows \equiv Si - O - Si \equiv \; + H_2O \tag{4.2a}$$

or alternatively:

$$\equiv Si - OR \; + \; HO - Si \equiv \rightleftarrows \equiv Si - O - Si \equiv \; + R - OH \tag{4.2b}$$

In this sol-gel system, methyltrimethoxysilane (MTMS) was used as precursor. As a first step, it was mixed with methanol (the solvent) and with aqueous solution of oxalic acid (as the catalyst of hydrolysis reaction, Eq. 4.1). The acid solution was prepared in distilled water and the concentration was equal to 0.01 $[M]$. The sample was stirred mechanically for one hour at room temperature ($T \; = \; 25$ [℃]). Subsequently, the condensation reaction (Eq. 4.2) was initiated by the addition of base catalyst, which is, aqueous ammonia solution with concentration of 1 $[M]$. Condensation was conducted under constant temperature of either $30, 40, 50, 60,$ or 70 [℃].

Samples were observed during condensation and tilting-test-tube method was used for determination of the gel-point (time of gelation). It is a straightforward, however commonly applied technique [104–114] . It is based on delicate tilting the vessel containing condensing sample, until the mixture starts to behave like a solid, instead of liquid matter. As consequence, a gelled sample can be turned upside down, and the gel structure should not be affected or destroyed. Determination of the gel-point by this method can be quite precise, especially for

MTMS-based alcogels, as in their case, the gel-point is preceded by transition from transparent into turbid solution.

The aging of the condensed samples was performed for $48\ [h]$ at temperature of 50 [℃]. Drying was conducted under ambient pressure conditions (APD), at temperature of 100 [℃] until total evaporation of the liquid filling the pores (mixture of solvent, water and unreacted components).

During the described synthesis, the $MTMS/CH_3OH$ ratio was planned to be constant, while $H_2O/MTMS$ ratio is a variable.

Additionally, the results were compiled with earlier work carried out by the Aerogel Engineering Team of Warsaw University of Technology (AET WUT) on precipitation [115]. Four samples (denoted as A, B, C, D) were prepared with constant $H_2O/MTMS$ molar ratio ($59.75\ [-]$), thus, for extremely low precursor concentration. The variable was the $MTMS/CH_3OH$ ratio. In the case of the cited research, the synthesis procedure was different, as hydrolysis catalyst was injected using syringe pump at a rate of $60\ [ml/h]$, while the reaction mixture was stirred mechanically for $24\ [h]$. Subsequently, the ammonia solution (with concentration of $10\ [M]$) at a rate of $60\ [ml/h]$ was added into the solution to start the gelation. The mentioned synthesis procedure was based on work of Rao et al. [110]. Gelation, ageing and drying were carried out at 50 [℃].

Molar and volume ratios of both synthesis (own work and cited earlier works of AEG WUT) ingredients are included in:

- Table 2 for precipitants (samples denoted as A, B, C, D) obtained for constant $H_2O/MTMS$ molar ratio (earlier works of AET WUT).
- Table 3 for monoliths (samples denoted as E, F, G, H) obtained for constant MTMS/MeOH molar ratio (own results).

Table 2 Molar and volume ratios of synthesis reagents (precipitant samples A-D)

Sample denotation	*$MTMS/CH_3OH$ vol. ratio*	*$H_2O/MTMS$ molar ratio*	*MTMS : MeOH : NH_4OH (10M) : $C_2H_2O_4$ (0.01M) vol. ratio*
A	1:10	59.75	1 : 10 : 4 : 4
B	1:15		1 : 15 : 4 : 4
C	1:20		1 : 20 : 4 : 4
D	1:25		1 : 25 : 4 : 4

Table 3 Molar and volume ratios of synthesis reagents (monolith samples E-H)

Sample denotation	*MTMS/CH_3OH vol. ratio*	*H_2O/MTMS molar ratio*	*MTMS : MeOH : NH_4OH (1M) : $C_2H_2O_4$ (0.01M) vol. ratio*
E	1:2	8.09	1 : 2 : 0.5 : 0.5
F		9.71	1 : 2 : 0.6 : 0.6
G		11.33	1 : 2 : 0.7 : 0.7
H		12.94	1 : 2 : 0.8 : 0.8

4.2.2 Kinetics designation

For registering condensation kinetics data, two methods were used:

- tor the precipitants (samples denoted as A, B, C, D, Table 3) filtration of a gelling solution;
- for monoliths (samples denoted as E, F, G, H, Table 2) absorbance measurements with a UV-Vis spectrophotometer.

During filtration method for precipitants, the gelled product was collected on a cellulose filter material placed on Büchner funnel at pre-set time intervals. The filtrate, after drying at 50 [℃], was weighed. The results of the mass deposition after certain time intervals were plotted as condensation kinetics curves. Spectrophotometric method utilizes *Genesys 10S UV-Vis* spectrophotometer (*Thermo Scientific*) measurements at wavelength $\lambda = 633\ [nm]$. After an addition of the base catalyst (ammonia solution, catalyst of condensation reaction) solution was poured to a disposable polystyrene cuvette and placed in spectrophotometer. Pure methanol was used as a reference sample. The increase of absorbance, occurring as initially transparent sample turns turbid as

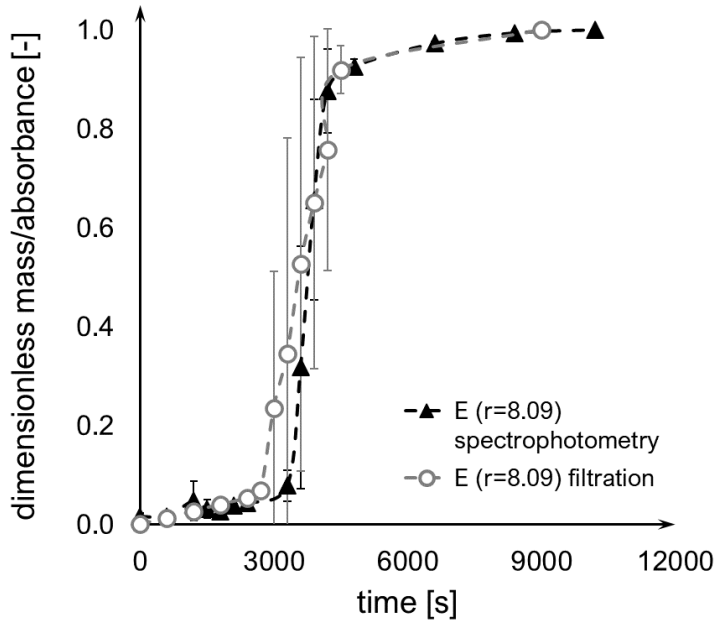

Fig. 21 Comparison of the gelation kinetics obtained by UV–Vis spectrophotometry and filtration method (synthesis *E, r = 8.09*) [115]

the condensation proceeds, was measured in certain time intervals. The results were plotted as kinetics curve.

The equivalence of these two methods was proven by comparing results obtained by filtration/spectrophotometry for the E sample (Fig. 21). It also proves that absorbance is directly proportional to mass of a condensing solution – an important fact that will be used during next chapters of this thesis. Both methods offer a relatively simple and repetitive way to designate gelation kinetics curves.

Based on the gel-point values designated for samples $E-H$ during synthesis, the Arrhenius equation (Eq. 4.3) could be applied to designate the activation energy and A constant (constant in Eq. 4.4, related to Arrhenius constant A_A). It was assumed the gelation time is inversely proportional to the mean or initial) reaction rate $t_g \propto {}^{1}/_{k}$ which led to the linear form of the Arrhenius equation (Eq. 4.4).

$$k = A_A \exp\left(-\frac{E}{RT_g}\right) \tag{4.3}$$

$$\ln t_g = A + \frac{E}{RT_g} \tag{4.4}$$

Where A_A denotes the Arrhenius constant, A - constant dependent on Arrhenius constant, R – universal gas constant, and E - activation energy.

4.3 METHODOLOGY – NUMERICAL

To explain the form of kinetics that was observed during experiments, analytical approach was applied in order to understand the formation and growth of an alcogel structure. To do so, first step is to identify dominant mechanisms of the process. Intuitively four main types of phenomena in the system can be distinguished:

(i) the reaction between two or more precursor particles leading to the appearance of small alcogel cluster;

(ii) the reaction between precursor molecules (or very small clusters) and already formed cluster (surface reaction);

(iii) merging of small clusters into a larger cluster;

(iv) merging of big clusters.

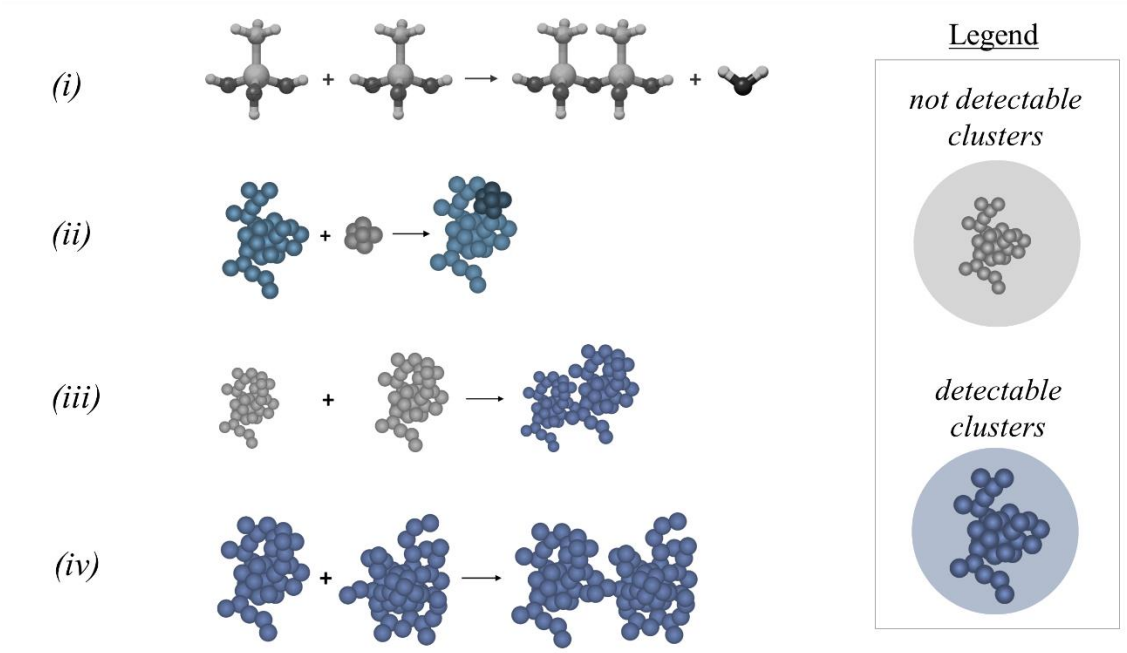

Fig. 22 Distinguished mechanisms of structure formation (grey – undetectable spectroscopically, blue – detectable spectroscopically)

Once the mechanisms are defined, it has to be established which of them affect the increase of the *mass* of the structure, thus the kinetics of the gelation process.

The first mechanism – denoted as (*i*) in Fig. 22 - admittedly is a basis of structure formation, however the size and mass of such a oligomer clusters is too small to be registered spectrophotometrically or captured by a cellulose filter.

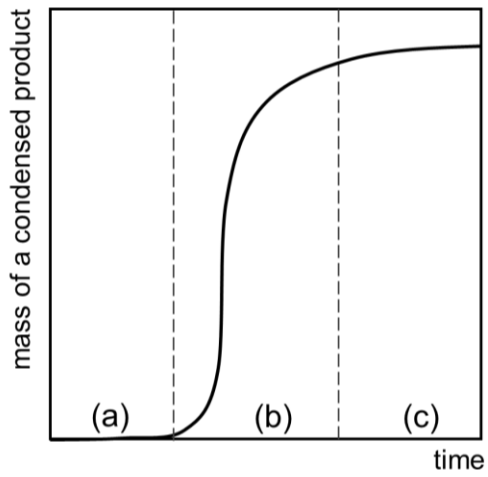

Fig. 23 Assumed phases of a condensation kinetics curve [122]

The second mechanism – denoted as (*ii*) (Fig. 22) - assuming the cluster is already of a detectable size, does indeed affect the condensing product mass, however in a very slow manner (due to very low mass of precursor molecules/oligomers).

The third mechanism (*iii*), assumes the case of two small, undetectable clusters merger into one, big, detectable aggregate. It affects the kinetics (structure formation rate) and leads to the most rapid mass increase of in a condensing system.

The forth (*iv*) mechanism affects strongly morphology of a gelling structure, however it has no impact on the condensing mass assuming the big aggregates were already of detectable size.

Thus, only (*ii*) and (*iii*) mechanisms lead to the increase of condensed product mass – one more slowly, other more rapidly. We can observe on our kinetic such regions (Fig. 23). Mechanisms are presented schematically in Fig. 22, and summary of this consideration is gathered in Table 4.

Table 4 Assumed mechanisms of structure formation during particular condensation phases

Stage of condensation	*Dominant mechanism*
(a) nucleation*	(*i*) and (*ii*)
(b) intensive mass growth (microscopic phase separation)	(*iii*)
(c) cluster-cluster gelation (plateau)	(*iv*)

** Nucleation in this context means a genesis of a new cluster of particles (or a new primary particle of amorphous silica structure), contrary to the nucleation described in Chapter 2, which was a genesis of a new precursor-rich phase.*

Within the scope of this model the focus is on the (ii) mechanism - reaction between precursor molecules and gel clusters. Thus, gel formation rate has to be proportional to precursor concentration (Eq. 4.5).

$$\frac{dm}{dt} = k_0 m^p c \tag{4.5}$$

In the Eq. 4.5, m denotes the mass of alcogel, c – precursor concentration, k is a reaction rate and p is an exponent, in general not equal to 1.

In order to understand the evolution of a condensing system the manner of decrease of precursor concentration has to be considered. Mathematical description of the precursor concentration decrease assumes, that the sum of measured mass of formed alcogel and mass of precursor in the form of molecules present in the reacting solution should be constant.

$$c = c_0 - \frac{m}{V} = \frac{1}{V}(m_0 - m) \tag{4.6}$$

where $m_0 = c_0 V$ and c_0 is equal to an initial precursor concentration. Subsuquently, equation 4.5 can be rewritten as follows:

$$\frac{dm}{dt} = \alpha m^{p}(m_0 - m) \tag{4.7}$$

Where the only unknown parameters are aerogel mass and $\alpha = {}^{k}/_{V}$.

Regarding the exponent p, it must be noted that if $p = 1$, the Eq. 4.7 would become a well-known description of product of first-order kinetics, which is oversimplifying. Based on the assumed dominant mechanism, the condensation reaction proceeds mostly on the surface of particles of alcogel, thus, concentration should be proportional to the surface. Mass is proportional to L^3 and surface to L^2, where L denotes a linear dimension of particles. Subsuquently the exponent value is assumed to be equal to $p = 2/3$. The final form of the equation that describes the rate of mass increase in the considered system takes the form of:

$$\frac{dm}{dt} = \alpha m^{2/3}(m_0 - m) \tag{4.8}$$

The equation 4.8 can be solved analytically as follows:

$$\int_0^m \frac{dm}{\alpha m^{2/3}(m_0 - m)} = \int_0^t dt \tag{4.9}$$

By performing following substitution (eq. 4.10), equation 4.9 is transformed int a sum of two fractions (Eq. 4.12).

$$y = m^{1/3} \tag{4.10}$$

$$\int_0^{m^{1/3}} \frac{dy}{m_0 - y^3} = \alpha t \tag{4.11}$$

$$\int_0^{m^{1/3}} \frac{A}{m_0^{1/3} - y} dy + \int_0^{m^{1/3}} \frac{By + C}{m_0^{2/3} + m_0^{1/3} y + y^2} dy = \alpha t \tag{4.12}$$

Where constants are equal to:

$$A = B = \frac{1}{3m_0^{2/3}} \tag{4.13}$$

$$C = \frac{2}{3m_0^{1/3}} \tag{4.14}$$

The first integral can be solved into:

$$\int_0^{m^{1/3}} \frac{A}{m_0^{1/3} - y} dy = -\frac{1}{3m_0^{2/3}} ln \left| m_0^{1/3} - y \right| \Bigg|_0^{m^{1/3}} \tag{4.15}$$

The second integral is further transformed into a form of:

$$\int_0^{m^{1/3}} \frac{By + C}{m_0^{2/3} + m_0^{1/3} y + y^2} dy = B \int_0^{m^{1/3}} \frac{y + \frac{m_0^{1/3}}{2}}{\left(y + \frac{m_0^{1/3}}{2}\right)^2 + \frac{3}{4} m_0^{2/3}} dy + \frac{3}{2} B m_0^{1/3} \int_0^{m^{1/3}} \frac{1}{\left(y + \frac{m_0^{1/3}}{2}\right)^2 + \frac{3}{4} m_0^{2/3}} dy \tag{4.16}$$

The second integral can be solved as follows:

$$B \int_0^{m^{1/3}} \frac{y + \frac{m_0^{1/3}}{2}}{\left(y + \frac{m_0^{1/3}}{2}\right)^2 + \frac{3}{4} m_0^{2/3}} dy = \frac{1}{2 m_0^{2/3}} \ln \left| m_0^{2/3} + m_0^{1/3} y + y^2 \right| \Big|_0^{m^{1/3}} \tag{4.17}$$

$$\frac{3}{2} B m_0^{1/3} \int_0^{m^{1/3}} \frac{1}{\left(y + \frac{m_0^{1/3}}{2}\right)^2 + \frac{3}{4} m_0^{2/3}} dy = \frac{\sqrt{3}}{m_0^{2/3}} \operatorname{atan} \left| \frac{y + \frac{m_0^{1/3}}{2}}{\frac{\sqrt{3}}{2} m_0^{1/3}} \right| \Bigg|_0^{m^{1/3}} \tag{4.18}$$

Considering eq. 13, 15, 16 leads to the final solution:

$$\frac{1}{2 m_0^{2/3}} \ln \left| \frac{m^{2/3} + m^{1/3} m_0^{1/3} + m_0^{2/3}}{\left(m_0^{1/3} - m^{1/3}\right)^2} \right| + \frac{\sqrt{3}}{m_0^{2/3}} \left(\operatorname{atan} \left| \frac{2 m^{1/3} + m_0^{1/3}}{\sqrt{3} m_0^{1/3}} \right| - \frac{\pi}{6} \right) = \alpha t \tag{4.19}$$

4.4 RESULTS

The morphology of the obtained monolith structures are shown in Fig. 24 . Images were captured with scanning electron microscope (SEM) *HITACHI TM-1000*. One can observe different type of morphologies. Samples E and F are the cocontinuous type of morphology (according to prof. Nakanishi's division [49]) derived due to the spinodal decomposition mechanism, while samples G and H are classic particle aggregates type of structures obtained in nucleation and growth mechanism of microscopic phase separation. Aspect of the connection between initial chemical composition of a sample and occurring type of phase separation, as well as the impact of the PS mechanism on the final morphology of a sample will be discussed in the next chapter.

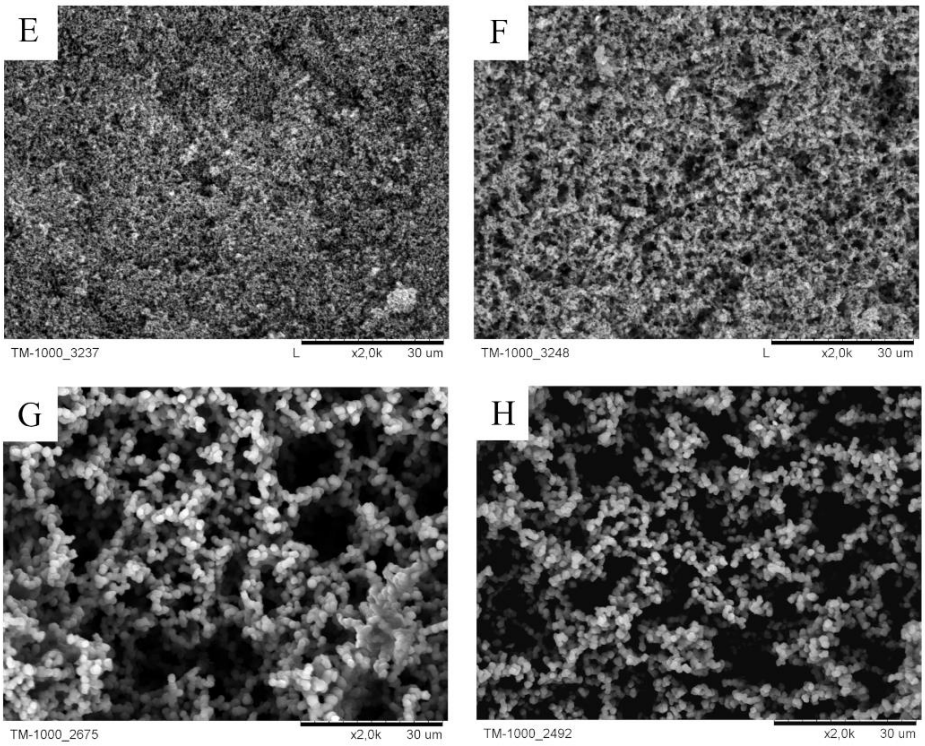

Fig. 24 SEM pictures of syntheses E-H structures, magnification x2000 [115]

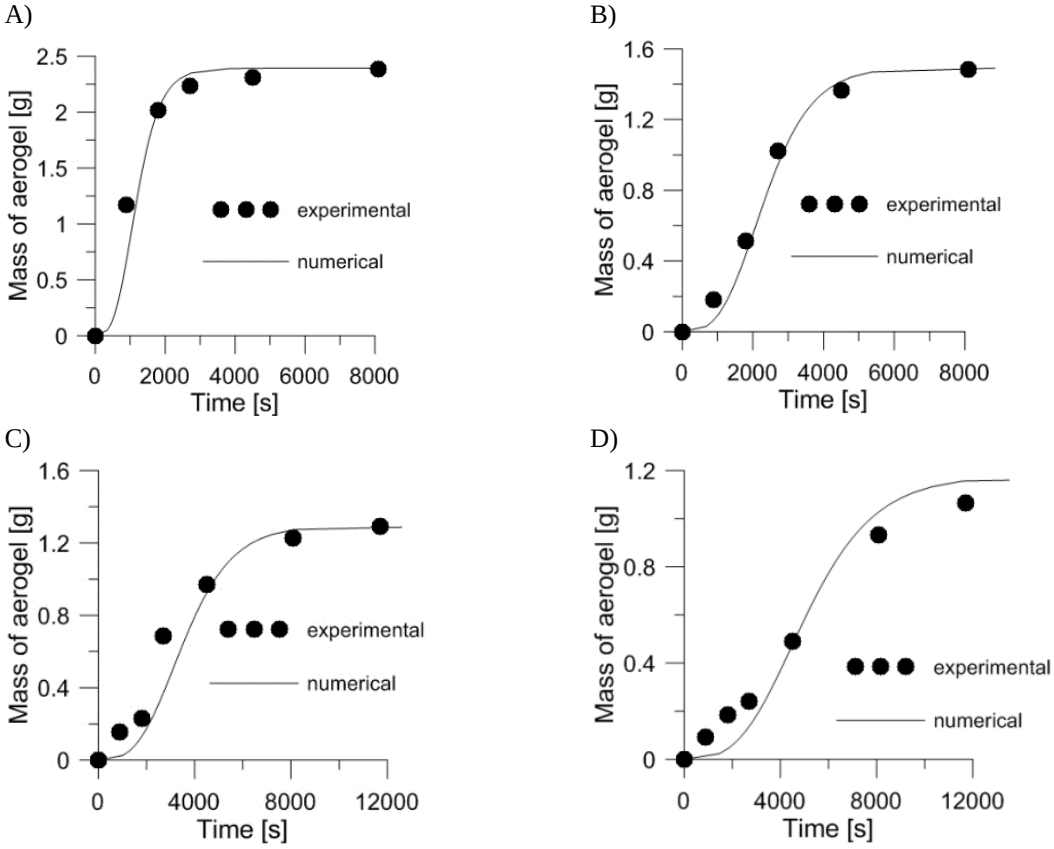

Fig. 25 Dependence of mass of aerogel on time during aerogel formation for four values of precursor to solvent ratio: (A) 1:10 (B) 1:15 (C) 1:20 and (D) 1:25. Comparison of experimental (filtration) and model results [115]

In **Fig. 25**, including the results of kinetics curves for precipitants, it can be observed that the first stage of condensation is not reflected properly, especially for low values of precursor concentrations (samples C, D).

This discrepancy can be caused by different dominant mechanism during initial steps of condensation for very low precursor concentrations. Thus, let's assume the direct reaction between precursor molecules (or their oligomers) as the main mechanism at the beginning of reaction. A following formula of mass growth rate was obtained:

$$\frac{dm}{dt} = k_0 c^2 \tag{4.20}$$

Taking into account equation 4.6:

$$\frac{dm}{dt} = \beta (m_0 - m)^2 \tag{4.21}$$

where β is kinetic constant, proportional to condensation reaction rate. The solution of the Eq. 9 has a well-known form:

$$m(t) = m_0 \frac{\beta m_0 t}{1 + \beta m_0 t} \tag{4.22}$$

This equation describes initial steps of condensation kinetics more accurately. Eq 4.19 is still valid for the later steps. The results of this approach (hybrid molecule-molecule and molecule-cluster) are presented for samples C and D in Fig. 26.

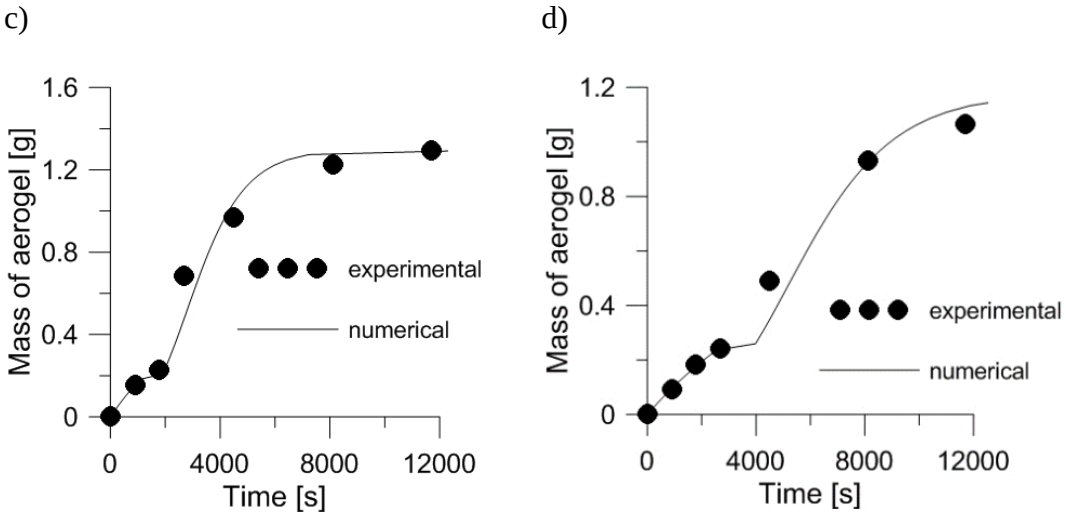

Fig. 26 Comparison of experimental and mathematical results of the dependence of aerogel mass on time of gelation when assuming two stages of gelation process. The precursor to solvent ratio is equal to 1:20 (c) and 1:25 (d) [115]

In **Fig. 27** it can be observed the model works well for condensation kinetics for the monolithic samples $E - H$.

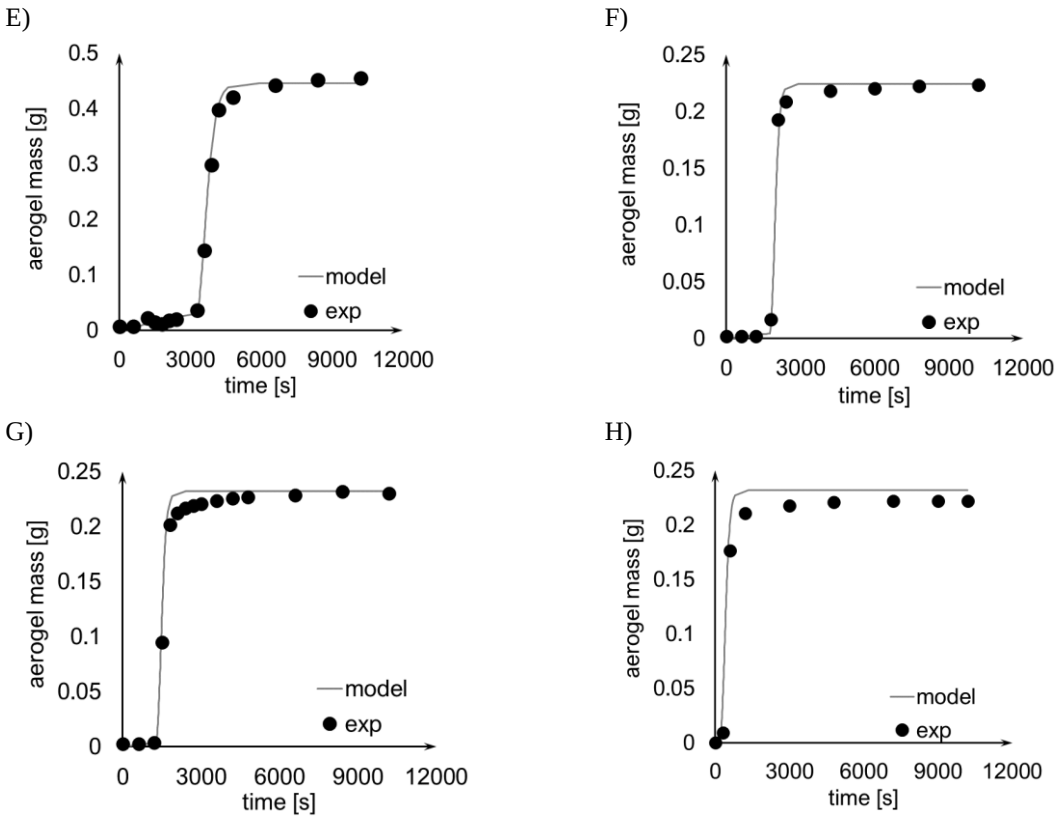

Fig. 27 Dependence of mass of aerogel on time during aerogel formation for four values H_2O/MTMS ratio: *(E) 8.09, (F) 9.71, (G) 11.33 (H) 12.94*. Comparison of experimental (UV-Vis) and model results [115]

During the data analysis it was noted that the kinetics coefficient $k = \alpha\, V$ is not constant for all of the investigated samples. A dependence between value of k and volume of used catalysts. It cannot be precisely stated which – acid or base – as their ratio was the same for all syntheses (according to Table 2 and Table 3). It was assumed that ammonia solution concentration is more significant in the condensation reaction step of the synthesis. By fitting the values to the experimental data, a following dependence was obtained:

$$k = k_0 \cdot c_{NH_4OH}^{3/2} [g^{-2/3} \cdot s^{-1}] \tag{4.23}$$

And with consideration of (Eq. 4.7) the final dependence of condensation rate is obtained:

$$\frac{dm}{dt} = k_0 \cdot c_{NH_4OH}^{3/2} \cdot m^{2/3}(m_0 - m) \tag{4.24}$$

The values of reaction rate constant k_0 for both series of measurements are included in Table 5. Despite slightly different values, the magnitude for both of them is the same, which

provides an initial validation of the proposed theoretical approach, as well as applied experimental methods.

Table 5 The designated reaction rate constant based on two methods of measurements [115]

	based on absorbance measurements	*based on filtrated mass measurements*
reaction rate constant k_0 $\left[\mathrm{mol}^{-3/2} \cdot \mathrm{g}^{-2/3} \cdot \mathrm{s}^{-1}\right]$	$1.16 \cdot 10^{-5}$	$4.30 \cdot 10^{-5}$

4.5 CONCLUSIONS

In this chapter, an applicability of the classic theoretical approach for reaction kinetics was proven, even for a nonstandard systems as condensing alcogels. Furthermore, an applicability of UV-Vis spectrophotometry for kinetics designation for turbid samples was proven valid. The direct dependence between absorbance and mass of condensing product was confirmed by comparison of kinetic data obtained by two methods: spectrophotometrically and by collecting product deposited on a cellulose filter during reaction. However, it should be kept in mind that spectrophotometric measurements are more suitable for monolithic samples, and filtration method for precipitates.

The dependence of an aerogel mass on time (also for very low concentrations of precursor) was obtained (Eq. 4.24). Two leading mechanisms of aerogel condensation kinetics were proposed. The first mechanism was the basic reaction between hydrolysed precursor molecules - either free monomers or mers (within an oligomer or small aggregate). It is the leading mechanism in the initial phase of condensation – the nucleation. The second mechanism is characteristic and dominant in the second phase of condensation. It is based on addition of monomers to a bigger (already detectable) cluster.

The reaction rate constant designated for both experimental series (samples $A - D$ and $E - H$) has slightly different values, but the magnitude of them seems correct. The difference can be a result of relatively high errors for $A - D$ samples (thus, for the results obtained by the filtration method).

The presented results offer the advancement of the state of the art for organoalkoxysilane-based alcogel and aerogel synthesis. Two simple experimental methods of condensation kinetics designation were proposed. The results were compared and proved as equivalent, however filtration method is more suitable for monoliths than monolithic samples, for which,

spectrophotometric method offers precise results. The kinetics of the condensation reaction were studied theoretically, and a simple dependence of mass of the condensing gel on time is proposed and verified experimentally. The possible mechanisms of condensation were proposed, as well as leading mechanisms for specific stages of condensation.

5. GELATION KINETICS AND PHASE SEPARATION DURING ORGANOALKOXYSILANE GEL FORMATION

5.1 OBJECTIVE

The second experimental part of the research was focused on the second step of the organoalkoxysiloxane-based gels synthesis – the condensation step. It was decided to thoroughly study two factors influencing this process:

i. molecular structure of a precursor (to be more precise, the structure and the number of the not hydrolysing alkyl groups -R within the precursor molecule),

ii. chemical composition of the reaction mixture - proportions of the three main ingredients: precursor(s), solvent (alcohol) and antisolvent (water).

As precursors three organoalkoxysilanes were chosen:

1. Methyltrimethoxysilane (MTMS) with the central silicon atom connected to one methyl group ($-CH_3$) and to three methoxy groups ($-O-CH_3$). The three methoxy groups can undergo hydrolysis, and subsequently during the condensation step they can create a covalent bond with oxygen atom, eventually forming three dimensional siloxane network $\left[CH_3SiO_{3/2}\right]_n$ (PMSQ).
2. Vinyltrimethoxysilane (VTMS) with the central silicon atom connected to one vinyl group ($-CH=CH_2$) and to three methoxy groups ($-O-CH_3$). The final network after hydrolysis and condensation of the methoxy groups has the following formula: $\left[CH_2=CHSiO_{3/2}\right]_n$.

3. Dimethyldimethoxysilane (DMDMS) with the central silicon atom connected to two methyl groups ($-CH_3$) and to two methoxy groups ($-O-CH_3$). This precursor does not gel on its own, and it was decided to use it as a co-precursor with MTMS. The formula of the final network after hydrolysis and condensation of the methoxy groups depends on the applied molar ratio of these two co-precursors.

All of the aerogels synthesised based on above-mentioned precursors due to organic groups remaining within the final molecular structure, possess hydrophobic properties and can exhibit impressive flexible behaviour [110,116–119]. However, the focus of this research was on purely fundamental influence of precursor molecule structure on the gel formation process.

The molecular structure of these three chosen organoalkoxysilane precursors is shown in Fig. 28. The not hydrolysing, alkyl groups were highlighted to emphasize the difference in the chemical structure of these compounds.

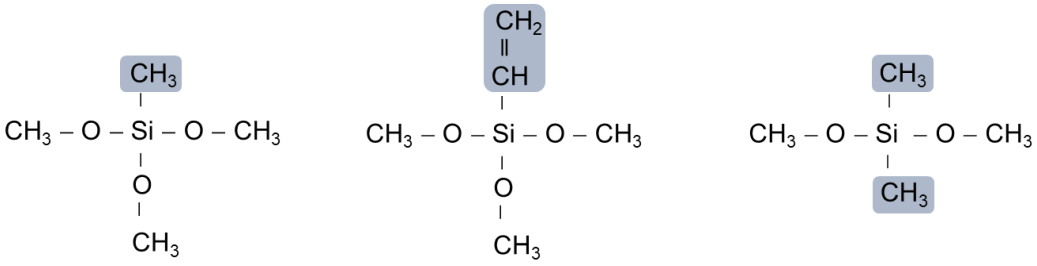

methyltrimethoxysilane (MTMS) | vinylltrimethoxysilane (VTMS) | dimethyldimethoxysilane (DMDMS)

Fig. 28 Representative semi-structural formula of precursors studied within the thesis: methyltrimethoxysilane (MTMS), vinyltrimethoxysilane (VTMS) and (used as a co-precursor with MTMS) dimethyldimethoxysilane (DMDMS)

Different chemical structure leads to different impact of steric effects on condensation kinetics or different morphologies of the final gels. Within this section of the thesis, it was decided to register the condensation kinetics by UV-Vis spectrophotometric measurements. By observations of the final form of the gel, it can be decided whether we observe monolith, precipitant or macroscopic phase separation (not fully gelled structure). In order to deduce the most information about the parallel processes - the condensation and phase separation - it was decided to use ternary plots for the comparison of the studied sol-gel systems. The dried monolithic samples were observed with scanning electron microscope (SEM). Based on the type of their structure, it could be deduced whether the structure was formed due to

the nucleation and growth (the thermodynamically meta-stable mechanism) or the spinodal decomposition (the thermodynamically unstable mechanism). All of these mechanisms were thoroughly discussed in the introduction section (*2.2 Phase separation during sol-gel transition*). This knowledge enables drawing a location of binodal and spinodal curve in the phase diagrams for the studied sol-gel systems. Coupling information about the phase separation mechanism and gelation kinetics provides a comprehensive and extensive knowledge about the formation of organoalkoxysilane-based gels depending on the molecular structure of the precursor and the chemical composition of the synthesis' ingredients.

Thus, it was decided to study the chosen systems with ternary plots with application of UV-Vis spectrophotometer for following condensation kinetics, and SEM for evaluation of final (dried, aerogel) structure. Eventually, the four following cases were studied:

I. The ternary diagram for MTMS with variable catalyst concentration (system denoted as: $TD - M1$). Although the presence of the fourth variable concentration (the catalyst) on the ternary plot may raise doubts, this method of research made it possible to observe the full diversity of structures of the resulting gels, thus, it was decided to include the results in this thesis.

II. The ternary diagram for MTMS with constant catalyst concentration (system denoted as: $TD - M2$). This MTMS-based ternary diagram was used for an actual comparison with the results of the two next cases – diagrams for VTMS and DMDMS-MTMS systems, as the only difference between any point on these three diagrams was the chosen precursor.

III. The ternary diagram for VTMS (system denoted as: $TD - V$) with constant catalyst concentration.

IV. The ternary diagram for DMDMS (as a coprecursor with MTMS in molar ratio DMDMS:MTMS = 1:4) (system denoted as: $TD - D$) with constant catalyst concentration.

The chosen systems and correlation between them are presented schematically in Fig. **29**. The chosen systems can answer the following research questions:

– by the comparison of $TD - M1$ and $TD - M2$: how the wider range of the condensation (base) catalyst concentration influence the variety of the obtained morphologies and the location of binode and spinode in the ternary graphs;

– by the comparison of $TD-M2$, $TD-V$, $TD-D$: how the molecular structure of a precursor and chemical composition of a reaction mixture influences the kinetics of gelation and location of binode and spinode in the ternary graphs.

The hypothesis for this part of this thesis is stated below:

3rd hypothesis

With ternary diagrams based synthesis, one can establish the location of binode and spinode (the range of the metastable and unstable thermodynamic conditions on a ternary plot). Additionally, one can gain a comprehensive and extensive knowledge on impact of (i) molecular structure of precursor, (ii) chemical composition of the reaction mixture on: condensation kinetics, thermodynamic conditions as well as the aerogel morphology.

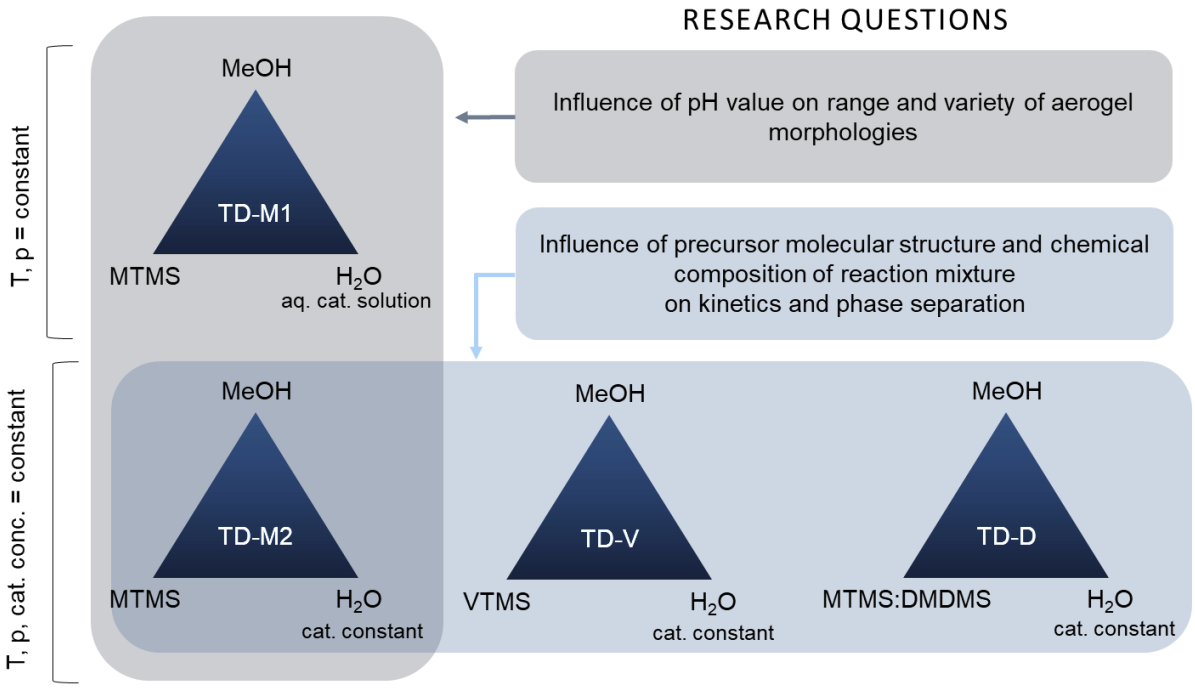

Fig. 29 Schematic representation of studied ternary system and their relation to answering the stated research questions

5.2 METHODOLOGY

5.2.1 The synthesis

For the preparation of ternary plot based samples, the synthesis method was the two step, acid-base sol-gel method, analogical as for previous sections. A given organoalkoxysilane (MTMS, VTMS or co-precursor mixture of MTMS and DMDMS in molar ratio 4:1) was mixed with methanol in an air-tight polypropylene container on an electromagnetic stirrer. After stirring mixture of precursor and alcohol (approximately one minute) the hydrolysis catalyst – the aqueous solution of oxalic acid - was added (according to the values in the tables included in the attachment A1 and attachment A2). The hydrolysis was conducted for one hour in the room temperature ($T \approx 25[℃]$), while a sample was vigorously stirred. After this time, aqueous solution of condensation catalyst - ammonia solution - was added to initiate the condensation. The sample was stirred for approximately thirty seconds, then the stirring element was removed and the sample was set aside for gelation in the room temperature. After complete gelation, the sample aged for one day, and after this time the series of solvent exchange was conducted – first to methanol, then two times to ethanol. After the last solvent exchange samples were left in the oven in the temperature of $50°C$ for one day. Subsuquently, the samples were dried in $100°C$.

Several differences in this overall procedures were made for different systems:

– for system $TD - M1$ (ternary diagram for MTMS with variable catalyst concentration): the concentration of oxalic acid was $0.01\,M$ and for ammonia solution it was $1\,M$. The ternary system was prepared on volume fractions, according to values included in the table in the attachment A1.

– System $TD - M2$, $TD - V$, $TD - D$ (ternary diagram for MTMS, VTMS, and MTMS:DMDMS with constant catalyst concentration) for each synthesis the aqueous solution of catalysts (oxalic acid and ammonia) were prepared individually according to the table in attachment A2), so each sample had constant acid and base concentration, regardless the amount of water in the system. The syntheses were distributed over the whole area of a ternary plot for given, constant ratios of precursor (or co-precursors in case of $TD - D$) to water (presented in Fig. 30). Also, these systems were synthesized in a mass fraction based ternary plot.

– Additionally, the system $TD - D$ (ternary diagram for MTMS:DMDMS with constant catalyst concentration) required addition of surfactant, thus cetrimonium bromide

(CTAB) with amount of 1 $[g]$ per 30 $[ml]$ of reaction mixture was added, leading to concentration CTAB in the initial gelling solution of 0.0915 $[M]$.

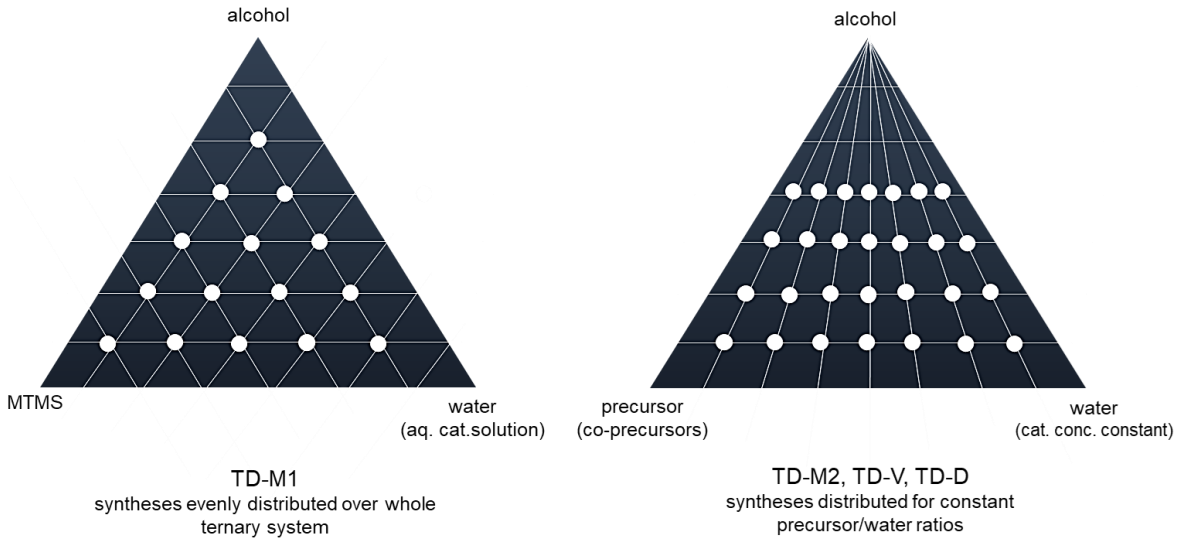

Fig. 30 Schematic representation of studied ternary system and their relation to answering the stated research questions

The recipes for all of the synthesis are included in tables in the attachment A1 (for $TD-M1$ system) and A2 (for $TD-M2$, $TD-V$, and $TD-D$ systems). All of the chemical reactions formulas (condensed and semi-structural) for the hydrolysis and condensation of the chosen precursors (MTMS, VTMS and DMDMS) are shown in Fig. 31.

5.2.2 The gelation kinetics experimental designation

The gelation kinetics was registered with UV-Vis spectrophotometry. The *Genesys 10S* UV-Vis Spectrophotometer (*Thermo Scientific*) was used, and measurements were made for the wavelength $\lambda = 633\ [nm]$.

Samples were prepared according to the methodology and recipes described in the previous subsection (*5.2.1 The synthesis*). After the addition of ammonia solution (the base catalyst of the condensation), a solution was stirred for approximately thirty seconds and the gelling solution in volume of 2.5 $[ml]$ was transferred to a disposable polystyrene cuvette. The cuvette was air-tight closed and secured with a parafilm to avoid any solvent evaporation (especially for sample with slower gelation) due to low evaporation point ($T = 78.4\ [℃]$ [120]) and methanol's toxicity.

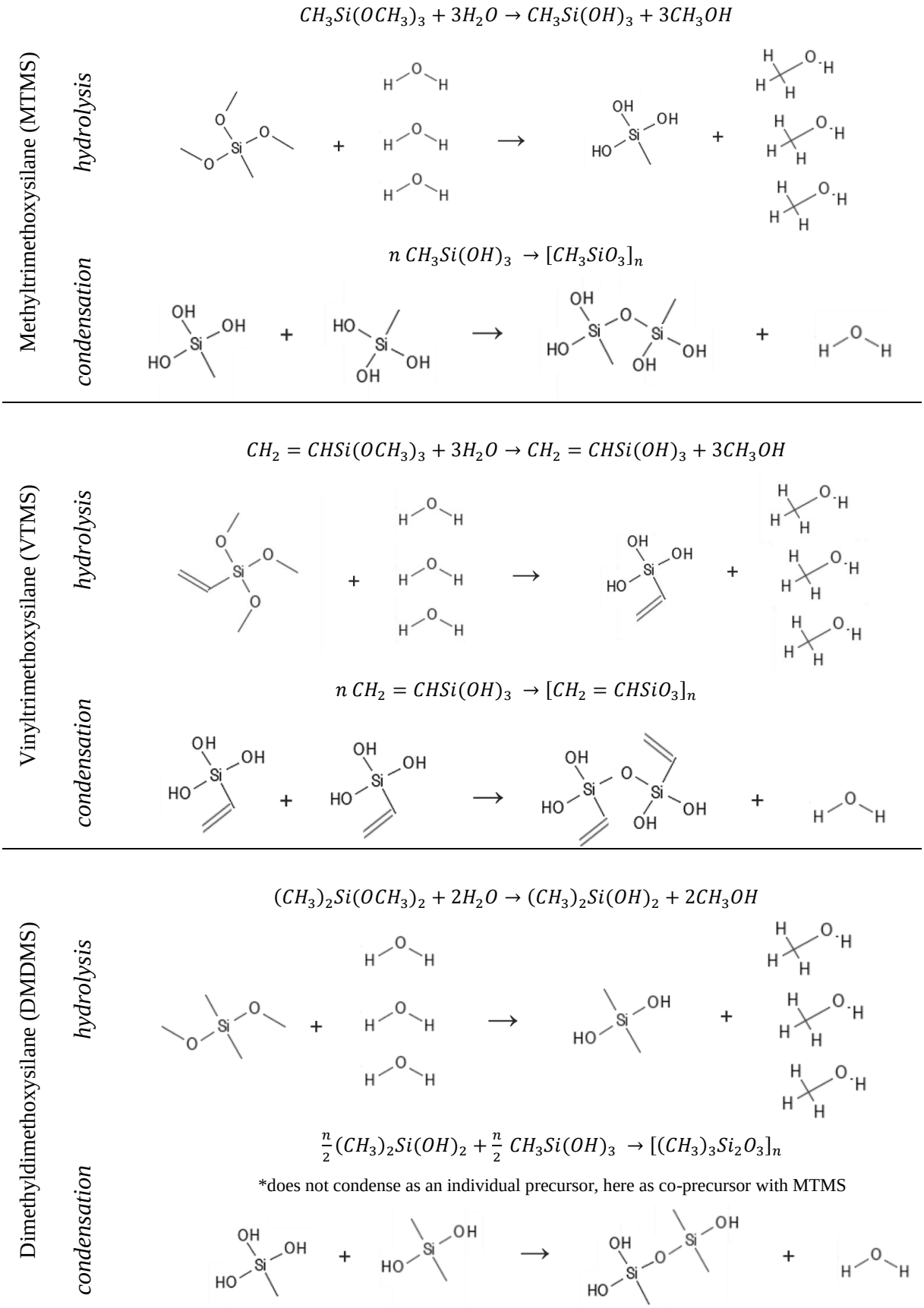

Fig. 31 The hydrolysis and condensation reactions formulas (condensed and semi-structural) for the chosen precursors (MTMS, VTMS and DMDMS)

The sample in a secured cuvette was placed in the spectrophotometer and another cuvette with the pure methanol was set as a reference sample (blank).

For the studied precursors, the turbidity of a sample increases with the progress of gelation – from a transparent colloid to a milky-opaque gelled structure. The absorbance was measured until complete gelation of a sample with certain time intervals, set based on previous observations in such a way, that would allow to collect sufficient number of data points for designation of kinetics curves. A certain part of the samples was omitted due to too fast gelation for collecting a sufficient number of data points (samples with a gel-point below three minutes). The measured values of the absorbance collected over time during gelation process were plotted as kinetics curve.

The overall experimental process – synthesis of samples and parallel UV-Vis spectrophotometric measurements of gelation kinetics are presented schematically in Fig. 32.

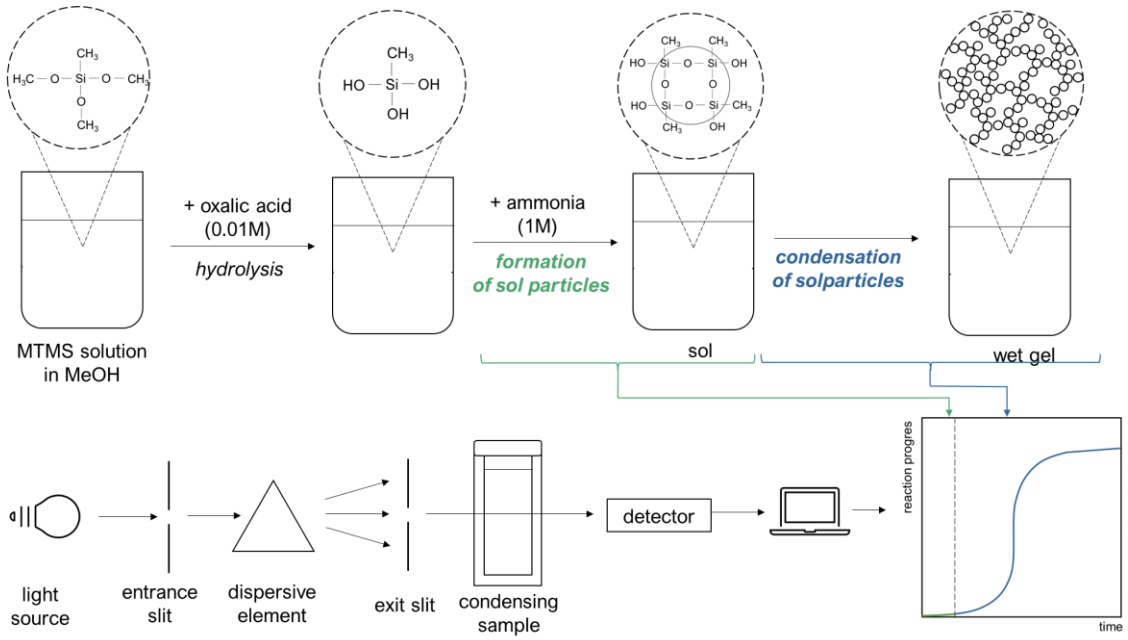

Fig. 32 Overall scheme of the experimental process – the sample synthesis and parallel UV-Vis spectrophotometric measurement of the gelation kinetics

5.2.3 Scanning electron microscopy and image analysis

Final dried samples were observed under scanning electron microscope (SEM), *HITACHI TM-1000*. The aerogel samples are an electric insulator, thus a carbon tape was used to attach the samples to the specimen holder. Samples were cut with a scalpel blade to obtain thin, flat slices with a clean cut surface. A prepared specimen was sputtered with a gold

nanolayer with vacuum sputter coater *Emitech K550X*, with pressure inside the chamber of 10^{-1} $[mbar]$.

The pictures were analysed in terms of morphology, analogically to the morphology classification proposed by professor Nakanishi et. al [49]. The four main types of micro-structure are presented in Fig. 34.

For $TD-M1$, $TD-M2$ and $TD-V$ systems the *ImageJ* software was applied for the analysis of secondary particles size distribution. The particles were assumed to be sphere-shaped (which was confirmed by SEM images evaluation) and diameter of each particle was measured three times and averaged. For each histogram, fifty particles were measured (providing 150 diameter measurements per picture in total). Basing on size distributions, the dispersity Đ (polydispersity index) was calculated as $Đ = \left(\sigma/\bar{d}\right)^2$, where $\bar{d}$ is the number weighted mean diameter of secondary particles for a given aerogel sample and σ is the standard deviation. Samples with $Đ > 0.1$ are classified as polydisperse.

5.3 RESULTS

5.3.1 Phase separation in TD-M1 system

The samples prepared for the $TD-M1$ system (according to the initial reaction mixture compositions included in the table in the attachment A1) were plotted in Fig. 35 with consideration of the obtained type of morphology. Basing on the SEM analysis, structures were classified according to work of Nakanishi et al. [49]. The classification provided further information about microscopic phase separation mechanism (nucleation and growth or spinodal decomposition), thus allowed to approximately sketch the binode's location and the part of the spinodal curve in the phase diagram. The areas of the two types of microscopic phase separation - nucleation and growth or spinodal decomposition – were marked with two shades of grey areas (as presented in Fig. 35).

The binodal curve is based on the MTMS-H_2O side of the ternary diagram. Within the area of the binode, the transition from nucleation & growth mechanism to spinodal decomposition can be observed while increasing the MTMS/H_2O molar ratio. There is a border between these two regions, corresponding to the spinodal curve location, although it was not completely designated.

For the lowest concentrations of the precursor (~10%$_{mas}$) condensation does not occur within the whole sample volume for the whole range of MeOH/H_2O ratio. Too low precursor

contribution in the ternary system leads to the macroscopic phase separation, thus the synthesis results in precipitants or collapsed, not completely interlinked structures. In the low water concentrations region (~5%$_{mas}$), no signs of the condensation reaction were observed, probably due to insufficient hydrolysis conversion ratio. Regarding the solvent content and the condensation range, the monolithic samples were obtained even for just 4.2%$_{mas}$ of methanol.

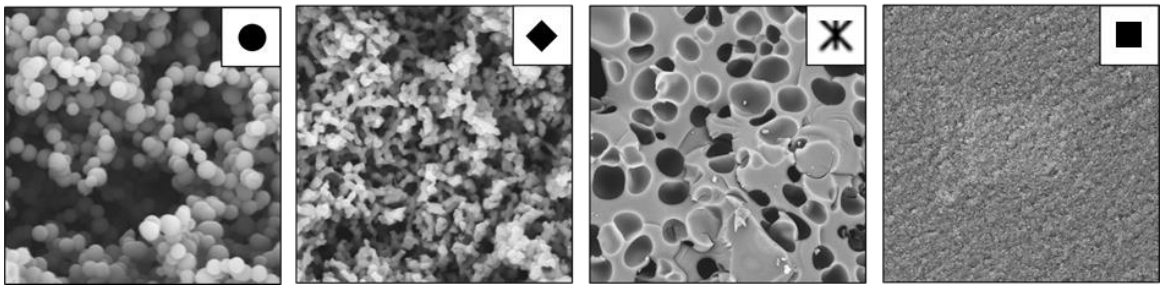

Fig. 34 Four types of an aerogel micro-structure (magnification: 2000x), from the left: particle aggregates, co-continuous, isolated pores, nanoporous structure

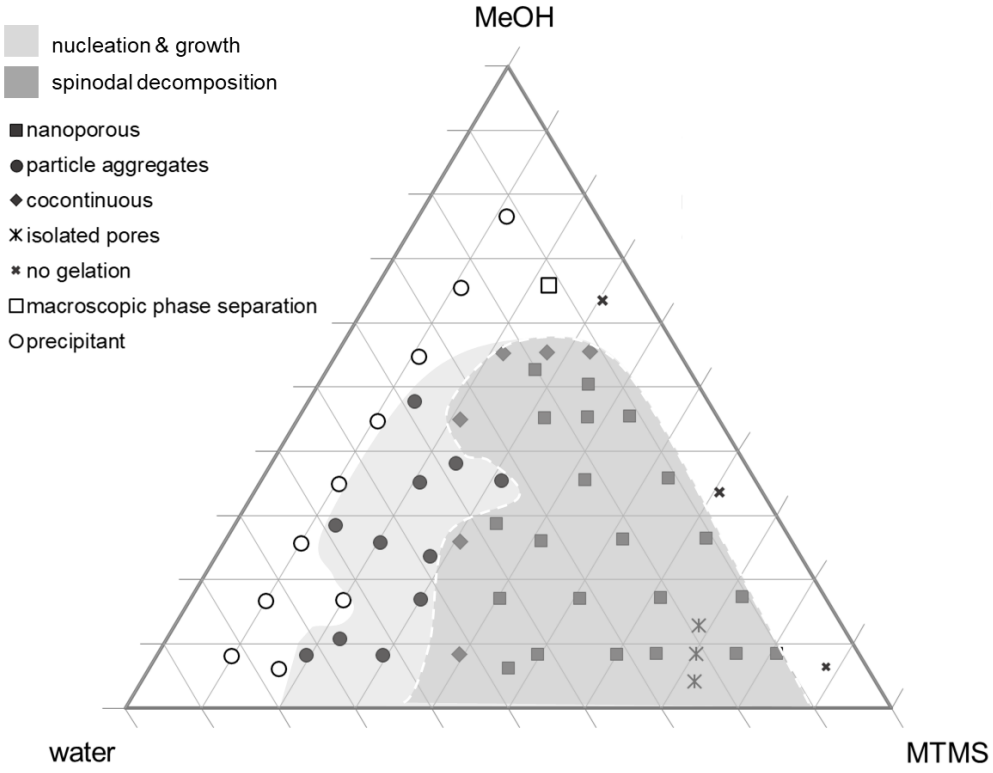

Fig. 35 Ternary diagram for the TD-M1 system

The influence of the initial chemical composition of the reaction mixture on the morphology of the final dried gels is presented in Fig. 36. The schematic comparison highlights the influence of precursor concentration on product morphology for constant solvent

concentration - transition of the system from nucleation and growth microscopic phase separation mechanism into the spinodal decomposition. The analogical tendency is observed for constant precursor concentration when MeOH/H_2O ratio is increasing.

In the ternary diagram (Fig. 35) and morphology comparison (Fig. 36), spinodal decomposition mechanism occurs for approximately precursor concentration above 35%$_{mas}$. Below this value of MTMS concentration (approximately) only nucleation and growth mechanism can be observed.

As far as water contribution is concerned, the nucleation and growth mechanism occurs for higher amounts of water in the system. The samples with water content 60%$_{mas}$ and higher, lead only to particle aggregates type of structure, moreover, for drastically high water concentrations synthesis resulted in precipitates.

While analysing the influence of methanol amount in the system it was observed that for constant concentration of solvent, N&G occurs for approximately, MTMS/H_2O > 1.9 (mass ratio).

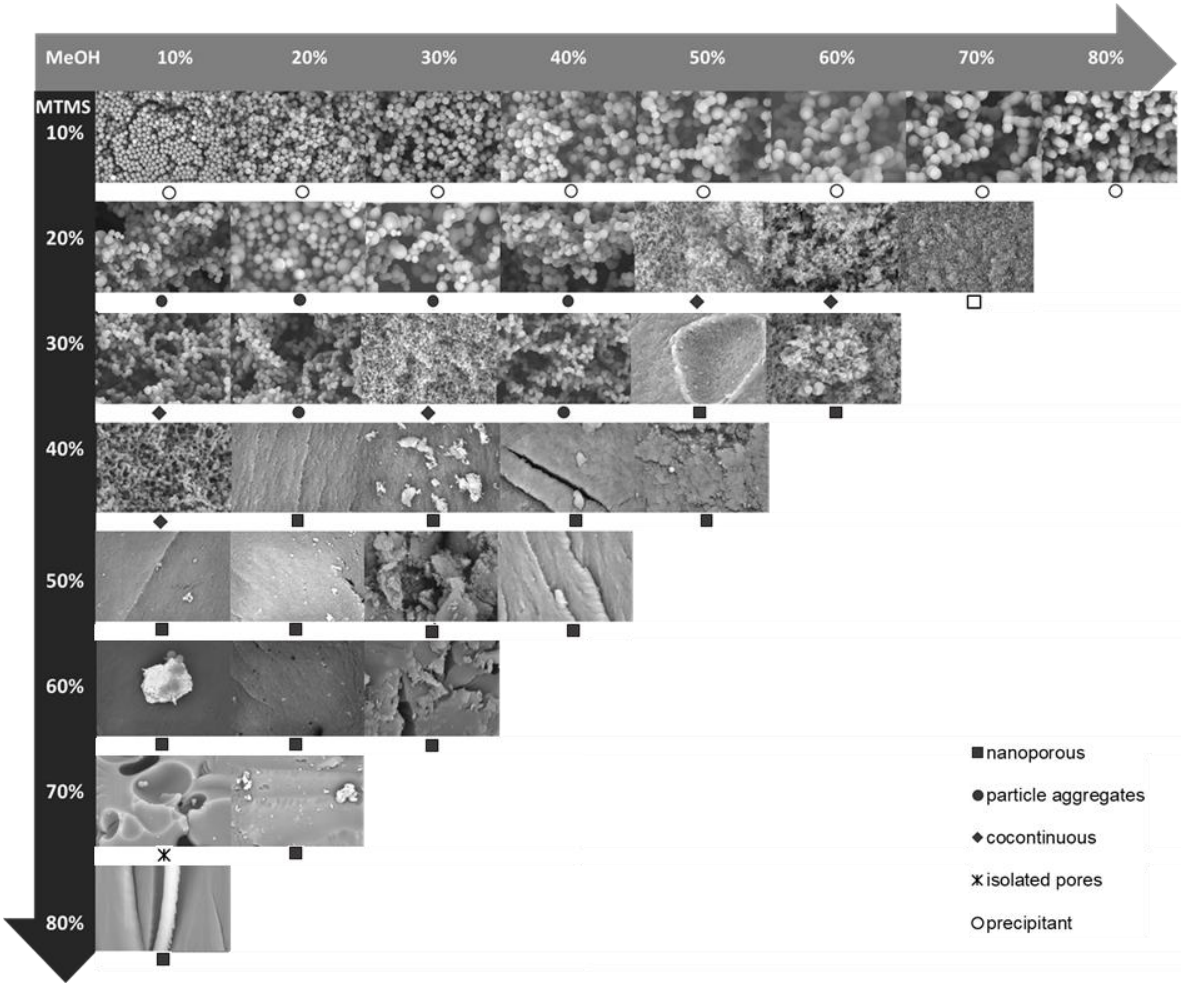

Fig. 36 The influence of the initial chemical composition of the reaction mixture on the morphology of the final dried gels

The values of the dried samples' porosity ε (described by the Equation 5.1, with structural density $\rho_s = 1.2\ [g/cm^3]$, and ρ_{env} denoting envelope density of a sample) are plotted as in the Attachment A3. The evident tendency is the decrease of structure's porosity with the increase of MTMS/H_2O ratio, when the constant concentration of MeOH is considered. The observation leads to further conclusions: the porosity decreases with increase of precursor concentration in the system, or as the microscopic phase separation mechanism changes from nucleation and growth to the spinodal decomposition. Thus, particle aggregates are mostly endowed with higher porosity than other types of structure. Although, two cocontinuous samples, with composition 30.74-25.96-43.31%$_{mas}$ (MTMS-MeOH-H_2O %$_{mas}$) and 39.49-8.34-52.17%$_{mas}$, also exhibit relatively high porosities (82% and 90%, respectively).

The diagram with included volume shrinkage (V_s) values defined according to Eq. 5.2 as a ratio of dried sample (V_{ae}) volume to alcogel volume (V_{al}) (Attachment A3) has, naturally, a reversed form. These two parameters are connected with each other: the higher volume shrinkage occurs, the lower aerogel porosity is obtained. However, the drying method has to be considered when analysing the results. Thus, application of supercritical drying (SPD) instead of the ambient pressure drying technique, could provide significantly different results.

$$\varepsilon = 1 - \frac{\rho_{env}}{\rho_s} \tag{5.1}$$

$$V_s = \frac{V_{ae}}{V_{al}} \tag{5.2}$$

The values of the mean diameter of secondary particles and polydispersity index Đ are plotted as in the Attachment A4 (applies only for the particle aggregates type of samples). The parameter was calculated for both monoliths and precipitants, as long as the structure exhibits the particle aggregate type of morphology. The investigated region appears near the left side of the binodal curve (for samples with MTMS concentration approximately 10, 20 and 30%$_{mas}$). The polydispersity index was designated according to the formula $Đ = \left(\sigma/\bar{d}\right)^2$ (where $\bar{d}$ is the number weighted mean diameter of secondary particles for a given aerogel sample and σ is the standard deviation). Samples with $Đ > 0.1$ were classified as polydisperse.

. The only samples that exhibits polydispersity of secondary particles' size ($Đ > 0.1$) are the samples for the concentration of MTMS approximately 20%$_{mas}$.

These preliminary observations can find the confirmation in secondary particles' size distributions – a comparison is presented in Fig. 38. The magnification of histogram for one the most monodisperse sample (11.3-76.7-12.0%$_{mas}$, $Đ = 0.01$) and the most polydisperse

sample (19.5-8.2-72.2%$_{mas}$, $Đ = 0.20$) are included in Fig. 37 and the difference between them is self-explanatory – we observe narrow peak for the monodisperse sample and a very wide peak (can include multiple maxima) for the polydisperse sample.

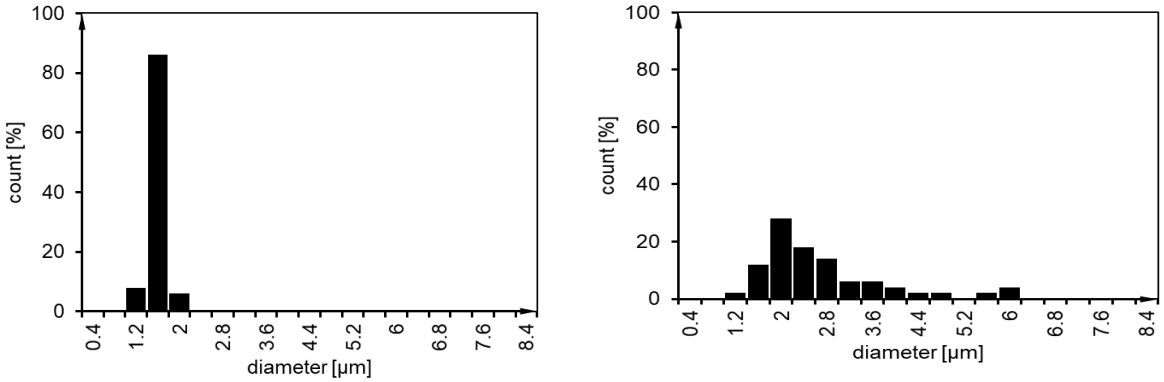

Fig. 37 The comparison of histograms for the most monodisperse sample (11.3-76.7-12.0%$_{mas}$, Đ=0.01) (left) and the most polydisperse sample (19.5-8.2-72.2%$_{mas}$, Đ=0.20) (right)

The comparison of the histograms (Fig. 38) and morphologies (Fig. 39) highlights the impact of the precursor and solvent concentration (consequently, also the water content as the third component in the ternary system, or the overall initial chemical composition of a given sample) on the particle aggregates morphology – we observe different width of the bottle-necks between particles, or regularity of the spherical shape. For MTMS 10%$_{vol}$ the index remains very low value 0.01-0.05 within the whole range of $MeOH/H_2O$ ratio. For samples with 20%$_{vol}$ of MTMS within the initial composition, the increase of $MeOH/H_2O$ ratio leads to less polydisperse aggregates (lower polydispersity index). For 30%$_{vol}$ of MTMS only three samples with "particle aggregates" structure was obtained, thus there is no enough data to evaluate any tendency. A remark: on the schemes presented in the Fig. 36, Fig. 38 and Fig. 39 volume concentrations were plotted, as this part of the experimental research was originally planned with volume concentrations. The rest of graphs, and all the ternary plots (presented in the Fig. **35** and attachments A3-A6) were plotted for mass concentrations to maintain the consistency with the phase diagrams included in the next sections of this chapter (as it was decided to continue research using mass concentrations).The exemplary pictures of particle aggregates structures are compared in Fig. 39. When comparing the pictures for MTMS 10%$_{vol}$, the transition from precipitant (10-10-80, 10-20-70, 10-30-60%$_{vol}$) to macroscopic phase separation structures (10-40-50, 10-50-40, 10-60-30, 10-70-20, 10-80-10%$_{vol}$) can be observed. The changes in the length of bottle-necks are also visible with the precipitant-macroscopic PS transition, it even seems that the length of the bottle-necks is increasing with methanol concentration.

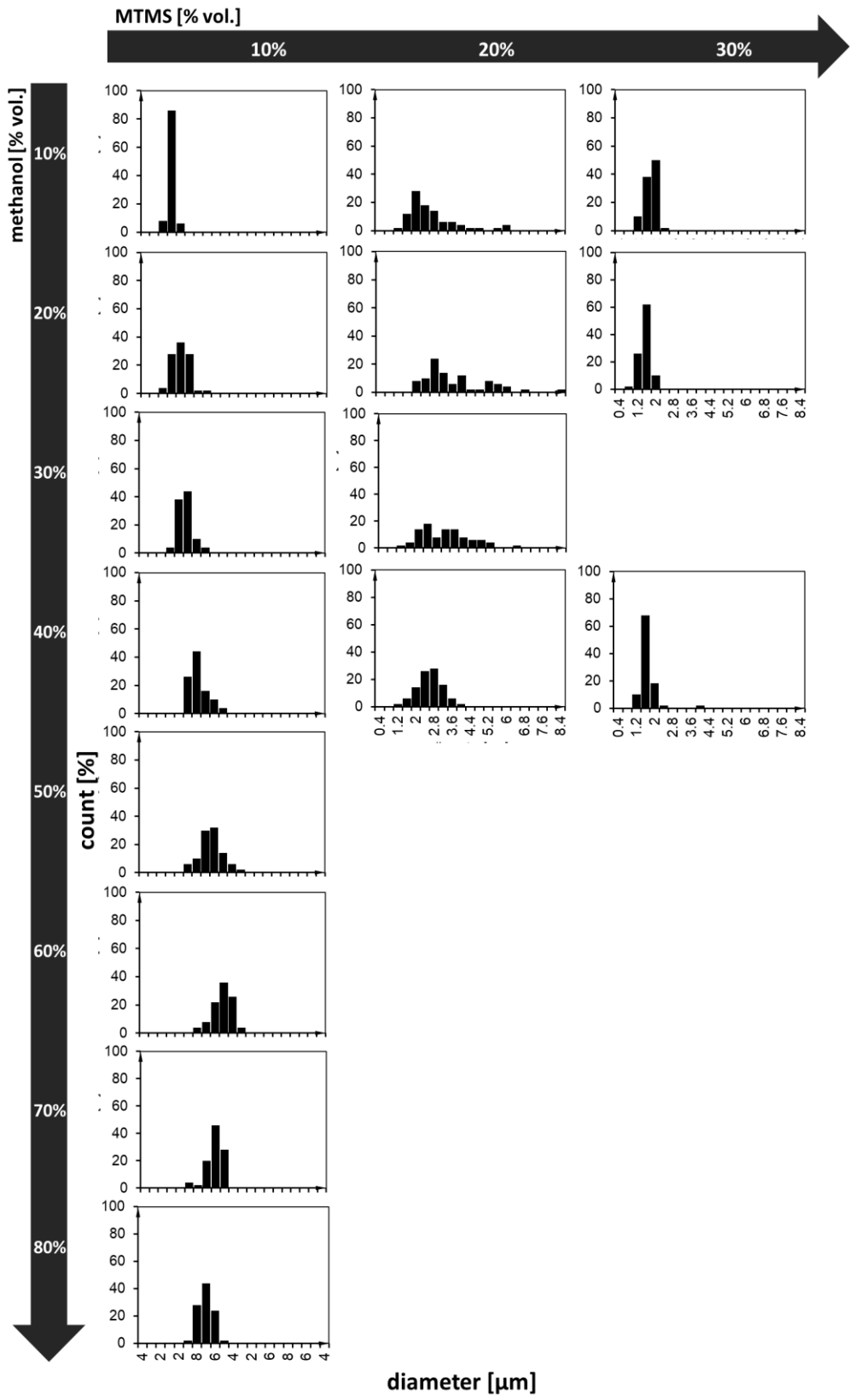

Fig. 38 The comparison of secondary particles size distributions due to initial chemical composition of a sample

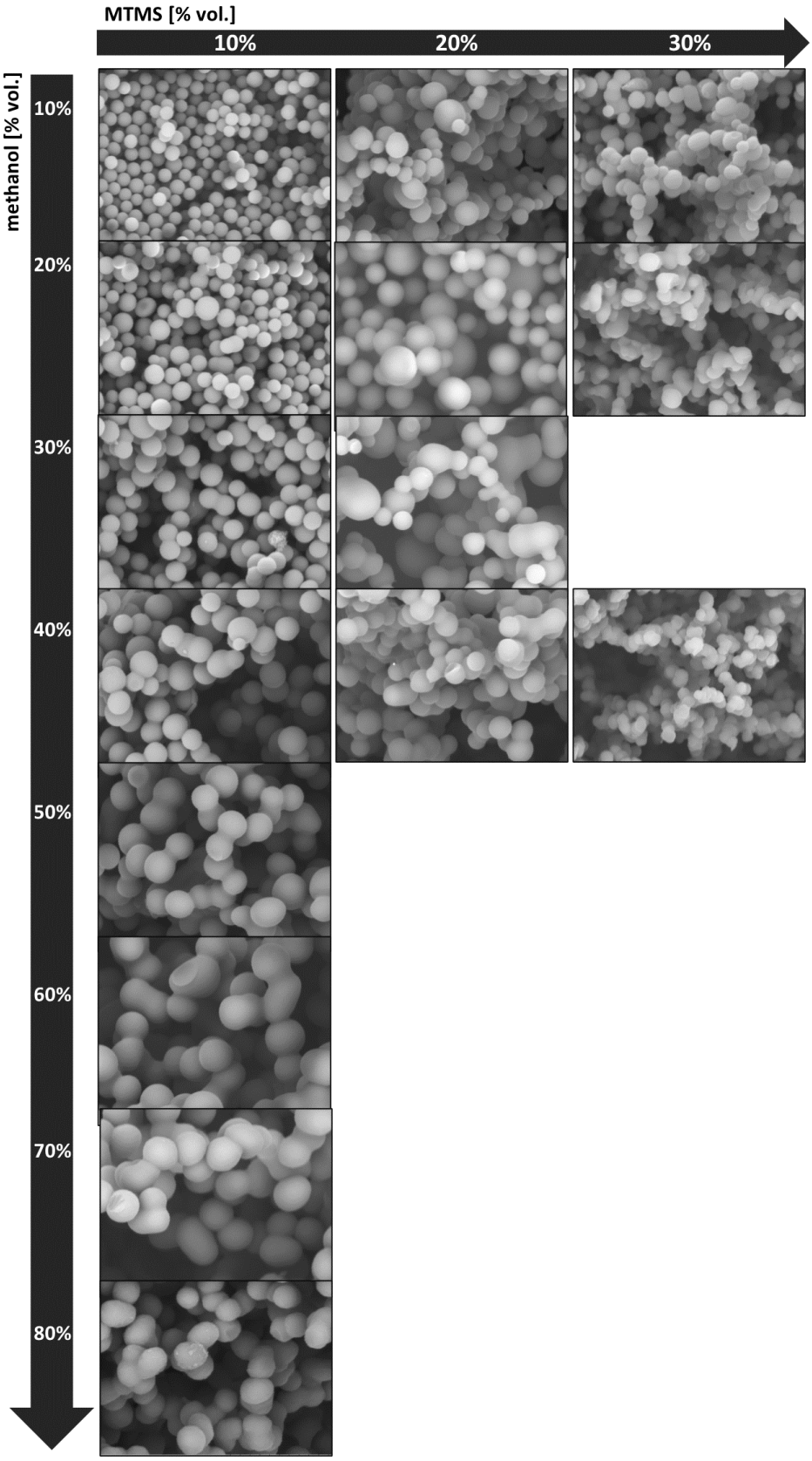

Fig. 39 The comparison of "particle aggregates" morphology due to initial chemical composition of a sample in terms of polydispersity (magnification 5000x)

When comparing samples with 10%$_{vol}$ of MTMS to samples with 20%$_{vol}$ of MTMS (especially 20-10-70, 20-20-60, 20-30-50%$_{vol}$) the changes in polydispersity are prominent, despite moderate changes in polydispersity index (Đ average for 10%$_{vol}$ MTMS is 0.02, and for 20%$_{vol}$ MTMS it is equal to 0.14). Whereas, samples with 30%$_{vol}$ of MTMS seem like a transition from between "particle aggregates" and "co-continuous" structures with moderate values of polydispersity index (average Đ equal to 0.05).

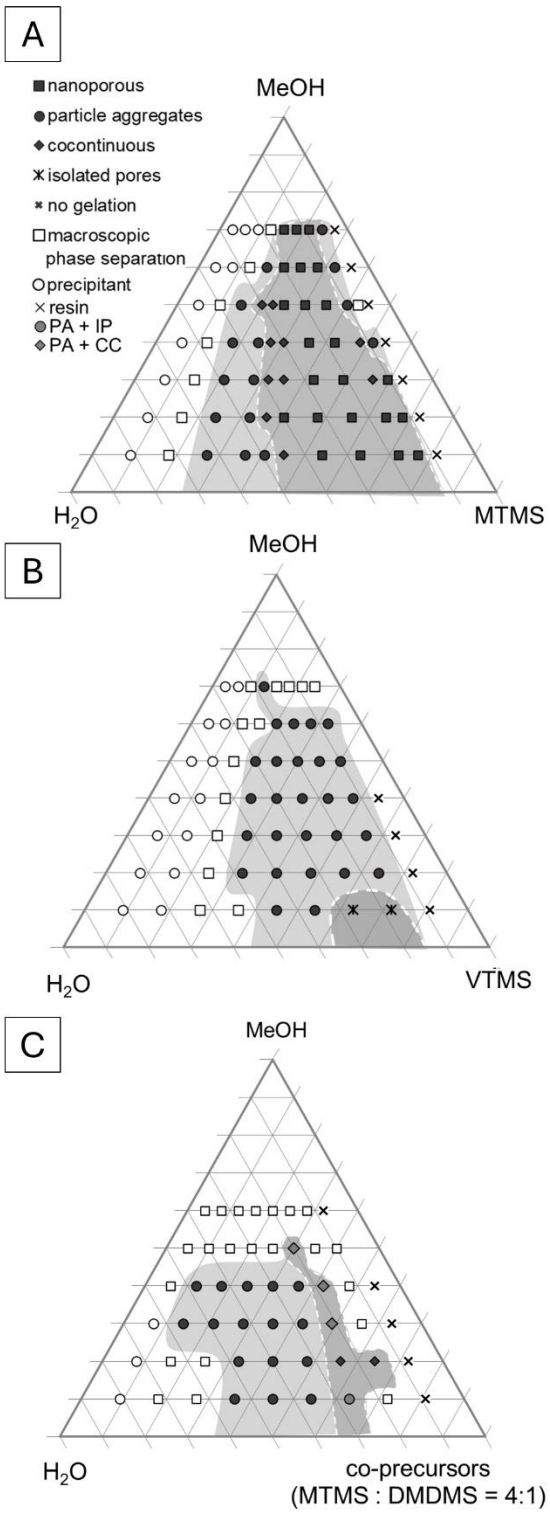

Fig. 40 Phase diagrams for the (a) TD-M2, (b) TD-V and (c) TD-D systems

5.3.2 Phase separation in TD-M2, TD-V, TD-D system

The phase diagrams for the $TD-M2$, $TD-V$ and $TD-D$ systems are presented in Fig. 40. Location of the nucleation & growth region as well as spinodal decomposition region were marked with two shades of grey. One can observe, for every of these systems how location of this thermodynamic regions (metastable N&G and unstable SD) changes for different precursors (MTMS, VTMS and mixture of MTMS and DMDMS in molar ratio 4:1 on Fig. 40a, b and c respectively).

For $TD-V$ and $TD-D$ systems the majority of the samples had the morphology type of particle aggregates. The $TD-M2$ system exhibits the largest range of binode and three types of monolithic structures (particle aggregates, cocontinuous and nanoporous). One difference comparing to

$TD-M1$ is the lack of presence of isolated pores type of structure. For MTMS and VTMS monoliths could be obtained up to 70% of methanol in the system. Systems with MTMS (both $TD-M2$ and as co-precursor $TD-D$) offer higher variety of structures types comparing to VTMS: n the $TD-V$ system only particle aggregates and isolated pores structures were obtained. The $TD-D$ system, based on a mixture of co-precursors (MTMS and DMDMS), resulted also in not homogenous morphologies, such as combination of particle aggregates and isolated pores or continuous morphology (marked as separate type of points in the ternary diagrams).

This analysis of structure types allowed to approximately establish areas of the metastable region of nucleation and growth and unstable region of spinodal decomposition. Binodal curve (including all monolithic samples) has the largest range for MTMS system ($TD-M2$).

Comparing $TD-M1$ system (presented in previous sub-section of this chapter) and $TD-M2$ (**Fig. 40**a) leads to an observation that the first system provides larger variety of structures, because the addition of catalyst is dependent on the water content, thus due to higher range of pH values in a system one can observe different pathways of the process, leading for example, to isolated pores type of structure, which was not observed for $TD-M2$.

The mean size of particles for $TD-M2$ and $TD-V$ system is presented in figures included in the attachment A5. In general the VTMS-based samples have larger sizes of particles.

The polydispersity index for $TD-M2$ and $TD-V$ system is presented on a ternary plot included in the attachment A6. It can be observed, that VTMS-based samples exhibit higher polydispersity in most cases. The highest polydispersity index for TD-M2 was 0.102, and for TD-V the value was 0.55.

5.3.3 Gelation kinetics in TD-M2, TD-V, TD-D system

The results of kinetics investigation are gathered in the attachments (A7- A9). The kinetics curves were measured for monolithic samples, but only in case the gelation time was long enough to capture the whole process. Furthermore, there was a few samples with a tendency to breaking during gelation ($TD-M2$ system) that were omitted, because the cracks would interfere the registered spectra and change the overall outcome of the experiment.

Three types of gelation kinetics curves were observed during the studies. The first one, presented in Fig. 41 a is characteristic for most opaque, monolithic samples. The sigmoid shape

is sharp and more or less symmetric. The second type, presented in Fig. 41b is not symmetric, and the upper inflection of the sigmoid curve is less sharp. In other words, the final absorbance values stabilizes for longer time, comparing to opaque samples. The third type is characteristic for samples with initial formation of a precipitant, followed by complete gelation within the whole volume of a sample (Fig. 41c). This process was observed, as initial turbidity followed by sedimentation of particles. The first type was characteristic for the definite majority of samples. All of the measured kinetics curves for the three systems: $TD-M2$, $TD-V$ and $TD-D$ are gathered in the attachments as A7, A8, A9 respectively. The graphs were prepared with logarithmic time scale, as for the constant methanol concentration, the difference between samples with highest and lowest value of precursor/water ratio (R) could be very high. It was observed that the time of gelation increases for higher concentrations of alcohol and with a decrease of precursor to water ratio, presumably to the fact the contribution of water was not sufficient for complete hydrolysis.

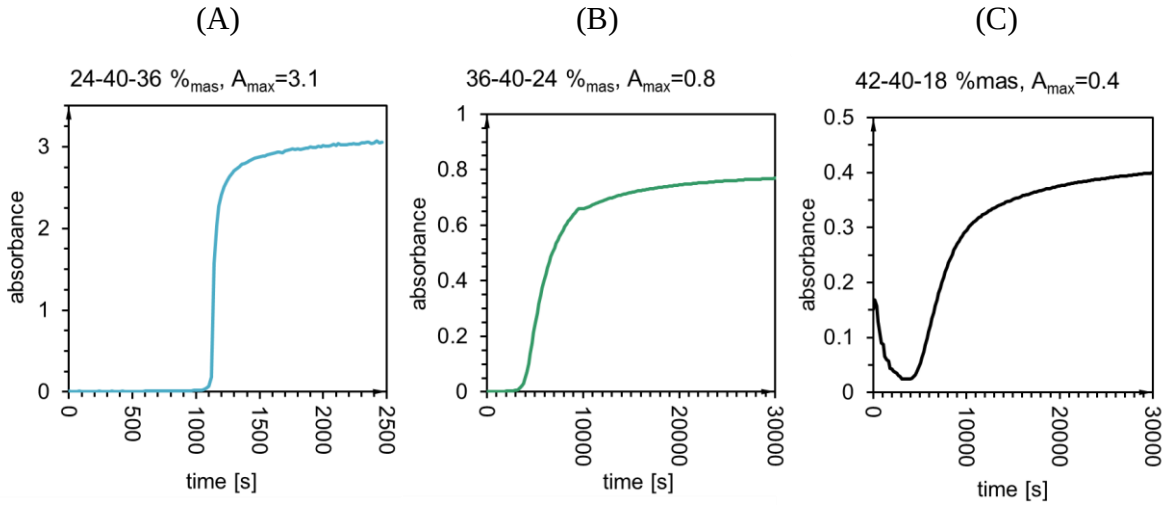

Fig. 41 Three types of the observed kinetics curves

The investigation offered a lot of qualitive analysis and comprehensive understanding of the sample's composition and final outcome – whether a monolithic sample can be obtained, what is the most likely type of morphology, particle size range and possible polydispersity of the system, as well as what is the kinetics, how long does the gelation takes place. What was still lacking, was a proposition of a mathematical description or type of analysis which would actually allow to compare the rate of gelation for different samples.

It was decided to interpolate the kinetics data ($A(t)$) with a spline and calculate the first derivative (dA/dt) (Fig. 42). As it was confirmed in previous chapter (*4. Analytical model of alcogels gelation kinetics*) the absorbance is directly proportional to mass, thus the kinetics in its normalised form can be interpreted as $m(t)$, thus the first derivative is dm/dt. The values

of the maximum value of the first derivative – the maximum condensation rate for $TD-M2$ and $TD-V$ were gathered in the attachment A10, and the values confirm the previously stated observations that gelation proceeds faster for VTMS as precursor, even despite larger size of the molecule and possible impact of steric effects.

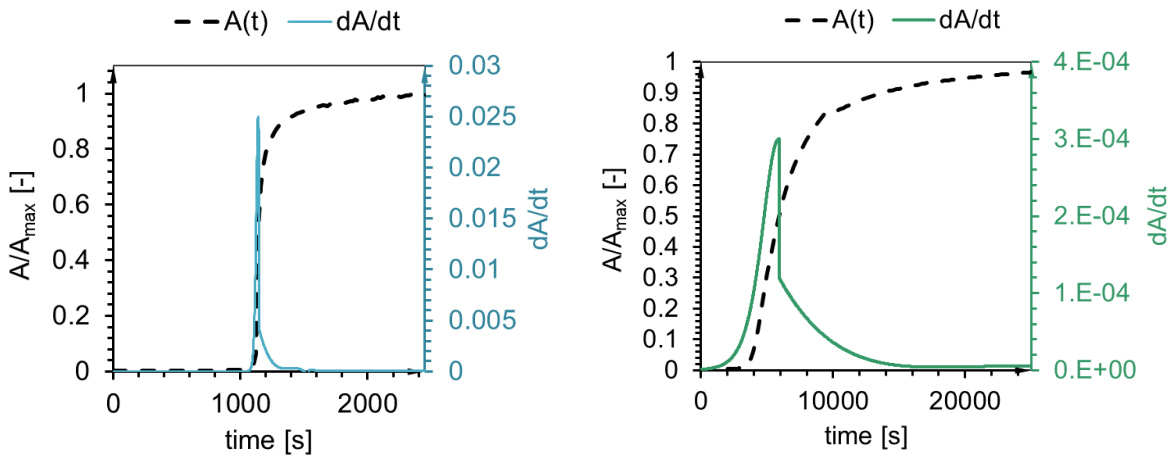

Fig. 42 The condensation kinetics data A(t) and condensation rate dA/dt for first and second type of a kinetics curve

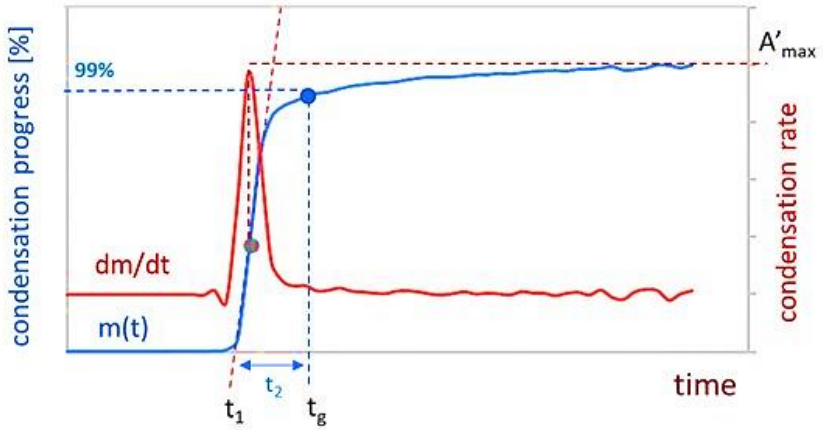

Fig. 43 Scheme of the analysis of a condensation kinetics curve [121]

The point of maximum condensation rate, $(dm/dt)_{max}$ was used to designate a tangent line to the kinetic curve $m(t)$, and the t_1 point which physical meaning is the end of first phase of gelation. The time gelation, for the syntheses studied in previous chapter (Chapter 4) $A-F$ was stated to correspond to 99% reaction progress, basing on the comparison of kinetic curve registered with spectrophotometer and gel-point captured with the tilting test-tube method. This assumption was used to propose a method of kinetics curve analysis. Subsequently, the time of the second phase was defined as a difference between time of gelation t_g and the time of nucleation t_1. All of the above considerations are schematically presented in Fig. 43.

In this case the phase 1 and 2 should be interpreted similarly as in previous chapter, according to Table 1. First phase corresponds to the genesis of a new cluster of gelling solid phase (or a new primary particle of amorphous silica structure), and the second phase to the intensive structure growth, occurring either due to N&G or SD mechanisms.

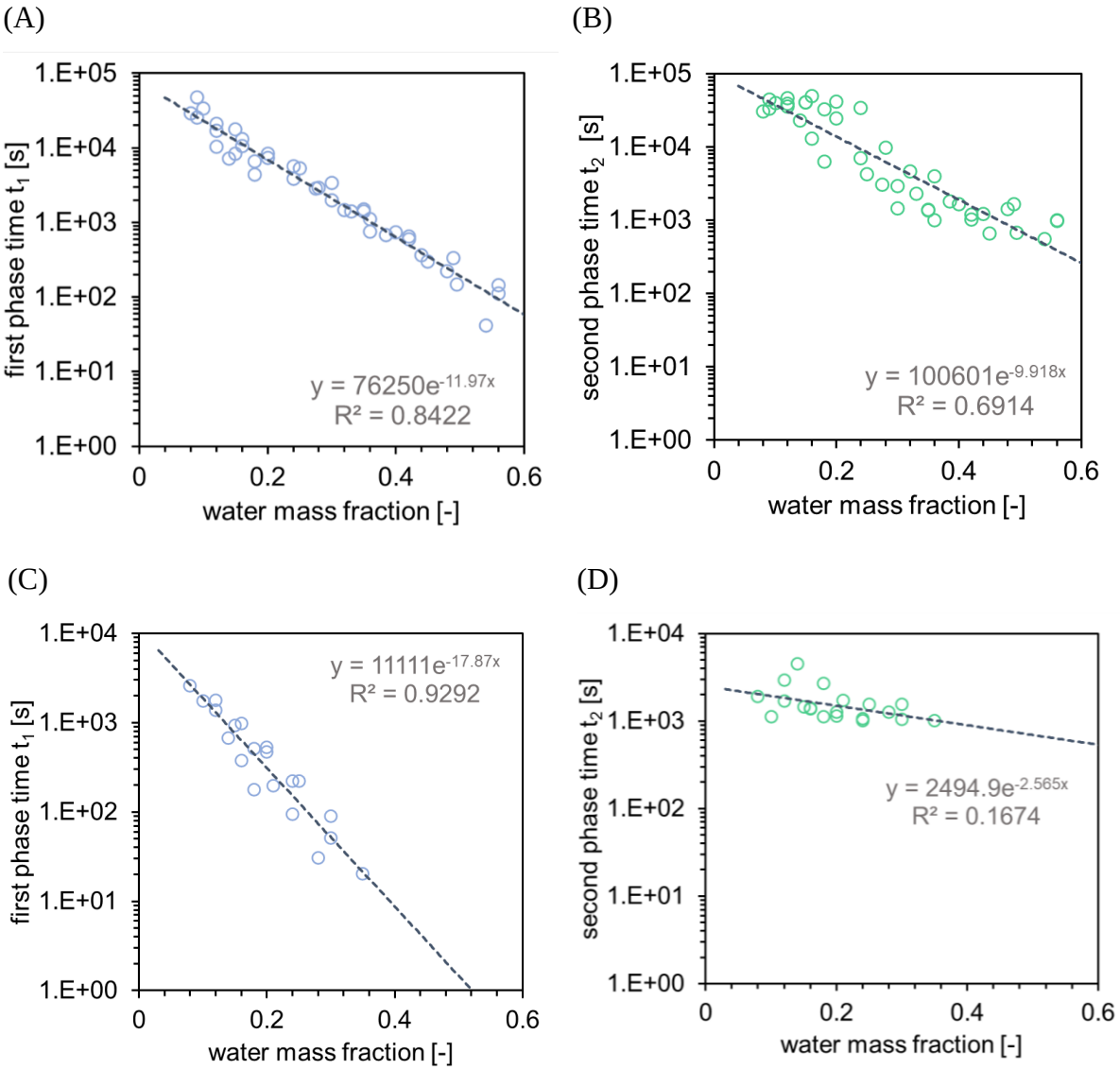

Fig. 44 Influence of water content on time of first and second phase for MTMS (a and b) and VTMS (c and d)

The results of the t_1 and t_2 for $TD-M$ and $TD-V$ are included in the attachment A11 and A12 respectively. It is observed that with higher water content in the initial chemical composition, the samples tends to gel faster. This tendency was proved valid for both MTMS and VTMS as precursors. Furthermore, the dependence was established to have an exponential character, as shown in Fig. 44.

The graph presents dependences between time of the first phase of gelation (nucleation) for MTMS (Fig. 44a) and VTMS (Fig. 44c), as well as time of the second phase of gelation (microscopic phase separation phase) (Fig. 44b and Fig. 44d for MTMS and VTMS respectively). This dependency can be explained by significant influence of water on reaction pathways – first of all, the amount of water is crucial to obtain full hydrolysis of the precursor molecules during the first step of the synthesis. The variable amount of water was the basic assumption of this research, however one has to be aware, that below certain mass fraction of water, the number of water molecules is not sufficient for full hydrolysis of the precursor molecules. Thus, the strong correlation between water content and time of the distinguished phases is understandable. It was also observed, that in general, VTMS gels faster comparing to MTMS, presumably to higher reactivity, despite possible steric effects for the larger molecule.

5.4 CONCLUSIONS

The ranges of occurrence of monolithic samples and their different morphologies were plotted in the form of ternary plots, providing a comprehensive knowledge about correlation between initial chemical composition of the reaction mixture and final product's properties.

The outline of binodal curve in a precursor-solvent-antisolvent ternary sol-gel system was designated experimentally, basing on the analysis of products' morphology. Four types of structure morphology were observed, same as in Nakanishi's work [49]. The studies indicate that within the area of the binode, the transition from NG mechanism to SD can be observed while increasing the precursor/water ratio. The exact location of the spinodal curves was not precisely established, however the obtained data provide an idea about location of spinodal decomposition area.

The condensation rate increases for lower concentration of solvent and lower values of precursor/water ratios. A new method of quantitative comparison of condensation process registered spectrophotometrically was proposed, based on kinetics data interpolation and calculation of first derivative corresponding to the value of condensation rate. This investigation allows to predict not only some of the structural properties of a system, as particle size distribution, polydispersity or porosity, but also the kinetics of gelation, which is very important aspect, especially for upscaling.

Presented research concerns the APD silica aerogels, which are based on relatively inexpensive precursors, reagents and drying technique. The porosity and volume shrinkage were measured only for the first investigated system (TD-M1) and the results looks promising

– even though APD was for a long time considered as a not suitable method for aerogel preparation, majority of the monolithic samples exhibit high porosities values (above 70%), reaching up to 93%.

The studies has a potential to advance the state of the art by providing knowledge about controlling the overall gelation process of synthesis of silica aerogels, as well as predict their condensation kinetics and some of the final's product structural properties, such as porosity, secondary particles mean size and polydispersity index.

6. DIFFUSION/REACTION LIMITED SECONDARY PARTICLES' AGGREGATION

6.1 OBJECTIVE

The fourth part of this thesis is focused on developing a model of organoalkoxysilane-based alcogels condensation kinetics. In difference to the analytical model presented in previous section (*Chapter 4*), this approach can follow not only condensation kinetics, but the morphology of the formed structure as well. The goals of this part were as follows:

- developing a computational approach based on a cellular automaton (CA) system that can mimic the kinetics gelation process (aggregation of secondary particles in this case);
- developing a computational approach based on a cellular automaton system that can, to some extent, represent the morphology of wet-gel;
- proposing a method for correlation between model parameters and experimental parameters, followed by this method verification;
- analysis of the applicability of the developed cellular automaton as a representation of gelation of organoalkoxysilane-based alcogels.

The hypothesis for this section was formulated as follows:

4^{th} hypothesis

A cellular automaton can be applied as a simplified representation of the gelation process, in particular for the aggregation of secondary organoalkoxysiloxane-based particles. The model parameters can be correlated with experimental synthesis conditions with the Arrhenius equation.

6.2 NUMERICAL METHODOLOGY

In order to implement the process of aggregation of organoalkoxysilane-based secondary particles (SP) during condensation, a cellular automaton system was developed.

This kind of system is based on n-dimensional, divided into a regular grid of cells (Fig. 45), computing domain with periodic boundary conditions (Fig. 46). According to the main idea of cellular automata, each cell can be in one of given number of states. The evolution of each cell proceeds simultaneously during each time step, depending on the given cell's state from the previous step and the state of its adjacent neighbours.

In the studied case, which is aggregation of secondary particles, a cell can be described by one of the two possible states: it can be either occupied by a secondary particle or empty (Fig. 45). The number of occupied cells depends on the SP concentration – the first introduced model parameter (c). The particles diffuse randomly in order to mimic Brownian motion. When two particles appear in the adjacent cells, a condensation reaction between them can occur, depending on the value of the second model parameter: reaction probability (P).

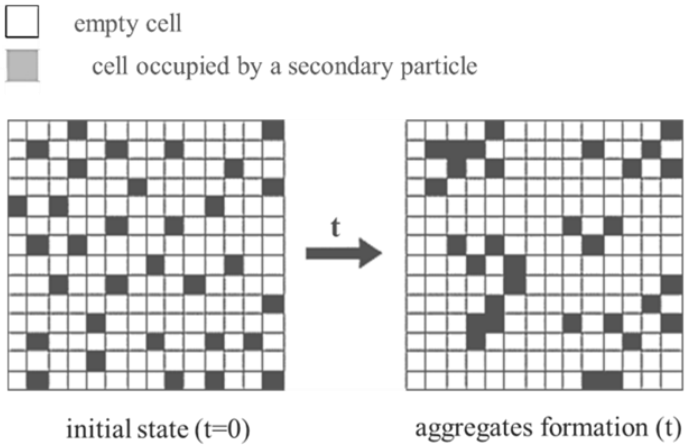

Fig. 45 Scheme of the cellular automaton behaviour

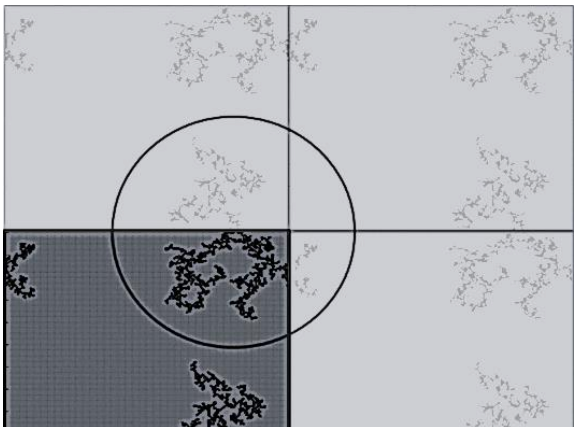

Fig. 46 Scheme of system periodicity [122]

In this sort of systems we can distinguish two main regimes: aggregation limited by diffusion (DLA, or DLCA for cluster aggregation) or reaction (RLA, or RLCA). When reaction probability P is significantly lower than 1, we enter the RLCA regime. The influence or reaction probability (also referred as sticking probability in the literature) is quite well

established – the higher probability the more branched and linear are the structures, and for low RLA regime more dense and compact structures are obtained (Fig. 47).

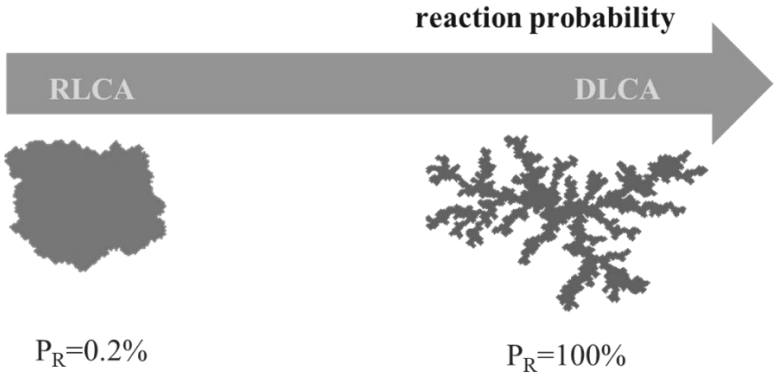

Fig. 47 Influence of reaction probability on aggregate morphology (initial results)

When the condensation reaction between SP occurs they start to behave as one aggregate, and from this point they move together. One of the simplification in the presented model is neglected possibility of the bond breakage, which means that once created aggregate cannot fall apart.

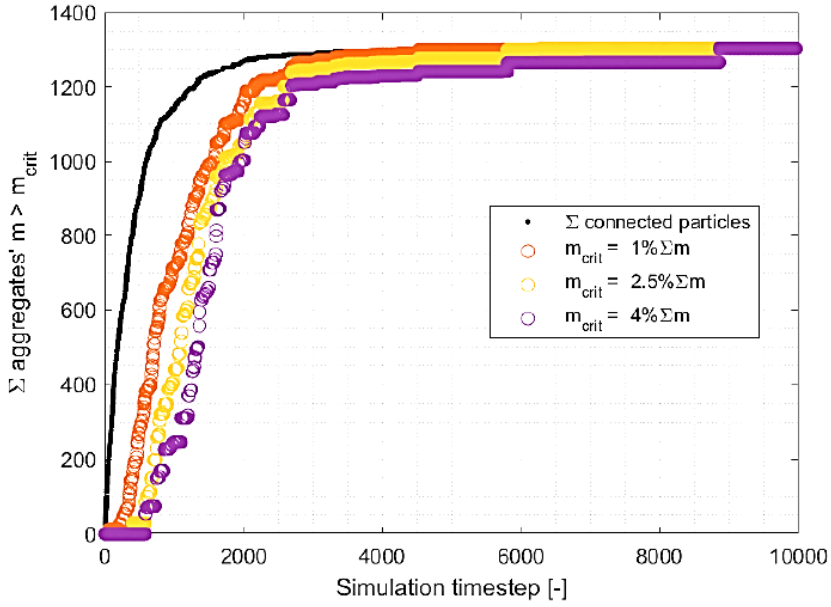

Fig. 48 Impact of an aggregate threshold size on condensation kinetics curve for three dimensional system [121]

The probability of motion (diffusion) P_D is dependent on the size of a given aggregate. It's reversibly proportional to the size of an aggregate, according to the Einstein-Stokes equation for diffusion of spherical particles in low Re numbers ($D \sim 1 / r$).

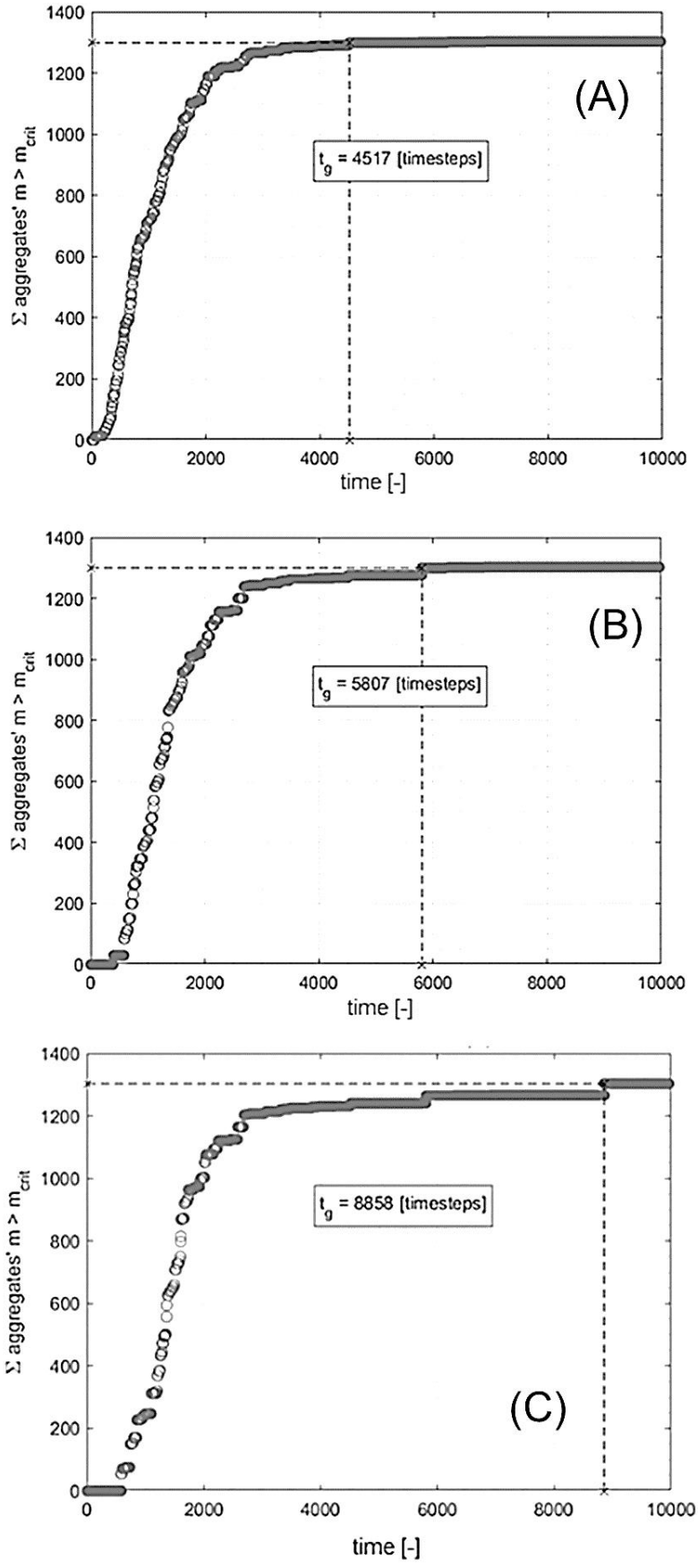

Fig. 49 Impact of an aggregate threshold size on gel-point location on the curve (threshold size: a – 1%, b – 2.5%, c – 4%) [122]

$$D = \frac{k_B T}{6\pi\eta r} \tag{6.1}$$

$$P_D \sim \frac{1}{r} \tag{6.2}$$

Where D is the diffusion coefficient, k_b – Boltzmann constant, T – temperature, η – dynamic viscosity, r – radius of a particle.

The simulation stops when all of the SP are connected into one cluster. In percolation theory this final state is called as large cluster or spanning cluster.

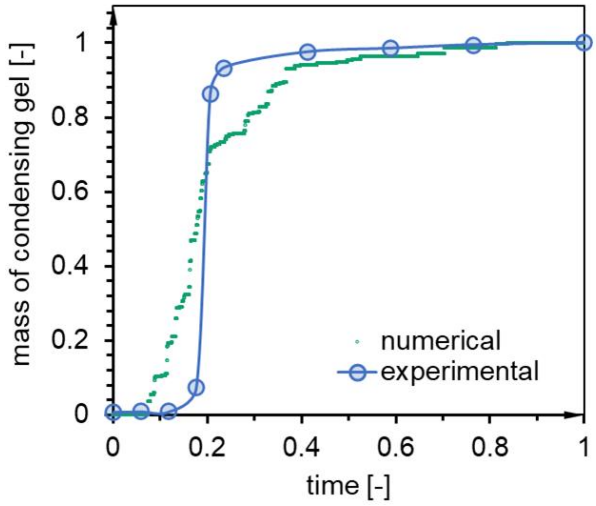

Fig. 50 Qualitative comparison of experimental and numerical condensation kinetics curve [122]

The goal was to designate condensation kinetics and compare them with experimental one. In order to achieve that goal, a numerical procedure that would be analogical to the experimental one, had to be developed. Thus, it was assumed that in order to detect an aggregate, first it has to reach a certain detectable threshold size. The value of this threshold size, was chosen in such way, to obtain the highest resemblance to the experimental shapes of the curves. Thus, the first criterium was to observe the first kinetics curve inflection (unlike the black line in Fig. 48). The second criterium was to obtain the gel point just after the second inflection of the curve (Fig. 49). The second criterium might seem arbitrary, however it is just an initial model assumption. Furthermore, this criterium was supported by observations of gel points for certain experimental samples, which were chosen for the model validation in the further part of this chapter (the samples selection is discussed in next subsections).

The resemblance of final kinetics curves obtained experimentally and numerically is presented in Fig. 50. At this point, there was no correlation between numerical and experimental

parameters, just a qualitative comparison of the dependences of condensation progress on time for experimental and numerical system.

After reaching the detectable size of an aggregate, the arbitrary total mass of condensed product (proportional to the number of SP within detectable clusters) is growing until the whole structure is interlinked. The kinetics curves were analysed according to the procedure described in Chapter 5 (Fig. 43).

The obtained structures were evaluated in terms of their porosity, determined as the number of not occupied cells within a volume of a certain spherical shell with certain thickness. A representative area of the structure had to be selected. It was chosen to select a mean distance of each particle to the mass centre of an aggregate, as this value could be precisely determined and because the local porosity seemed to be approximately constant around this point. Thus, the representative area for porosity designation was chosen to be $< 80\%\,\bar{r},\ 120\%\,\bar{r} >$. The scheme showing an exemplary aggregate with the representative spherical shell volume is presented in Fig. 51a. The exemplary dependence of porosity on distance from the centre of an aggregate is shown in Fig. 51b.

(A) (B)

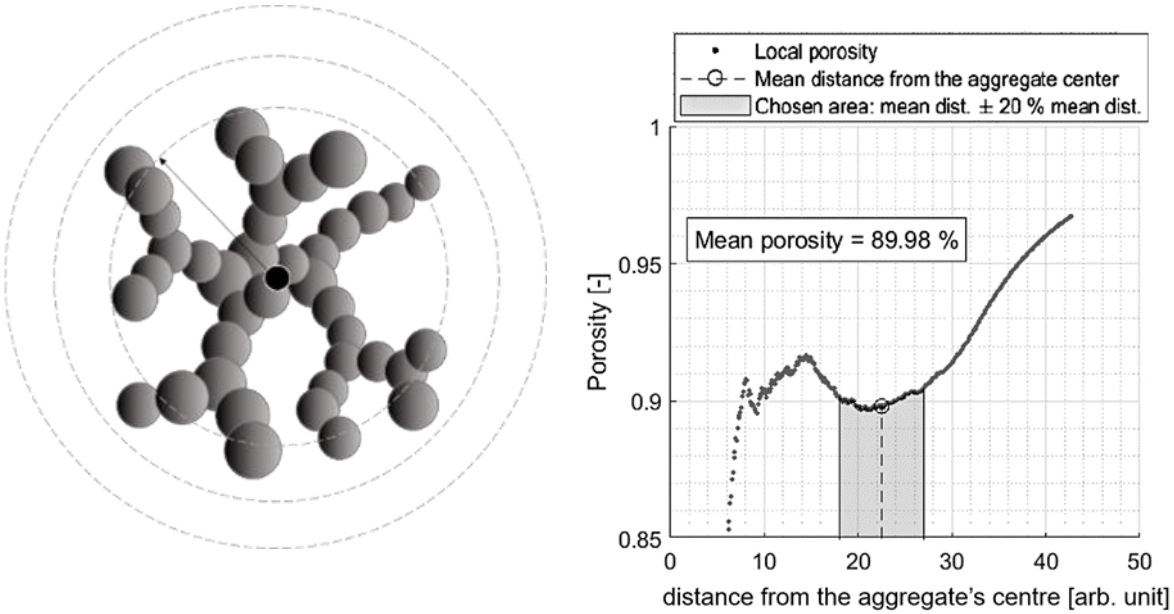

Fig. 51 (A) scheme of the representative spherical shell volume, (B) exemplary dependence of porosity on distance from the centre of an aggregate [121]

In this thesis two type of cellular automata systems were studied:

a) the simpliefied, two dimensional ($n = 2$)
b) the advanced, three dimensional ($n = 3$)

Naturally, the 3D system is more accurate and offers more results for interpretation and validation. The work on the two dimensional system was an initial approach used for a simplification, while developing an actual, three dimensional model. However, the results even for the simplified 2d system were found interesting, and it was decided to show the comparison between the results and pros and cons of both system. Thus, the differences in assumptions in these two systems were gathered in Table 6.

Table 6 Comparison of the developed 2D and 3D cellular automata assumptions

Aspect	*Two dimensional* $n = 2$	*Three dimensional* $n = 3$
Neighbourhood	Moore's type of neighbourhood	
	Cell *i* has 8 neighbours	Cell *i* has 26 neighbours
Diffusion	Probability of motion uniform for each size of an aggregate (an initial simplification)	Probability of motion correlated with an aggregate size by Einstein – Stokes equation (Eq. 6.1)
Reaction probability	Tested for 4 chosen values: 0.001, 0.01, 0.1, 1 (studied cases presented in Fig. 52)	Tested for 5 chosen values: 0.0005, 0.001, 0.01, 0.1, 1 (studied cases presented in Fig. 52)
Tested concentrations	1, 5 and 12.5% of number of cells in computing domain (studied cases presented in Fig. 52)	0.5, 1, 2, 3 and 4 % of number of cells in computing domain (studied cases presented in Fig. 52)

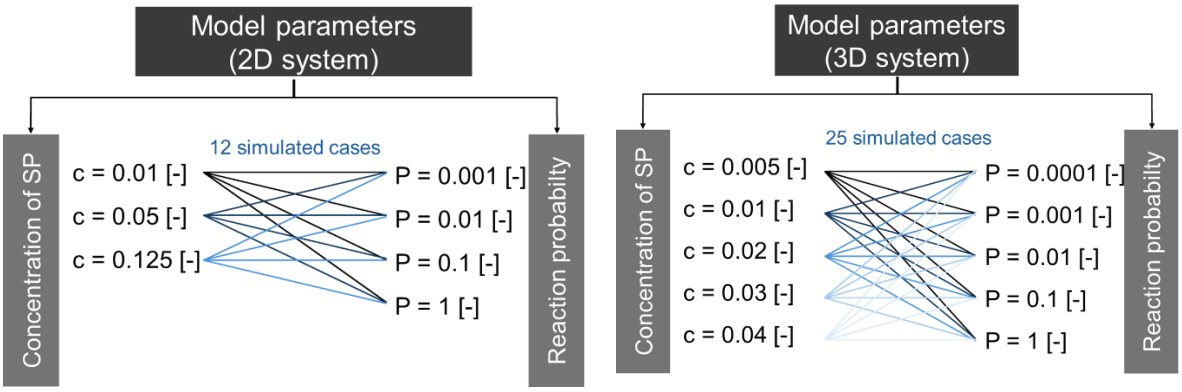

Fig. 52 Model parameters chosen for 2D (left) and 3D system (right) study case

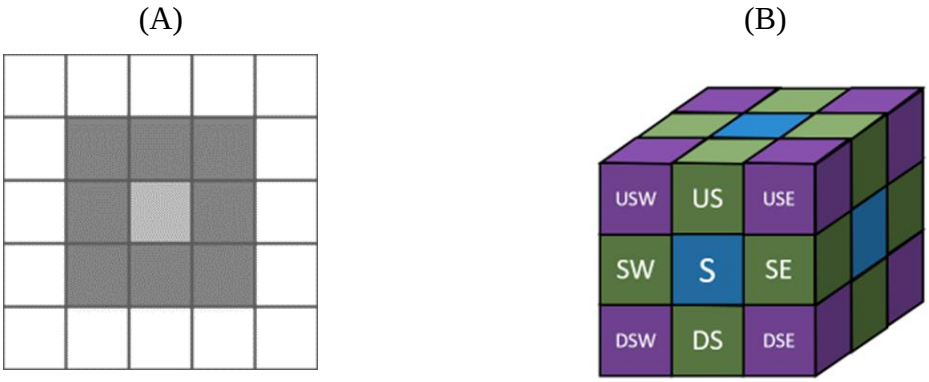

Fig. 53 Moore type of neighbourhood for (a) 2d, (b) 3d system

6.3 EXPERIMENTAL METHODOLOGY

6.3.1 Experimental verification for the two dimensional approach

The experimental samples were prepared according to the two-step, acid-base synthesis described thoroughly in Chapter 4 and 5. In this section of the thesis MTMS (methyltrimethoxysilane) was used as a precursor, methanol as solvent, distilled water as anti-solvent, oxalic acid (0.01 $[mol/dm^3]$) as the catalyst of hydrolysis and ammonia solution (1 $[mol/dm^3]$) as the base catalyst of condensation. The precursor and acid were purchased from *Sigma-Aldrich* (St. Louis, MO, USA), the solvent from *Stanlab* (Stanlab, Lublin, Poland) and the base from *Eurochem BGD*, (Tarnów, Poland) .

The molar ratios of reagents used during synthesis are given in Table 6.2. After mixing of precursor and solvent (MTMS and MeOH), the hydrolysis was initiated with addition of the acid and carried out for 1 hour. After this time, a proper amount of the base catalyst was

added to initiate the gelation. Solution was stirred vigorously for 30 seconds, then the stirring element was removed and subsequently 2.5 $[ml]$ of reaction mixture was transferred into a polystyrene cuvette which was inserted into the spectrophotometer, with pure methanol as a reference sample (blank). The kinetics of gelation was measured for wavelength 633 $[nm]$. The rest of the prepared, gelling solution was observed to determine the gel-point values by the tilting test tube method.

The chemical compositions of the samples are given in Table 7.

Table 7 Comparison of two and three dimensional cellular automaton systems

Sample Nr	*Molar composition [mol]*					*Conc. NH_4OH [mol/dm^3]*
	MTMS	*MeOH*	*H_2O*	*Oxalic acid*	*NH_4OH*	
1	1	7.36	14.87	1.34	0.13	0.19
2	1	7.36	14.93	1.34	0.07	0.09
3	1	7.36	16.52	1.49	0.15	0.20
4	1	7.36	18.17	1.64	0.16	0.21
5	1	7.36	19.78	1.79	0.22	0.28
6	1	7.36	19.82	1.79	0.18	0.22
7	1	7.36	19.86	1.79	0.13	0.17
8	1	7.36	19.91	1.79	0.09	0.11
9	1	7.36	21.47	1.94	0.19	0.23
10	1	7.36	23.08	2.09	0.26	0.30
11	1	7.36	23.12	2.09	0.21	0.24
12	1	7.36	23.17	2.09	0.16	0.18

6.3.2 Experimental verification for the three dimensional approach

Experimental samples presented in this section were used for verification of the three dimensional CA approach. A two-step, acid-base sol-gel synthesis was applied with the same precursor, solvent, anti-solvent, acid and base catalyst as described in previous sub-section (*6.4.1 Experimental verification for the two dimensional approach*). A bullet-point summary is written below:

- precursor: methyltrimethoxysilane (MTMS), *Sigma-Aldrich* (St. Louis, MO, USA);
- solvent: methanol (MeOH), *Stanlab*, (Lublin, Poland);
- anti-solvent: distilled water (own production);
- Hydrolysis catalyst: oxalic acid, concentration 0.01 $[mol/dm^3]$, *Sigma-Aldrich* (St. Louis, MO, USA);

– Condensation catalyst: ammonia solution, concentration $1\,[mol/dm^3]$, *Eurochem BGD*, (Tarnów, Poland).

The chosen samples, in terms of both preparation methodology and kinetics measurement results were described already in the Chapter *4. Analytical model of alcogels gelation kinetics*. In brief summary, the samples were prepared in such a manner, to maintain a constant MTMS/MeOH vol. ratio $1:2$. The volume of aqueous catalyst solutions was variable. Chemical composition are presented in Table 8. The samples were studied by UV-Vis spectrophotometer, with pure methanol set as reference and wavelength $633\,[nm]$. The remaining, gelling solution was observed the gel-point values by the tilting test tube method.

Table 8 Chemical composition of the studied MTMS-based alcogel samples

volume proportions [ml]				*Number of moles [mol]*				
Sample Denotation	*MTMS: MeOH*	*: Acid*	*: Base*	*MTMS*	*MeOH*	*Water*	*Acid*	*Base*
A	1:2	0.9	0.9	0.0069	0.049	0.050	$1.2\cdot10^{-9}$	$5.9\cdot10^{-8}$
B		1.0	1.0			0.055	$1.2\cdot10^{-9}$	$6.3\cdot10^{-8}$
C		1.1	1.1			0.061	$1.3\cdot10^{-9}$	$6.7\cdot10^{-8}$
D		1.2	1.2			0.066	$1.4\cdot10^{-9}$	$7.0\cdot10^{-8}$
E		1.3	1.3			0.072	$1.4\cdot10^{-9}$	$7.4\cdot10^{-8}$
F		1.4	1.4			0.077	$1.5\cdot10^{-9}$	$7.7\cdot10^{-8}$

6.3.3 Estimation of the model parameters (3D approach)

One of the goals (as stated in the *6.1 Objective* subsection) was too propose *"a method for correlation between model parameters and experimental parameters"* and provide a verification of this method. In case of this computational approach, there are two main model parameters:

– concentration of secondary particles in the system;
– probability of reaction between adjacent particles.

The first parameter – the SP concentration, can be designated by a straight forward analytical method. In the case of a cellular automaton, the concentration can be interpreted as a ratio of the SP number to the total number of cells within the representative volume element.

In real, experimental system there is no cells, so this approach needs to be converted from number concentration into volume concentration. Thus, the SP concentration parameter should be interpreted as ratio of total cells (particles) volume to the total RVE volume (or alcogel volume, V_{al}).

When considering an actual experimental system, to designate the total volume of the secondary particles (V_{sp}) we need to multiply their number (n_{sp}) and volume of a single particle (V_{sp1}). The number of SP can be established by dividing the total mass of dried alcogel (an aerogel) m_s by the mass of a single particle (m_{sp}). The mass of a single particle is equal to multiplication of skeleton density (ρ_s) and the volume of a single particle. Simplifying of this equation leads to the final form, where the concentration can be designated with only three, easily possible to measure parameters: mass of dry sample, skeleton density and alcogel volume (Eq. 6.3).

$$c = \frac{V_{sp}}{V_{al}} = \frac{n_{sp}V_{sp1}}{V_{al}} = \frac{m_s}{m_{sp}}\frac{V_{sp1}}{V_{al}} = \frac{m_s}{V_{sp1}\cdot\rho_s}\frac{V_{sp1}}{V_{al}} = \frac{m_s}{\rho_s V_{al}}\,[\%_{vol}] \tag{6.3}$$

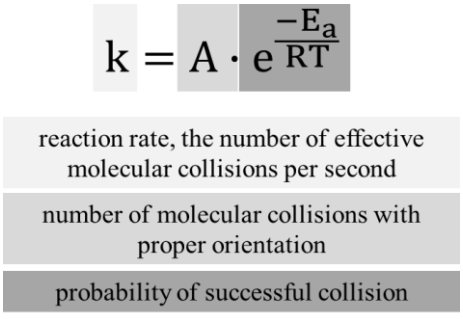

Fig. 54 Interpretation of the Arrhenius equation

The second model parameter – the probability of an effective collision (often referred to as simply "reaction probability", or sometimes in literature as "sticking probability" [80]). As the goal of the thesis was to propose a correlation of this parameter with experimental conditions, it was decided to use and verify application of the Arrhenius equation. The interpretation of the Arrhenius equation was schematically presented in Fig. 54. The equation correlates the reaction rate (k) with number of molecular collisions with proper orientation (the physical meaning of the Arrhenius constant - A), and the probability of a successful collision (the physical meaning of the exponential factor $\exp(-E/RT_g)$). This exponential factor was assumed to be proportional to the model parameter - reaction probability in the developed cellular automaton.

To establish the sought probability parameter, it was assumed that the reaction rate is reversibly proportional to the time of reaction (gelation time), thus $t_g \propto 1/k$, the Arrhenius equation (Eq. 6.4) can be transformed to its linear form (Eq. 6.5) with E/R as its slope, A' as an intercept (new constant, dependant on the Arrhenius constant), $\ln t_g$ as an ordinate and $1/T_g$ as an abscissa.

$$k = A \exp\left(-\frac{E}{RT_g}\right) \tag{6.4}$$

$$\ln t_g = A' + \frac{E}{RT_g} \tag{6.5}$$

$$p = A' \cdot \exp\left(-\frac{E}{RT_g}\right) \tag{6.6}$$

$$P = \left[A' \cdot \exp\left(-\frac{E}{RT_g}\right)\right] dt \tag{6.7}$$

Basing on these values, the probability parameter could be designated according to the above described interpretation of the Arrhenius equation. This parameter is assumed to be an equivalent of an effective collision probability and it is the main model parameter within the presented research. The probability rate (p) was designated directly based on the Arrhenius equation (Eq. 6.6), while probability P was multiplied by the time step value (characteristic for each investigated synthesis from Table 8) (according to Eq. 6.7).

6.4 RESULTS OF THE TWO-DIMENSIONAL (SIMPLIFIED) APPROACH

Fig. 55 depicts influence of transition from diffusion to reaction limited aggregation on morphology of obtained structures. The model parameters were concentration of secondary particles c (the percentage of cells occupied by a particle within a computing domain), and probability of reaction P. The chosen values of these parameters are P = 0.001, 0.01, 0.1, 1 and $c = 1,5$ and 12.5% according to the Table 6 and scheme included in Fig. 52.

Analogically, Fig. 56 presents the influence of the same transition on the shape of condensation kinetics curves.

The following observations can be made, based only on the simplified (two dimensional) version of the aggregation-driven structure formation:

- For each of the tested concentration values one can observe, the structures become more dense and compact with the decrease of the probability value. This is a consequence of the transition into the reaction-limited aggregation: when the probability of merging particles is lower, they are more likely to penetrate the structure deeper, until they finally join the aggregate at some point.
- The time of the simulation decreases when the system approaches diffusion limited regime due to higher probability of reaction between adjacent particles. The time can be

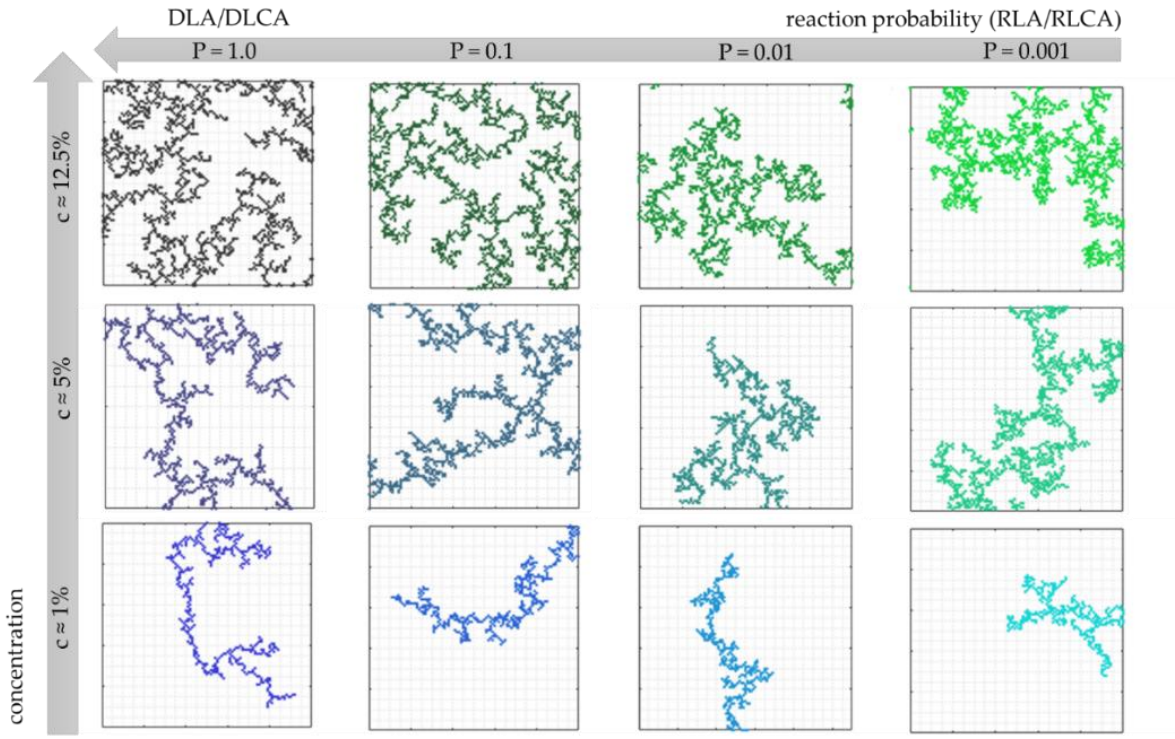

Fig. 55 CA-generated final wet–gel structure visualizations depending on the model parameters values [122]

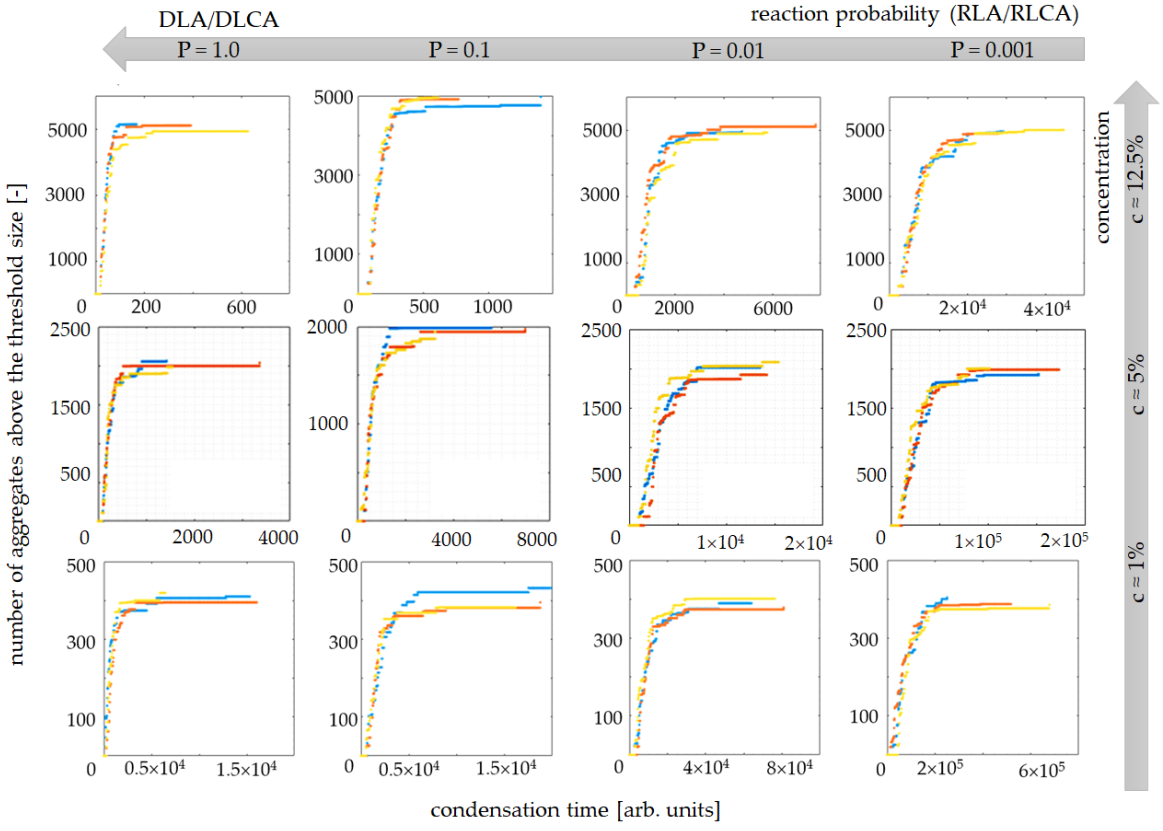

Fig. 56 CA-generated condensation kinetics curves, depending on the model parameters values. Each variant was simulated 3 times (blue, orange and yellow line) which indicates repeatability of the runed simulations [122]

- also associated with the gelation time, i.e. when all secondary particles are interlinked, thus the system behaves as solid matter instead of a liquid.
- The same tendency can be observed when increasing the concentration of the secondary particles in the system. Naturally, a higher number of SP within the computing domain is also responsible for the higher probability of collision, even with the same "reaction probability" parameter value.

Additional feature of the presented model was registering the size distribution of the clusters during the condensation process. An insight into such exemplary results is presented in Fig. 57. This option was not further explored within the presented thesis, nevertheless, it creates a great potential of studying system kinetics and dynamics, and comparison with experimental data, obtained, for example by the dynamic light scattering technique.

Table 9 The chemical composition and the values of designated gelation time for the investigated samples

Sample Nr	*Molar composition [mol]*					*Conc. NH_4OH [mol/dm^3]*	*Gel. time [s]*	*S.dev [s]*
	MTMS	*MeOH*	*H_2O*	*Oxalic acid*	*NH_4OH*			
1	1	7.36	14.87	1.34	0.13	0.19	913.67	129.62
2	1	7.36	14.93	1.34	0.07	0.09	2445.00	141.07
3	1	7.36	16.52	1.49	0.15	0.20	737.67	329.82
4	1	7.36	18.17	1.64	0.16	0.21	540.67	147.78
5	1	7.36	19.78	1.79	0.22	0.28	634.67	49.00
6	1	7.36	19.82	1.79	0.18	0.22	366.00	214.00
7	1	7.36	19.86	1.79	0.13	0.17	966.67	15.00
8	1	7.36	19.91	1.79	0.09	0.11	1411.67	128.00
9	1	7.36	21.47	1.94	0.19	0.23	328.00	129.90
10	1	7.36	23.08	2.09	0.26	0.30	324.00	7.94
11	1	7.36	23.12	2.09	0.21	0.24	301.67	158.66
12	1	7.36	23.17	2.09	0.16	0.18	640.00	17.32

It can be clearly observed, that in initial state of the system ($t = 0$), the majority of the particles are single (not within an aggregate). Some of the particles are already interlinked, because the model assumes that when generating random position of particles, if particles appear in neighbouring cells, the reaction between them can occur even before the diffusion starts. It can be observed on the scheme, that during the condensation, the total number of aggregates decreases. The distribution is shifted towards bigger aggregates, until all of the particles are completely interlinked (one "giant aggregate" was formed, $t = 1427$).

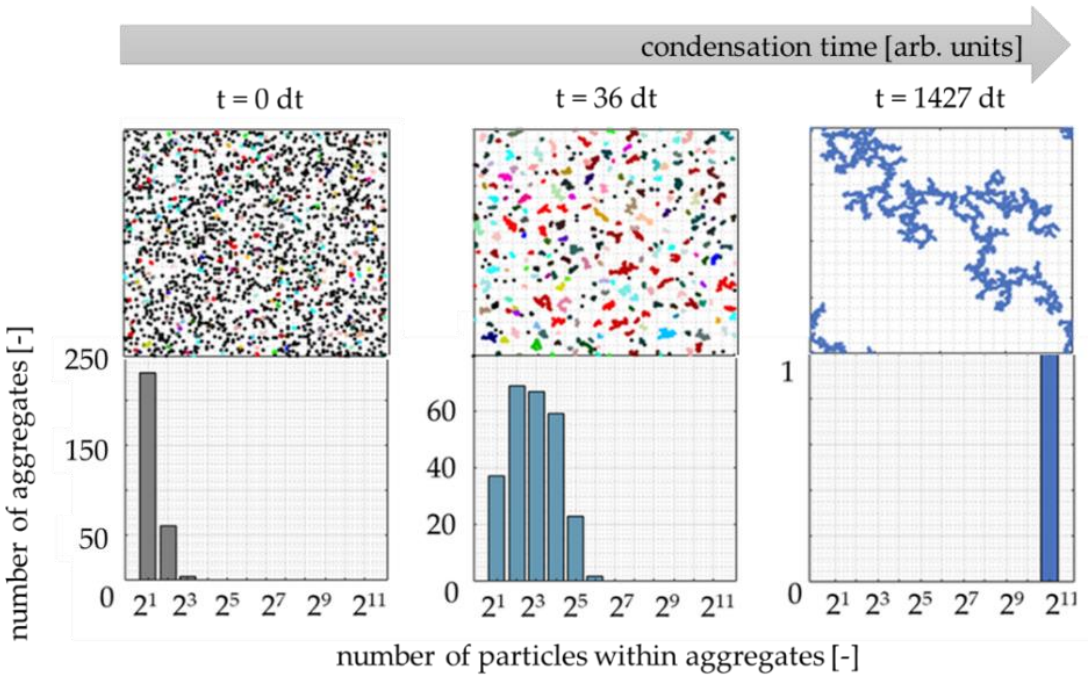

Fig. 57 The evolution of the aggregate size distribution during the process of condensation (simulation parameters: c = 5%, P = 1). Initial colours of the aggregates are randomly generated for easier distinction [122]

The experimental results of the gel points are presented in Table 9. The experimental and numerical kinetics curves are presented in Fig. 58, with additionally potted gel-points to show the resemblance on a qualitative level, thus acceptable assumption of the threshold size value. The gel-points values established for experimental samples with the tilting test tube method are plotted in Fig. 59. The experimental dependence was approximated by the power function:

$$t_{gel} = 36.2\left(n_{NH_4OH}/n_{MTMS}\right)^{-1.5} \tag{6.8}$$

with $R^2 = 0.85$. The power function is also a good approximation of the gelation time established computationally (Fig. 59b) depending on the reaction probability (Eq. 6.9, with a and n parameters gathered in Table 10). By comparing Eq. 6.8 and 6.9 it was observed that the reaction probability is an increasing function of the molar ratio of condensation catalyst to the precursor (MTMS) (Eq. 6.10). The exponent α equals between $2-3$ depending on the studied variant. By comparing Eq. 6.10 with Eq. 6.6 one can observe the correlation between activation energy and the base catalyst/precursor ration according to the Eq. 6.11.

$$t_{gel} = a \cdot P^n \tag{6.9}$$

$$P \propto \left(n_{NH_4OH}/n_{MTMS}\right)^{\alpha} \tag{6.10}$$

$$E \propto -ln\left(n_{NH_4OH}/n_{MTMS}\right) \tag{6.11}$$

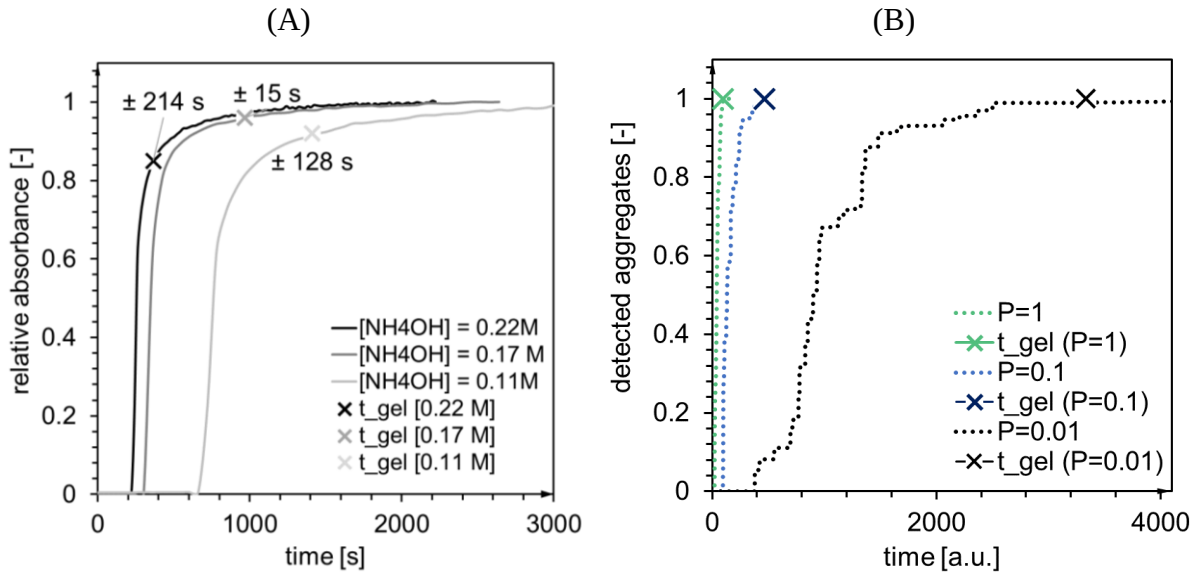

Fig. 58 The condensation kinetics curves obtained (a) experimentally (UV–Vis spectrophotometry) and (b) numerically. The gelation time values (cross points) estimated by (a) tilting test tube method and (b) assuming the gelation time point occurs for structure cross-linked in 99%. [122]

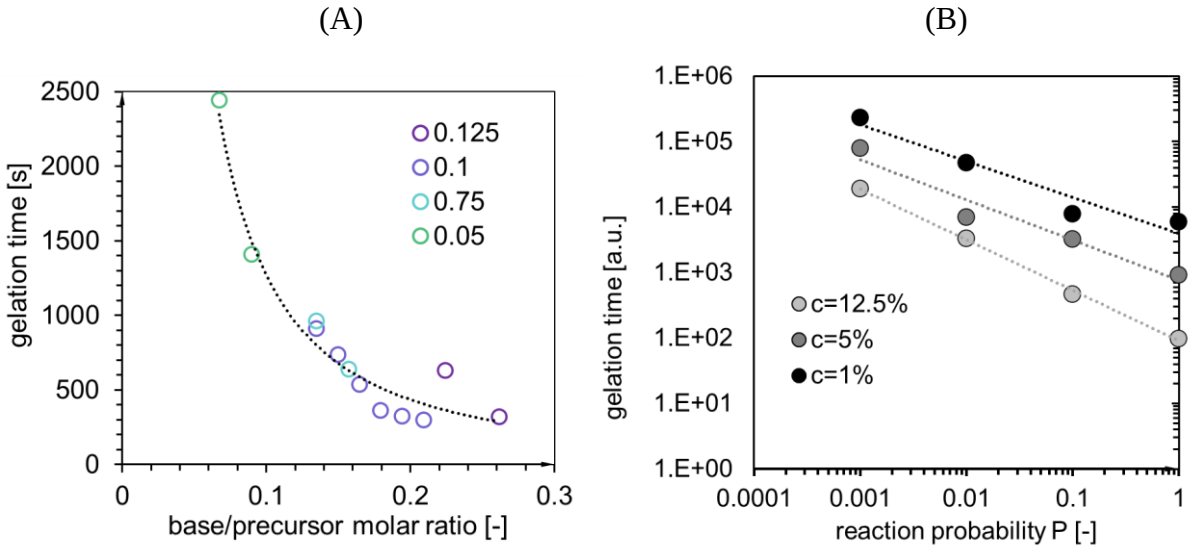

Fig. 59 The dependence of (a) gelation time on base/precursor molar ratio and (b) simulation results of the gelation time on the reaction probability (plotted with logarithmic scale) [122]

Table 10 The parameters A and n, describing the power dependence of the gelation time on the reaction probability (numerical results) [122]

SP concentration [%]	*A parameter*	*n parameter*	R^2
1	3901.8	−0.56	0.94
5	761.8	−0.61	0.95
12.5	90.1	−0.77	1.00

6.5 RESULTS OF THE THREE DIMENSIONAL APPROACH

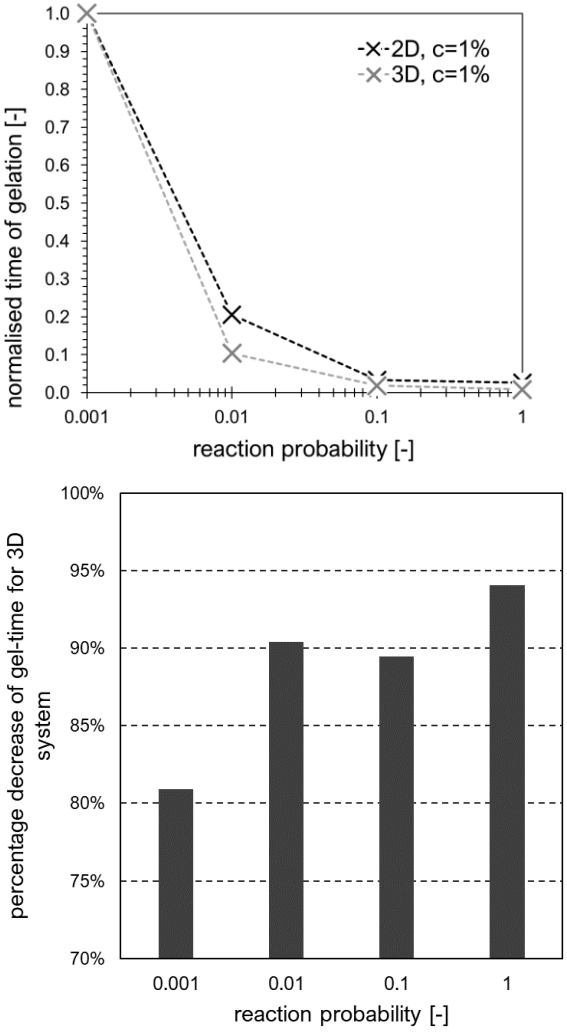

Fig. 60 Dependence of normalised time of gelation on probability value for 2D and 3D system (upper); the values of percentage decrease of gelation time for the 3D system (bottom)

The first analysed aspect of the two and three dimensional cellular automaton system, was the relation between time of gelation and probability parameter (P). The dependence is plotted in Fig. 60. The time of gelation is normalised in the following manner: $t_g(P)/t_g(P=1)$. The dependence of normalised time of gelation shows the effect of probability on both system, and it can be observed that the dependence looks very similar. However, the numerical values for 3-dimensional are lower. The values of percentage decrease for the 3D system are plotted in the bottom part of Fig. 60. It can be observed, that the higher is the probability, the higher is the difference between time of gelation for 2D and 3D system. This can be explained by the system structure. With the Moore neighbourhood, in 2D system a particle has 8 neighbours, while in 3D system a given particle has 26 (Fig. 53). It means, that for the same value of SP concentration in

a system in 3D system a given particle is more likely to have neighbours even in the initial state. In this case, for concentration 1%, in 2D system within Moore neighbourhood on average we will have 0.9 particle, and for 3D system 2.7 particles. It explains, that for the same concentration of particles in a system, the distances seem smaller in 3D system, as a given particle has more neighbouring cells.

Exemplary structure and kinetics curve for the three dimensional system is presented in Fig. 61. Both the morphology and the kinetics curve exhibit resemblance to the experimental results presented in previous sections.

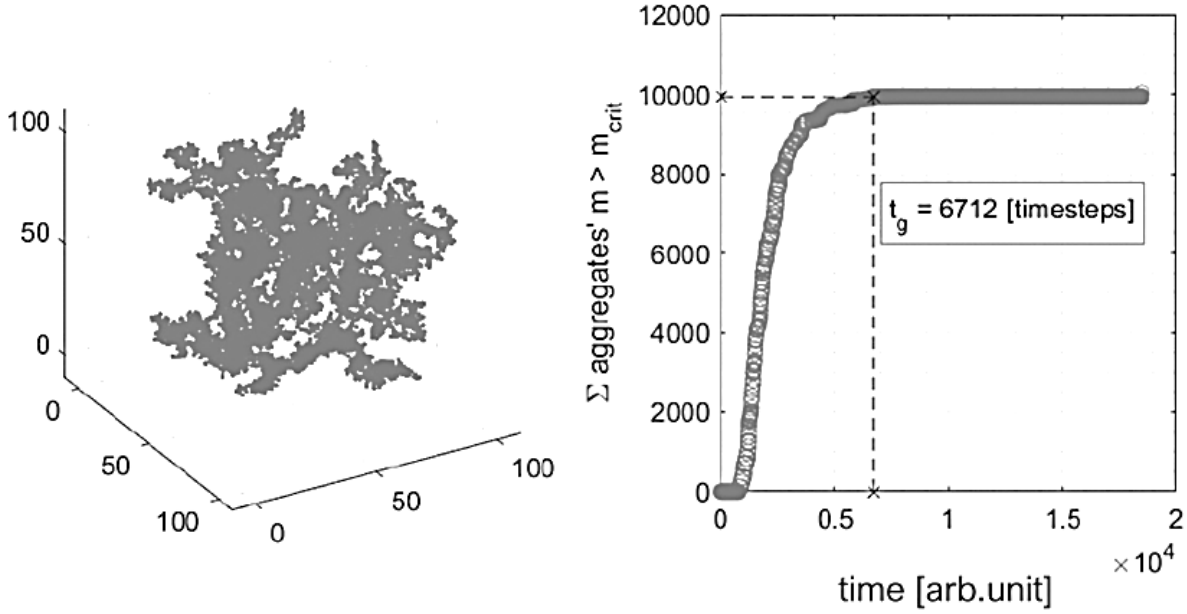

Fig. 61 Exemplary micro-structure and gelation kinetics of secondary particles in three dimensional system

The whole study-case in terms of porosity dependence on model parameters, morphology and kinetics curves are presented in Fig. 62 – Fig. 65. Similarly to the 2D system, the higher the probability or the concentration parameter value is, the faster gelation proceeds. As far as morphology of the aggregates is concerned, according to the theory and initial results (Fig. 47), as the system enters the reaction limited aggregation conditions, the aggregates become more dense, as it takes more steps for a particle to attach to an aggregate, thus it penetrates the aggregate "brunches" deeper before it gets attached. This effect is especially visible for very low probability values ($P = 0.001, 0.0001$), where the aggregates are clearly more dense comparing to DLCA conditions ($P = 1$) (Fig. 65).

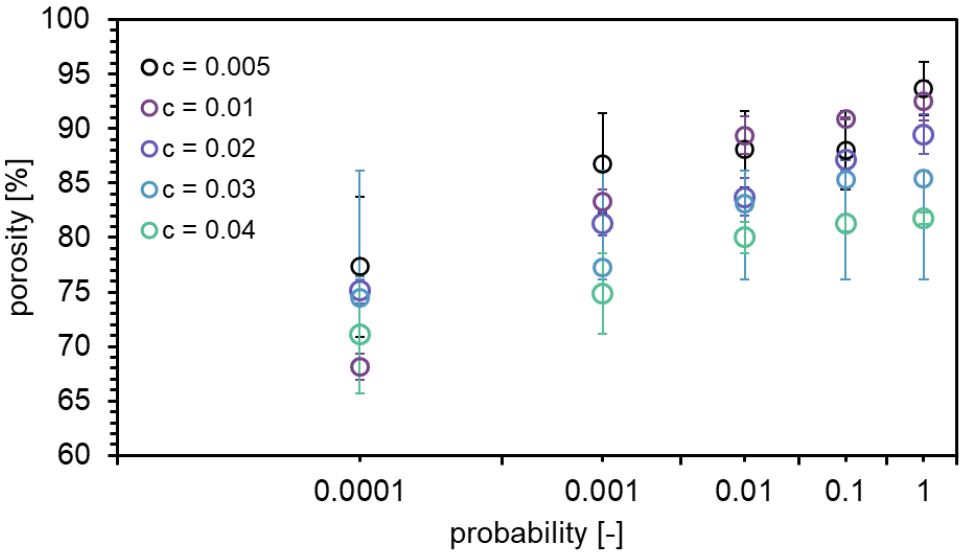

Fig. 62 Parameter sensitivity analysis on porosity

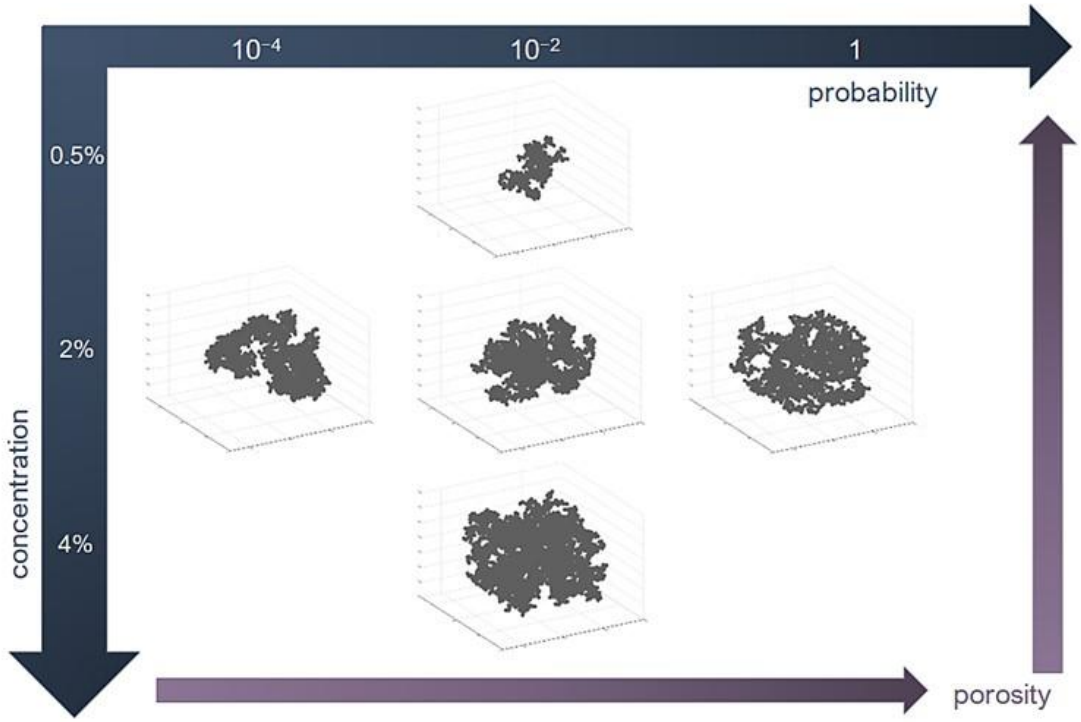

Fig. 63 Schematic representation of parameter sensitivity analysis on morphology&porosity [121]

The values of porosity are presented in Fig. 62. It can be easily noticed, that porosity of an obtained aggregate is increasing with probability value, thus as system approaches DLCA conditions. This dependence is valid for every tested concentration value, although the average porosity value fluctuates with standard deviation presented on the graph. If we look at the porosity values for pure DLCA regime ($P = 1$), it can be noticed that alcogel porosity increases as the concentration of secondary particles decreases. This observation is valid for

most of the tested probability values, however due to stochastic nature of the process in some cases the tendency is not as clear (e.g. $P = 0.0001$). However, the general tendency is increase of porosity with increase of reaction probability and decrease of SP concentration, which is schematically presented in Fig. 63.

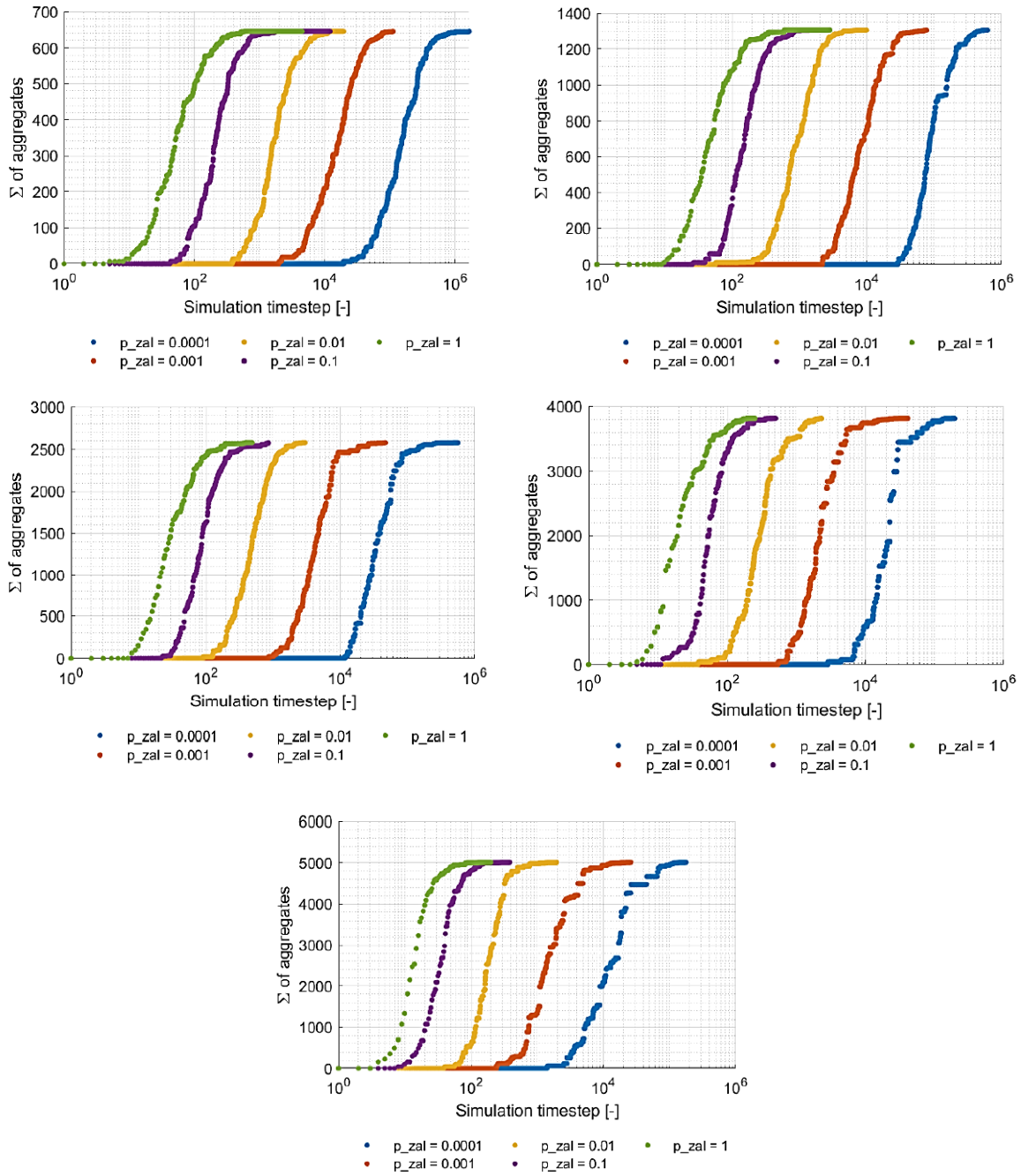

Fig. 64 Parameter sensitivity analysis on gelation kinetics

Fig. 65 Parameter sensitivity analysis on morphology

6.5.1 Experimental synthesis and model parameters estimation

The two constants in the linear form of the Arrhenius equation (activation energy E and the new constant A', dependant on the Arrhenius constant A, Eq. 6.5) were designated based on a series of time of gelation measurements (conducted by the tilting test tube method) for chosen values of temperature of gelation. The measurements were plotted, and a linear trend line was found with Excel software. The data points with error bars are plotted in Fig. 66. The corresponding kinetics curves, measured with UV-Vis spectrophotometer for the ambient temperature for gelation (as this was original temperature based on the synthesis recipe) are presented in Fig. 67. The influence of aqueous catalyst volume can be observed based on both graphs analysis (Fig. 66, Fig. 67), where it can be easily noticed how the increasing amount of catalyst solution causes the decrease of the time of gelation.

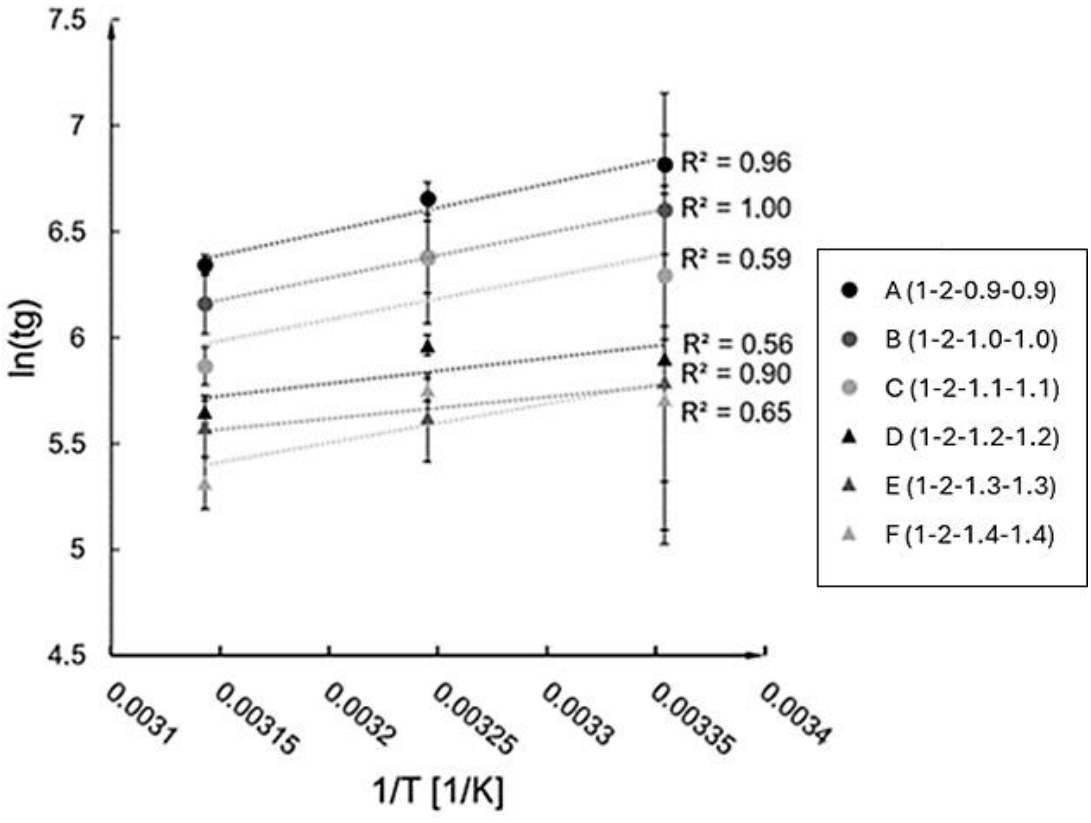

Fig. 66 Linearisation of Arrhenius equation for the studied samples A-F [121]

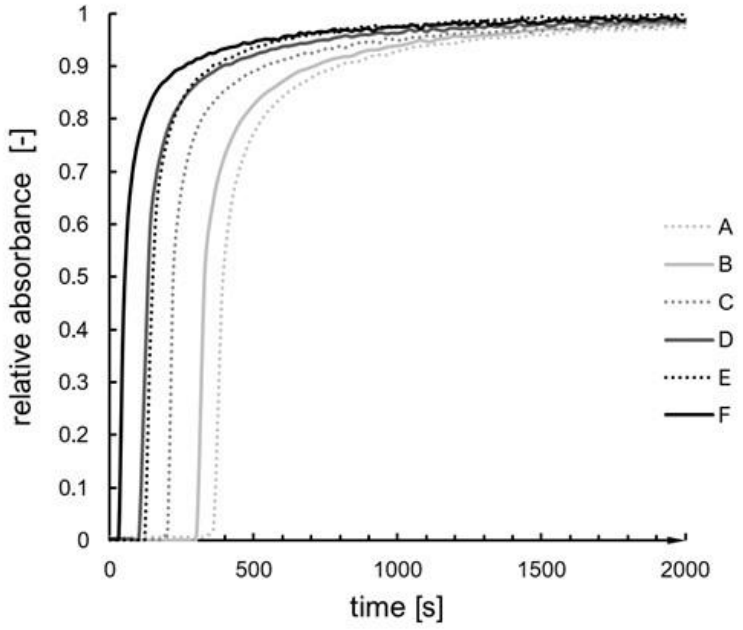

Fig. 67 Gelation kinetics of the experimental samples A-F [121]

Based on the slope and the intercept of the designated linear functions (Fig. 66), and the equation formula $\ln t_g = A_A + E/RT_g$ the values of probability rate and probability could be designated based on equations: $P = A_A \cdot \exp(-E/RT_g)$ and $P = [A_A \cdot \exp(-E/RT_g)]dt$ respectively (as it was explained in the subsection *6.4.3 Estimation of model parameters (3D approach)*). At this point of the study it is aimed to find only correlation between synthesis conditions and probability parameter value, so the factor of proportionality between constants A and A_A can be at this step or the studies omitted.

The value of the time step dt was established based on the conclusions from earlier studies of the two dimensional cellular automaton [122], where it was observed that for the same series of experimental synthesis the gel-point occurred approximately when the structure was gelled in 99%. Knowing the time of gelation for the experimental samples, and the number of timesteps for corresponding simulations, the values of the timestep could be calculated.

The concentration of the secondary particles was established based on the measured values of alcogel volume, dried sample mass and skeleton density, (according to Eq. 6.1) $c = m_s/\rho_s V_a\,[\%_{vol}]$. The values of the activation energy E and the constant A_A are presented in Fig. 68. The values of probability and probability rate are plotted on the graph presented in Fig. 69. All of the established parameters (c, P, and dt) for the studied synthesis $A - F$ are gathered in Table 11.

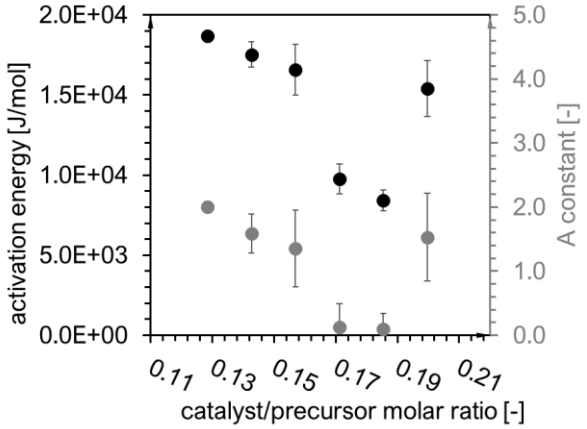

Fig. 68 The values of activation energy and A' constants [121]

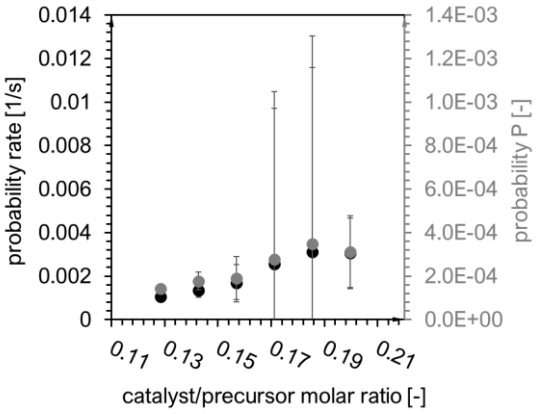

Fig. 69 The values of probability and probability rate [121]

Table 11 The analysed experimental samples, the established model parameters and time step

A (1-2-0.9-0.9)	**B (1-2-1-1)**	**C (1-2-1.1-1.1)**
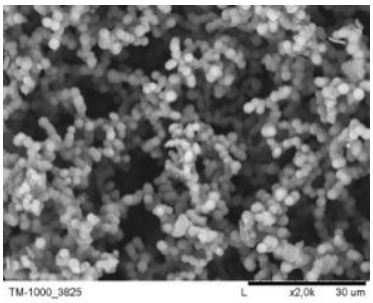	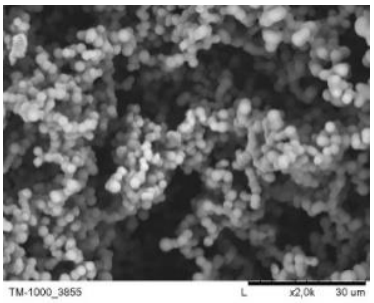	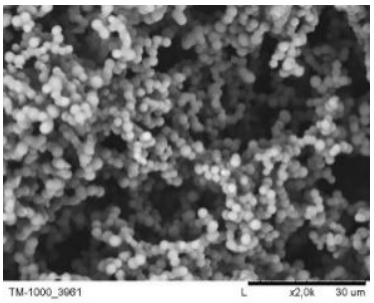
$c = 6.7\%$ $P = 1.4 \times 10^{-4}$ $dt = 1.34 \times 10^{-1}$	$c = 6.4\%$ $P = 1.8 \times 10^{-4}$ $dt = 1.31 \times 10^{-1}$	$c = 6.2\%$ $P = 1.9 \times 10^{-4}$ $dt = 1.14 \times 10^{-1}$
D (1-2-1.2-1.2)	**E (1-2-1.3-1.3)**	**F (1-2-1.4-1.4)**
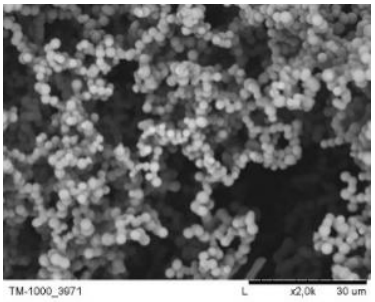	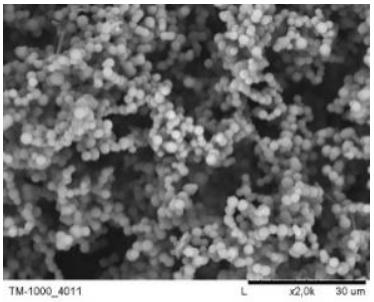	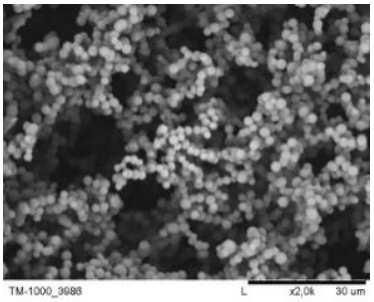
$c = 6\%$ $P = 2.8 \times 10^{-4}$ $dt = 1.08 \times 10^{-1}$	$c = 6.1\%$ $P = 3.5 \times 10^{-4}$ $dt = 1.12 \times 10^{-1}$	$c = 5.9\%$ $P = 3.1 \times 10^{-4}$ $dt = 1.02 \times 10^{-1}$

6.5.2 Model parameters verification

The final part of the research included in this section, was verification if the proposed in previous section correlation between model parameters and experimental conditions is actually accurate.

The data, both experimental and numerical, was thoroughly analysed. In order to be able to compare any two kinetics curve, it was decided to calculate the first derivative of mass on time sigmoid dependence $m(t)$, according to the methodology described in the previous chapter. As a result, the condensation rate dm/dt is obtained. The point of maximum condensation rate, $(dm/dt)_{max}$ was used to designate a tangent line to the kinetic curve $m(t)$, and the t_1 point which physical meaning is the end of first phase of gelation (the nucleation, as a first phase of structure formation). The time gelation, for this given case of syntheses ($A-F$) was stated to be equal to 99% reaction progress [122]. The time of the second phase is defined as a difference between time of gelation t_g and the time of the first phase t_1. All of the above considerations are schematically presented in Fig. 43 in the previous chapter.

There is no nucleation in the numerical cellular automaton system, as the simulation is initiated when the secondary particles are already formed. Thus, the only parameters in the proposed in the previous paragraph description, which are both suitable for experimental and numerical kinetics curves were:

- the maximum value of condensation rate, $(dm/dt)_{max}$ (red line in Fig. 43),
- the time of the second phase of condensation (explained schematically in Fig. 22 and Fig. 23, in Chapter 4).

Thus, it was decided to use the ratio of these 2 values as a comparative factor for experimental kinetics curves, and numerical kinetics curves, obtained for corresponding model parameters (Table 11). This procedure is an original, proposed assumption designed for verifying the proposed hypothesis in this chapter.

Fig. 70 presents the gelation rate designated for the experimental samples $A-$F over the whole time of UV-Vis spectrophotometric measurement. Fig. 71 contains designated values of the gelation phases: nucleation phase t_1, intensive mass growth (microscopic phase separation) t_2, and time of gelation t_g. All of the values were designated according to the method described above and presented schematically in Fig. 43 (the values of the gel point can be slightly different comparing to the ones obtained by the tilting test-tube method, as the condition of 99% formed structure for the determination of a gel-point was an approximation).

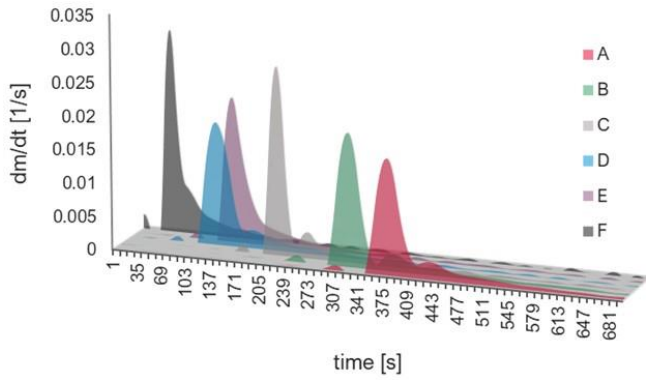

Fig. 70 Condensation rate of the experimental samples [121]

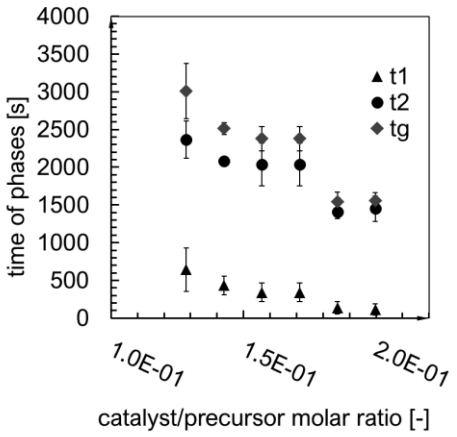

Fig. 71 Time of the t_1, t_2, t_{gel} of experimental samples [121]

Analogical graphs for the numerical results are presented below. Fig. 72 contains values of maximum condensation rate according to the study-case parameters: probability and SP concentration. Although the values fluctuate, the main trend is the increase of the maximum rate with the value of probability and SP concentration. However, the increase is not constant and steady even for the experimental case (Fig. 70). The two aspect matters: the value of the maximum condensation rate, but also how soon the peak appears, which can be clearly observed on Fig. 70. The graph presented in Fig. 73 contains the values of the numerical gel-point, depending on the tudy-case parameters (probability and SP concentration). The purple cross points ($c = 6.2\%$) are interpolated for the parameters corresponding to the experimental $A - F$ syntheses. This graph clearly shows how the experimental system is close to the reaction limited aggregation conditions.

The final comparison of the ratio of the kinetic parameters: the maximum value of condensation rate, $(dm/dt)_{max}$ and the time of the second phase of condensation (intensive mass growth or microscopic phase separation) t_2 is presented in Fig. 74. Despite many simplifications and assumptions, the experimental values are very similar to the ratios obtained for the cellular automaton simulations performed for experimental-based model parameters values. This comparison indicates potential for cellular automata to represent the complex experimental system.

Despite the clear focus of this thesis on the condensation kinetics, the last point of the CA research was to evaluate the applicability of the developed model for structure morphology and properties prediction. The experimental values of the alcogel porosity were

compared to the experimental values obtained for the numerical study-case in Fig. 75. It can be observed, that the values obtained based on CA simulations are significantly lower. However, the computational method of porosity designation could be adjusted with wider range of experimental samples and larger numerical RVE.

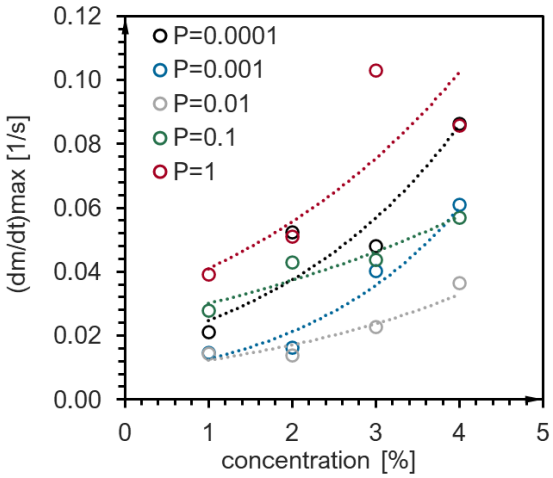

Fig. 72 Numerically obtained maximum condensation rates [121]

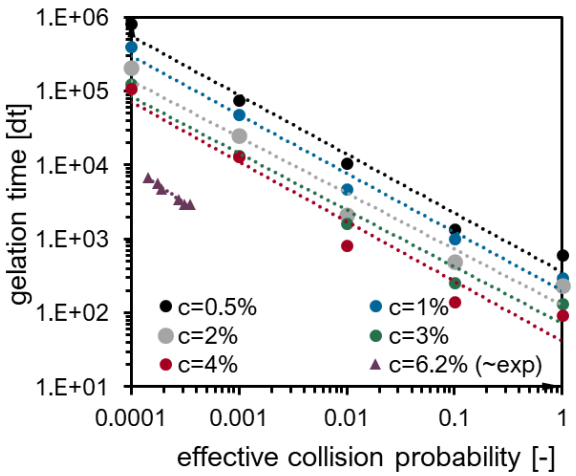

Fig. 73 Numerical gel-points values due to concentration of SP and reaction probability [121]

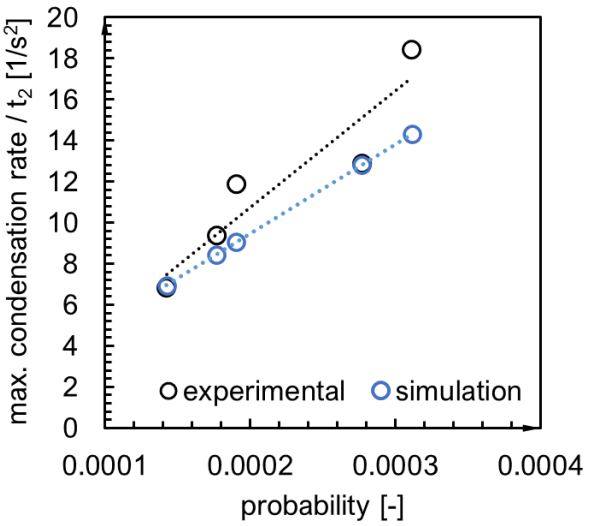

Fig. 74 The ratio of the maximum value of condensation rate, (dm⁄dt)max and the time of the second phase of condensation – numerical and experimental data [121]

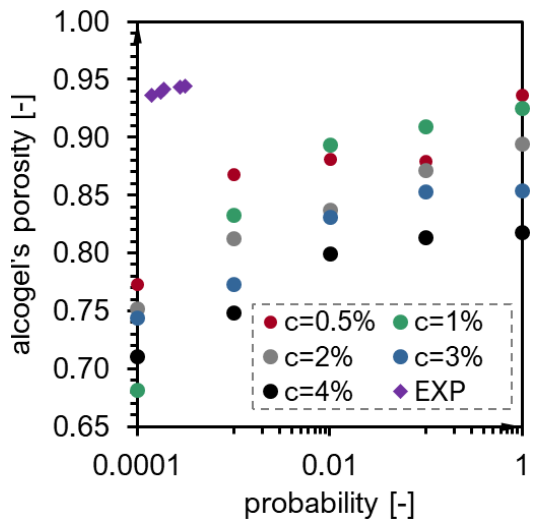

Fig. 75 Alcogel porosity – parameter sensitivity analysis [121]

6.6 CONCLUSIONS

This section's focus was on:

(i) developing numerical model, able to follow both kinetics of alcogel structure formation and the morphology of the final formed gel;

(ii) proposing a method of correlation between model parameters (concentration of secondary particles in the system and the probability of successful collision between adjacent particles);

(iii) validation of the proposed correlation between model parameters and experimental conditions, mostly on the level of reaction kinetics (this thesis main focus), but also briefly checking the applicability on the morphology and structural properties level.

The goals were accomplished successfully. Regarding the first goal (i), the model was successfully developed, first initial version for the simplified two dimensional system, which was later improved and transformed into the three dimensional, final approach. The cellular automaton allows to follow both kinetics and morphology of the obtained structures.

The study enabled by this numerical model led to many observations and conclusions on cellular automaton system. First of all, there is a significant dependence of the two model parameters and total time of structure formation. Both concentration of the particles in the system and probability of effective collision have a significant impact on the time of gelation. It is quite clear, that the more particles in the system are, the faster the structure will gel, as it is more likely for particles to approach each other. Similarly, the higher is the probability of effective collision (reaction probability) the fastest the structure formation progresses, leading to obtaining the final gelled structure. The probability parameter has also a significant impact on the aggregate morphology: the lower is the probability, the denser an aggregate appears to be. It is due to the fact that it takes more timestep for a particle to attach to aggregate branches, so it penetrates the structure deeper, before it finally connects to the aggregate. It results with more dense structure in RLCA regime (reaction limited cluster aggregation), and more dendritic and more porous aggregates obtained in DLCA conditions (diffusion limited cluster aggregation). It was also noticed that the gelation proceeds faster in the three-dimensional cellular automaton than the two-dimensional one, as in 3D system a given particle will have more neighbours, thus, for the same concentration value, the process will be accelerated.

Regarding the second goal (ii), a method of correlation between model parameters and experimental conditions was developed. It was proposed to use the Arrhenius equation, as it

correlates reaction rate (number of successful molecular collisions) with the number of molecular collisions with proper orientation and probability of successful conditions. This equation seemed to describe the simulated system well. The probability parameter established based on the linear form of this equation was due to measurement of gel-point for different temperatures of gelation. This procedure allowed to fit linear trend lines to the experimental data, and by the slope and intercept of the function establish the constants in the Arrhenius equation, thus, the probability of the reaction as CA model parameter. The obtained results of the activation energy were compared with the values available in the literature in Table 12. The obtained values seems to be with a sufficient agreement with literature data for other silica precursor, and also the first (to my best knowledge) reported data for the methyltrimethoxysilane as a precursor of silica aerogel synthesis.

Designation of the second model parameter – the concentration of secondary particles – was much easier, due to straight forward analytical method, which provided a simple formula, which correlates the concentration with three, easily measurable parameters: mass of a dry sample, the skeleton density and alcogel volume.

This method was verified (iii) mostly on the level of kinetics analysis. After a thorough analysis, it was stated, that the easiest way of quantitative analysis of the sigmoidal kinetics curve was by calculating the first derivative (structure formation rate) and based on the location of the maximum rate value, establishing time of the nucleation, phase separation and time of gelation. This procedure allowed to compare ratio of the only two parameters that could be designate for both experimental and numerical curves (as numerical system do not inhibit nucleation step, because the simulation is initiated at the stage of already formed secondary particles). The comparison of these ratios for the analysed experimental samples ($A - F$), and numerical simulations performed for parameters corresponding to experimental conditions (each SP concentration, reaction probability and timestep value were designated based on the proposed above method of correlation between numerical and experimental system) looks promising.

The model applicability is promising and cellular automata indicate a significant potential for representing the complex systems as sol gel system, or other type of particle-aggregation, stochastic systems. It should be emphasized that these results constitute one of the first effective attempts to link the parameters of the discrete particle-aggregation model (number of particles, probability of aggregation) with the parameters of the real system (gelation time, porosity of the obtained material). This opens the way to a quantitative description of gel formation using this group of models, which has so far been used only to describe the qualitative

behaviour of the system. However, the validation is not completely satisfactory and comprehensive. Definitely, more work on bridging gaps between experiments and numerical models is needed for creation of ultimate model able to precisely represent the complex system of organoalkoxysilane-based gels synthesis.

Table 12 Comparison of obtained activation energy results with the literature data

Source	*Precursor*	*E[kJ/mol]*	*Reference*
This thesis	methyltrimethoxysilane (MTMS)	2.6–37.6	[121]
A. Ponton et al. (2002)	tetramethoxysilane (TMOS)	37.1–38.2	[123]
C.J. Brinker and G.W. Scherer (1990)	general data for silica precursors	42–84	[1]

7. DISCUSSION & CONCLUSIONS

The aim of the thesis was to experimentally and numerically investigate the kinetics of sol-gel transition during the synthesis of organoalkoxysilane-based alcogels. This process is based on two chemical reactions (hydrolysis and condensation) and occurring parallelly imposition of physical phenomena, such as phase separation, Brownian motion, aggregation.

Nuclear magnetic resonance (NMR) was employed for methyltrimethoxysilane (MTMS) hydrolysis investigation NMR measurements indicate distinct decrease of the 0.12 ppm 1H-NMR signal during reaction, initially associated with methyl groups. Similar observation can be found in literature [103], identified as chemical cleavage, although the presented studies confirm that the decrease is acid catalyst concentration dependent. Exponential approximation of the hydrolysis kinetics curves provides initial reaction rates, indicating pre-equilibrium protonation as a step preceding hydrolysis of the organoalkoxysilane (MTMS). The identified mechanism is consistent with literature [14,124]. The conclusions made based on NMR studies were confirmed by measurements of time of gelation for the same sample prepared with different duration of hydrolysis. Any variation was within standard deviation. Due to this confirmation of the first hypothesis (*"The hydrolysis of methyltrimethoxysilane in acidic conditions is based on a protonation mechanism, and this step occurs very rapidly, thus, the time of conducting the hydrolysis reaction should not influence further stage of the sol gel synthesis: the gelation process and the gel-point value."*) it could have been assumed, that the reaction mixtures reaches maximum possible conversion ratio of hydrolysis reaction, thus, should not impact kinetics of the gelation, which was the main focus of this thesis.

An applicability of UV-Vis spectrophotometry for designation of condenstion kinetics for turbid samples was proven valid in the fourth chapter of the thesis. The direct dependence between absorbance and mass of condensing product was confirmed by comparison of kinetic data obtained by two methods: spectrophotometrically and by collecting produced deposited on a cellulose filter during reaction. The dependence of aerogel mass on time was obtained, providing additional quantitative understanding of the gelation process.

Two leading mechanisms of aerogel condensation kinetics were proposed: (i) reaction between hydrolysed precursor molecules - either free monomers or mers (within an oligomer or small aggregate). It is the leading mechanism in the initial phase of condensation – the nucleation. The second mechanism is characteristic and dominant in the second phase of condensation. It is based on addition of monomers to a bigger (already detectable) cluster (ii).

The reaction rate constant designated for the two developed methods of registering gelation kinetics (spectrophotometric and by filtration) has slightly different values, but the order of magnitude is correct, which at this stage of research was considered as satisfactory. The difference can be a result of relatively high errors for samples prepared for low concentrations of precursor, thus, with kinetics measured by the filtration method. This could explain any uncertainties. The both methods were proven valid, however the filtration method is more suitable for precipitants than monolithic samples, for which, spectrophotometric method offers more precise results. The kinetics of the condensation reaction were studied theoretically, and a simple dependence of mass of the condensing gel on time was proposed and verified experimentally.

Theoretical investigation lead to identification of three mechanisms of condensation, dominant for different phases of gelation (Fig. 22, Fig. 23, and Table 4):

i. the reaction between two or more precursor particles leading to the occurrence of a small alcogel cluster,
ii. the reaction between precursor particles and already formed cluster,
iii. merging of small clusters into a larger cluster.
iv. merging of big clusters

The mechanism (i) and (ii) was identified as a dominant mechanism during nucleation phase. The reaction between precursor particles and already formed cluster (iii) was identified as a leading mechanism during intensive mass growth (microscopic phase separation), and finally, the merging of big (detectable) clusters was identified as a main mechanism during cluster-cluster gelation (visible as a plateau on the kinetics curve).

Due to the phase separation investigation (Chapter 5) the areas of monolithic samples obtained due to different thermodynamic conditions were plotted in form of ternary plots, providing a comprehensive knowledge about correlation between initial chemical composition of the reaction mixture and final product's properties. The outline of binodal curve in a precursor-solvent-antisolvent ternary sol-gel system was established experimentally, based on the analysis of products' morphology, in respect to the division introduced in K. Nakanishi's work [49]. The transition from metastable to unstable conditions is observed while increasing the precursor/water ratio (for constant solvent contribution). Between these two regions there is a border, responding to the spinodal curve location, although it was not totally discovered.

A new method of quantitative comparison of condensation process registered spectrophotometrically was proposed, based on kinetics data interpolation and calculation of first derivative corresponding to the value of condensation rate. The condensation rate increases for lower concentration of solvent and lower values of precursor/water ratios. The collected experimental data provided comprehensive knowledge and understanding of relation between chemical composition of the reaction mixture and chosen structural properties of aerogels prepared based on this mixture. The studied parameters were: particle size distribution, polydispersity, porosity and kinetics of gelation.

The last section was focused on development and validation of a numerical model based on diffusion/reaction (cluster) aggregation, able to follow both kinetics of alcogel structure formation and the morphology of the final formed gel.

A novel method of correlation between model parameters (concentration of secondary particles in the system and the probability of successful collision between adjacent particles) was proposed, based on the Arrhenius equation. The validation of the proposed correlation on the level of reaction kinetics was successful, however the applicability of cellular automata and aggregation models for prediction of alcogels in general still leaves doubts. Especially since the target material is aerogel, the drying procedure and volume shrinkage have to be considered before any final evaluation of this model applicability, however at this stage the results are promising and indicate potential for rapid material development of aerogels. Definitely, more work on bridging gaps between experiments and numerical models is needed for creation of ultimate model able to precisely represent the complex system of organoalkoxysilane-based gels synthesis.

This thesis advanced the current state of the art with an in-depth and comprehensive understanding of phenomena occurring during the sol to gel transition of organoalkoxysilanes, the process very important, especially for aerogel community – devoted to incredible materials

that could target very specific and demanding applications, and solved challenges that modern industry is currently facing. Especially areas of avionic and aerospace engineering are highly interested in aerogel rapid development due to their low weight and incredible thermal insulation properties. The results of this thesis enable better prediction of (aero)gels properties, as well as kinetics of gelation, which is especially important while upscaling the synthesis process.

The four main hypotheses of the thesis were stated as follows:

1st hypothesis

The hydrolysis of methyltrimethoxysilane in acidic conditions is based on a protonation mechanism, and this step occurs very rapidly, thus, the time of conducting the hydrolysis reaction does not influence further stage of the sol gel synthesis: the gelation process and the gel-point value.

2nd hypothesis

The condensation reaction of a chosen organoalkoxysilane (methyltrimethoxysilane) can be followed through UV-Vis spectrophotometric measurements, and the mass of the formed gel formed due to polycondensation reaction progress is directly proportional to the time-dependant absorbance of a sample. The condensation rate is dependent on the precursor and the base catalyst concentrations. Basing on the condensation kinetics curves, the gelation can be divided into three phases, and the dominant, mechanisms of these phases can be identified

3rd hypothesis

With ternary diagrams based synthesis, one can establish the location of binode and spinode (the range of the metastable and unstable thermodynamic conditions on a ternary plot). Additionally, one can gain a comprehensive and extensive knowledge

on impact of (i) molecular structure of precursor, (ii) chemical composition of the reaction mixture on: condensation kinetics, thermodynamic conditions as well as the aerogel morphology.

4th hypothesis

A cellular automaton can be applied as a simplified representation of the gelation process, in particular for the aggregation of secondary organoalkoxysiloxane-based particles. The model parameters can be correlated with experimental synthesis conditions with the Arrhenius equation.

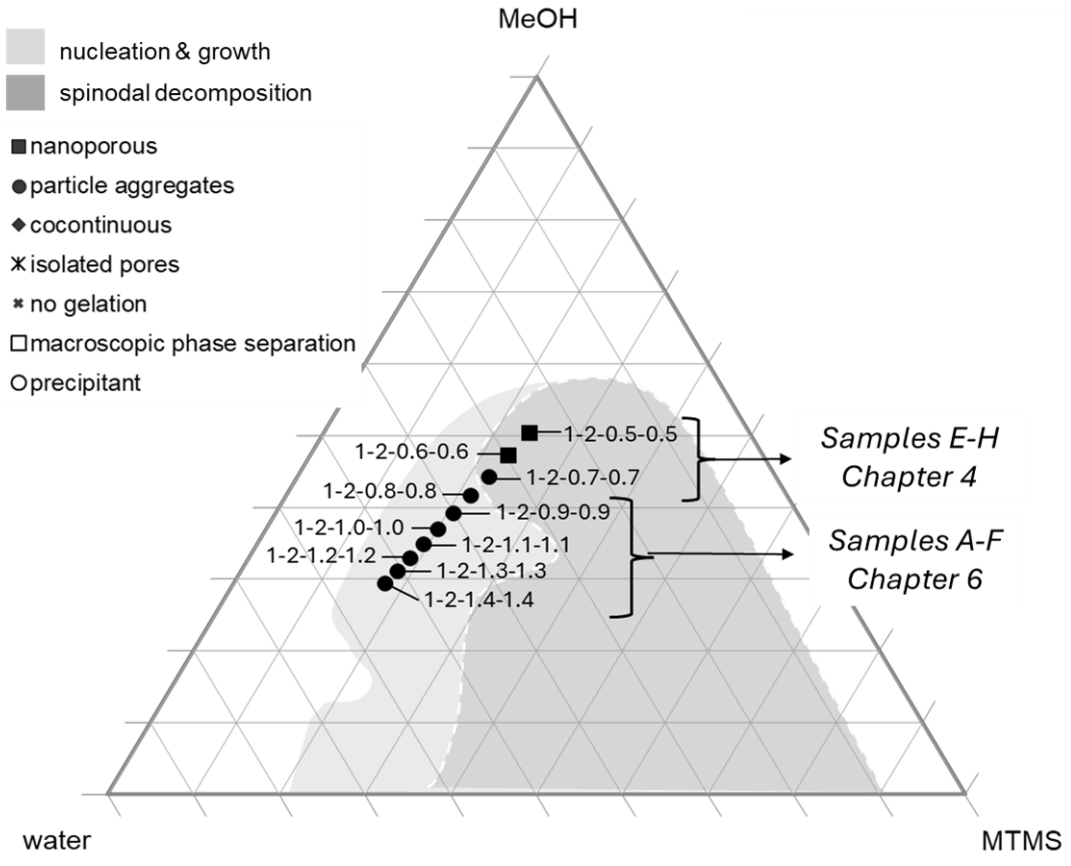

Fig. 76 The experimental samples selected for validation of both developed models (analytical in Chapter 4 and CA-based in Chapter 6)

The four hypothesis were to an advanced extent verified. However certain questions remain, namely, how to accurately describe model imposition of liquid-liquid phase separation

and polymerization induced separation and how to increase the accuracy of the cellular automaton for SP aggregation representation.

Table 13 Summary of experimental samples used for model validation

Volume composition [ml]				*Mass fractions [-]*					*Denotation*	
MTMS :	*MeOH:*	*aq. acid solution*	*aq. base solution*	*Xp*	*Xs*	*Xw*	*Phase separation*	*Morphology*	*Chapter 4*	*Chapter 6*
1	2	0.5	0.5	0.24	0.50	0.26	SD	cocontinuous	E	-
1	2	0.6	0.6	0.23	0.47	0.30	SD	cocontinuous particle	F	-
1	2	0.7	0.7	0.22	0.44	0.33	N&G	aggregates particle	G	-
1	2	0.8	0.8	0.22	0.42	0.37	N&G	aggregates particle	H	
1	2	0.9	0.9	0.21	0.39	0.40	N&G	aggregates particle	-	A
1	2	1.0	1.0	0.20	0.37	0.43	N&G	aggregates particle	-	B
1	2	1.1	1.1	0.19	0.35	0.46	N&G	aggregates particle		C
1	2	1.2	1.2	0.19	0.33	0.48	N&G	aggregates particle	-	D
1	2	1.3	1.3	0.18	0.31	0.51	N&G	aggregates particle	-	E
1	2	1.4	1.4	0.18	0.29	0.53	N&G	aggregates		F

It is also important that the experimental samples chosen to validate the analytical model (samples $E - G$ in Chapter 4) and CA model (samples $A - F$ in Chapter 6) represent a full transition from spinodal decomposition to nucleation and growth mechanism of microscopic phase separation. The precise selection is plotted on the ternary graph (Fig. 76), and the recipes are included in Table 13. Originally the sample selection can be found in Chapter 4 (Table 3) and in Chapter 6 (Table 11). The fact that samples $E - G$ cross both N&G and SD regions proves the universal character of the developed analytical description. However it has to be mentioned that sample 1-2-0.7-0.7 (sample G from Chapter 4) is located at the approximated border of the two regions (on the spinodal curve), however it's morphology is particle aggregates (N&G). This is caused to the stochastic nature of the process and very specific location of the sample on the ternary plot. With limited number of experiments performed within Chapter 5, only an approximate location of the spinode could be established which explains this inaccuracy.

The main novelty of this thesis lies in validation of the aggregation model, which to my knowledge was not reported in literature before. Additionally, dominant mechanisms occurring through condensation phases were identified, providing better understanding of the organoalkoxysilane-based system kinetics and thermodynamic conditions.

The presented work is complementary to the one of the current directions of chemical engineering – the synthesis of novel, porous materials that tailored for very specific applications, such as silica aerogels. This research proposes and validates the thorough description of organoalkoxysilanes gelation. The determination of kinetic parameters of hydrolysis and gelation is an important step towards upscaling and sustainable synthesis of aerogels.

8. ACADEMIC ACHIEVEMENTS

8.1. LIST OF SCIENTIFIC PUBLICATIONS

Nr	*Publication*	*IF **	*Polish Ministry of Science and Higher Education points **	*Citations***
1	Borzęcka, N.H.; Kozłowska, I.; Gac, J.M.; Bojarska, M. *Anti-Fouling Properties of Poly(Acrylic Acid) Grafted Ultrafiltration Membranes – Experimental and Theoretical Study*. Appl Surf Sci 2019, doi:10.1016/j.apsusc.2019.144658.	6.7	140	9
2	Borzęcka, N.H.; Nowak, B.; Gac, J.M.; Głaz, T.; Bojarska, M. *Kinetics of MTMS-Based Aerogel Formation by the Sol-Gel Method - Experimental Results and Theoretical Description*. J	3.5	70	12

	Non Cryst Solids 2020, 547, 120310, doi:10.1016/j.jnoncrysol.2020.120310.			
3	Borzęcka, N.H.; Nowak, B.; Pakuła, R.; Przewodzki, R.; Gac, J.M. *Cellular Automata Modeling of Silica Aerogel Condensation Kinetics*. Gels 2021, 7, doi:10.3390/gels7020050.	4.6	20	6
4	Borzęcka, N.H.; Nowak, B.; Pakuła, R.; Przewodzki, R.; Gac, J.M. *Diffusion/Reaction Limited Aggregation Approach for Microstructure Evolution and Condensation Kinetics during Synthesis of Silica-Based Alcogels*. Int J Mol Sci 2023, 24, doi:10.3390/ijms24031999.	5.6	140	2

Citations: 29

H-index: 3

** Impact Factor and Polish Ministry of Science and Higher Education points values in 2024*

*** Data from Scopus, 07.06.2024 [3]*

8.2 LIST OF CONFERENCES

Affiliated to Warsaw University of Technology (2018-2023):

1. 8th European Young Engineers Conference (Warsaw, Poland, 8-10.04.2019), "Modelling dynamics of polymer chains grafted to a surface of a separative membrane", Nina Borzęcka*, Jakub Gac, (oral presentation, presenting author)

2. 23rd Polish Conference of Chemical and Process Engineering (Jachranka, Poland, 2-5.06.2019), "Modelling dynamics of poly(acrylic acid) chains grafted to a surface of polypropylene membrane", Nina Borzęcka*, Jakub Gac, (oral presentation, presenting author)

3. 5th International Seminar On Aerogels (online, 16-18.09.2020), “Elaboration of cellular automata-based numerical model reflecting condensation kinetics of MTMS-based aerogels”, Nina Borzęcka*, Bartosz Nowak, Rafał Pakuła, Jakub Gac (poster presentation, presenting author)

4. 9th European Young Engineers Conference (online, 4-6.04.2022), “Cellular automata modeling of silica aerogel condensation kinetics", Nina H. Borzęcka*, Bartosz Nowak, Rafał Pakuła, Robert Przewodzki, Jakub M. Gac (oral presentation, presenting author)

5. 9th European Young Engineers Conference (online, 4-6.04.2022), "Phase separation in MTMS-based sol-gel system and secondary partlices’ dispersity ", Aleksandra M. Pisarek*, Nina H. Borzęcka, Bartosz Nowak, Jakub M. Gac (oral presentation, co-author)

6. Sol-Gel (Lyon, France, 24-29.07.2022), “Kinetics and mechanism of methyltrimethoxysilane hydrolysis” , Nina H. Borzęcka*, József Kalmár, Attila Forgács, Bartosz Nowak, Robert Przewodzki, Jakub M. Gac, (poster presentation, presenting author)

7. Sol-Gel (Lyon, France, 24-29.07.2022), “Influence of organic group on structure and properties of organotrialkoxysilane-based aerogel”, Bartosz Nowak*, Bartosz Babiarczuk, Nina Borzęcka, Jakub Gac, (poster presentation, co-author)

8. Sol-Gel (Lyon, France, 24-29.07.2022), “Cellular automata coupled with lattice boltzmann model for modeling of silica aerogel formation and structure”, Jakub M. Gac*, Nina H. Borzęcka, Bartosz Nowak (poster presentation, co-author)

9. 6th International Seminar On Aerogels (Hamburg, Germany, 28-30.09.2022), “MTMS and VTMS-based aerogel synthesis - phase separation and condensation kinetics”, Nina Borzęcka*, Bartosz Nowak, Aleksandra Pisarek, Jakub Gac (poster presentation, presenting author)

10. 6th International Seminar On Aerogels (Hamburg, Germany, 28-30.09.2022), “Structure vs mechanical properties of MTMS-based aerogel”, Bartosz Nowak*, Bartosz Babiarczuk, Nina Borzęcka, Daniel Lewandowski, Jakub Gac (poster presentation, co-author)

Affiliated to German Aerospace Center (since 2023):

11. The 1st International Seminar on Modelling, Simulation and Machine Learning for the Rapid Development of Porous Materials (Cologne, Germany, 10-12.05.2023), “A new type of hybrid aggregation model and the application towards silica (aero)gels”, Nina Borzęcka*, Prakul Pandit*, Ameya Rege (oral presentation, tandem speech, one of the presenting authors)

12. 2nd International Conference on Aerogel Inspired Materials (San Sebastian, Spain, 27-29.09.2023), “How accurately can silica aerogels be computationally modelled?” Nina Borzęcka*, Prakul Pandit, Ameya Rege (oral presentation, presenting author)

13. DLR Material Colloquium (Cologne, Germany, 05.12.2023), “Digital material twins for silica aerogels“, Nina Borzęcka*, Prakul Pandit, Ameya Rege (oral presentation, presenting author)

14. The 2nd International Seminar on Modelling, Simulation and Machine Learning for the Rapid Development of Porous Materials (Madrid, Spain, 4-6.03.2024), “Insights into modelling the gelation process in cellulose aerogels”, Jannik Jarms, Nina Borzęcka*, Ameya Rege (oral presentation, presenting author)

15. The 2nd International Seminar on Modelling, Simulation and Machine Learning for the Rapid Development of Porous Materials (Madrid, Spain, 4-6.03.2024), “Towards Sustainable Material Development: Computational modelling of (Aero)-gels”, Prakul Pandit*, Nina Borzęcka, Ameya Rege (oral presentation, co-author)

16. DPG Spring Meeting (Berling, Germany, 17-22.03.2024), “Insights into Modelling Cellulose Aerogels: A Computational Approach”, Jannik Jarms, Nina Borzęcka*, Ameya Rege (oral presentation, presenting author)

8.3 INTERNATIONAL INTERNSHIPS & VISITS

Affiliated to Warsaw University of Technology (2018-2023):

- Short term scientific mission, COST Action CA18125 at University of Debrecen (Debrecen, Hungary, 1-31.III.2021), “Investigation of hydrolysis and condensation reactions as the initial steps of the mechanism of MTMS based aerogel synthesis”. Supervised by dr Attila Forgacs and professor József Kalmar,

Affiliated to German Aerospace Center (since 2023):

- Scientific visit at Nagoya university and Kyoto University (Nagoya, Kyoto, Japan 21.01.2024-04.02.2024). Supervised by professor Kazuki Nakanishi, professor George Hasegawa and professor Kazuyoshi Kanamori.

8.4 INTERNATIONAL WORKSHOPS

Affiliated to Warsaw University of Technology (2018-2023):

- 7th International Summer School on Aerogels (German Aerospace Center, Cologne, Germany, 20-23.09.2022)

Affiliated to German Aerospace Center (since 2023):

- 6th Spring School Lattice Boltzmann Methods with OpenLB Software Lab (University of Greenwich, London, England, United Kingdom 5-9.06.2023)

8.5 REWARDS AND SCHOLARSHIPS

- Dean’s award for scientific and organisation achievements 2019/2020 (“*Nagroda Dziekana za osiągnięcia naukowe i organizacyjne*”);

- Dean's distinction for scientific and organisation achievements 2020/2021 ("*Wyróżnienie Dziekana za osiągnięcia naukowe i organizacyjne*");
- Scholarship 2020/2021 ("*Stypendium projakościowe*");
- Rector's scholarship 2020/2021 ("*Stypendium Rektora*");
- Rector's scholarship 2020/2021 ("*Stypendium Rektora*")

8.6 OTHER ACTIVITIES

- Collaboration with Scientific Club of Chemical and Process Engineering, co-organization of 8th European Young Engineers Conference;
- Editorship of 8th European Young Engineers Conference Monograph;
- Participation in The Faculty PhD Students Council 2018-2020 ("*Wydziałowa Rada Doktorantów*");
- Participation in The PhD Students Council 2018/2019 ("*Rada Doktorantów Politechniki Warszawskiej*");
- "*Przedstawiciel Doktorantów WIChiP w komisji ds. dydaktycznych*." 2021/2022.

9. LIST OF TABLES

10. LIST OF FIGURES

11. REFERENCES

1. C.J. Brinker; G. W. Scherer *Sol-Gel Science The physics and chemistry of sol-Gel_processing* **1990**.

2. Edition, S. *The Sol-to-Gel Transition*; ISBN 9783030200299.

3. Elsevier B.V. Scopus Preview - Scopus - Welcome to Scopus. *Scopus Preview* 2020.

4. Everett, D.H. Manual of Symbols and Terminology for Physicochemical Quantities and Units, Appendix II: Definitions, Terminology and Symbols in Colloid and Surface Chemistry. In Proceedings of the Pure and Applied Chemistry; 2019.

5. Alemán, J.; Chadwick, A. V.; He, J.; Hess, M.; Horie, K.; Jones, R.G.; Kratochvíl, P.; Meisel, I.; Mita, I.; Moad, G.; et al. Definitions of Terms Relating to the Structure and Processing of Sols, Gels, Networks, and Inorganic-Organic Hybrid Materials (IUPAC Recommendations 2007). *Pure and Applied Chemistry* **2007**, *79*, doi:10.1351/pac200779101801.

6. Roy, R. Ceramics by the Solution-Sol-Gel Route. *Science (1979)* **1987**, *238*, doi:10.1126/science.238.4834.1664.

7. Deshmukh, K.; Kovářík, T.; Křenek, T.; Docheva, D.; Stich, T.; Pola, J. Recent Advances and Future Perspectives of Sol-Gel Derived Porous Bioactive Glasses: A Review. *RSC Adv* 2020, *10*.

8. Brinker, C.J.; Hurd, A.J.; Schunk, P.R.; Frye, G.C.; Ashley, C.S. Review of Sol-Gel Thin Film Formation. *J Non Cryst Solids* 1992, *147–148*.

9. Minami, T. Advanced Sol-Gel Coatings for Practical Applications. *J Solgel Sci Technol* **2013**, *65*, doi:10.1007/s10971-011-2572-y.

10. Kloskowski, A.; Pilarczyk, M.; Chrzanowski, W.; Namieśnik, J. Sol-Gel Technique-a Versatile Tool for Adsorbent Preparation. *Crit Rev Anal Chem* **2010**, *40*, doi:10.1080/10408347.2010.490486.

11. Jelle, B.P.; Baetens, R.; Gustavsen, A. Aerogel Insulation for Building Applications. In *The Sol-Gel Handbook*; 2015; Vol. 3–3.

12. Innocenzi, P. Measuring the Sol-to-Gel Transition. In; 2016.

13. Aegerter, M.; Leventis, N.; Koebel, M. *Aerogels Handbook (Advances in Sol-Gel Derived Materials and Technologies)*; 2011; ISBN 9781441974778.

14. Issa, A.A.; Luyt, A.S. Kinetics of Alkoxysilanes and Organoalkoxysilanes Polymerization: A Review. *Polymers (Basel)* **2019**, *11*, doi:10.3390/polym11030537.

15. Ratke, L.; Gurikov, P. *The Chemistry and Physics of Aerogels*; 2021;

16. Hüsing, N.; Schubert, U. Aerogels—Airy Materials: Chemistry, Structure, and Properties. *Angewandte Chemie International Edition* **1998**, *37*, 22–45, doi:10.1002/1521-3773(19980202)37:1/2<22::aid-anie22>3.3.co;2-9.

17. Zerda, T.W.; Artaki, I.; Jonas, J. Study of Polymerization Processes in Acid and Base Catalyzed Silica Sol-Gels. *J Non Cryst Solids* **1986**, *81*, doi:10.1016/0022-3093(86)90503-X.

18. Shibayama, M. Gel Formation Analyses by Dynamic Light Scattering. **2002**.

19. Hüsing, N.; Schubert, U. Aerogels—Airy Materials: Chemistry, Structure, and Properties. *Angewandte Chemie International Edition* **1998**, *37*, doi:10.1002/1521-3773(19980202)37:1/2<22::aid-anie22>3.3.co;2-9.

20. Liu, Y. Polymerization-Induced Phase Separation and Resulting Thermomechanical Properties of Thermosetting/Reactive Nonlinear Polymer Blends: A Review. *J Appl Polym Sci* 2013, *127*.

21. Kaji, H.; Nakanishi, K.; Soga, N. Polymerization-Induced Phase Separation in Silica Sol-Gel Systems Containing Formamide. *J Solgel Sci Technol* **1993**, *1*, 35–46, doi:10.1007/BF00486427.

22. Flory, P.J. Thermodynamics of High Polymer Solutions. *J Chem Phys* 1941, *9*.

23. Favvas, E.P.; Mitropoulos, A.C. What Is Spinodal Decomposition? *Journal of Engineering Science and Technology Review* **2008**, *1*, doi:10.25103/jestr.011.05.

24. Wang, F.; Altschuh, P.; Ratke, L.; Zhang, H.; Selzer, M.; Nestler, B. Progress Report on Phase Separation in Polymer Solutions. *Advanced Materials* **2019**, *31*, doi:10.1002/adma.201806733.

25. Shimizu, R.; Tanaka, H. A Novel Coarsening Mechanism of Droplets in Immiscible Fluid Mixtures. *Nat Commun* **2015**, *6*, doi:10.1038/ncomms8407.

26. Tozar, A.; Tasbozan, O.; Kurt, A. Analytical Solutions of Cahn-Hillard Phase-Field Model for Spinodal Decomposition of a Binary System. *EPL* **2020**, *130*, doi:10.1209/0295-5075/130/24001.

27. Cahn, J.W.; Hilliard, J.E. Free Energy of a Nonuniform System. I. Interfacial Free Energy. *J Chem Phys* **1958**, *28*, doi:10.1063/1.1744102.

28. Shao, J.Y.; Shu, C.; Huang, H.B.; Chew, Y.T. Free-Energy-Based Lattice Boltzmann Model for the Simulation of Multiphase Flows with Density Contrast. *Phys Rev E Stat Nonlin Soft Matter Phys* **2014**, *89*, doi:10.1103/PhysRevE.89.033309.

29. Thanh, N.T.K.; Maclean, N.; Mahiddine, S. Mechanisms of Nucleation and Growth of Nanoparticles in Solution. *Chem Rev* 2014, *114*.

30. Green, D.L.; Lin, J.S.; Lam, Y.F.; Hu, M.Z.C.; Schaefer, D.W.; Harris, M.T. Size, Volume Fraction, and Nucleation of Stober Silica Nanoparticles. *J Colloid Interface Sci* **2003**, *266*, doi:10.1016/S0021-9797(03)00610-6.

31. Fouilloux, S.; Taché, O.; Spalla, O.; Thill, A. Nucleation of Silica Nanoparticles Measured in Situ during Controlled Supersaturation Increase. Restructuring toward a Monodisperse Nonspherical Shape. *Langmuir* **2011**, *27*, doi:10.1021/la2013842.

32. Carcouët, C.C.M.C.; Van De Put, M.W.P.; Mezari, B.; Magusin, P.C.M.M.; Laven, J.; Bomans, P.H.H.; Friedrich, H.; Esteves, A.C.C.; Sommerdijk, N.A.J.M.; Van Benthem,

R.A.T.M.; et al. Nucleation and Growth of Monodisperse Silica Nanoparticles. *Nano Lett* **2014**, *14*, doi:10.1021/nl404550d.

33. Forgács, A.; Moldován, K.; Herman, P.; Baranyai, E.; Fábián, I.; Lente, G.; Kalmár, J. Kinetic Model for Hydrolytic Nucleation and Growth of TiO2 Nanoparticles. *Journal of Physical Chemistry C* **2018**, *122*, 19161–19170, doi:10.1021/acs.jpcc.8b04227.

34. Ostwald, W. On the Assumed Isomerism of Red and Yellow Mercury Oxide and the Surface-Tension of Solid Bodies. *Zeitschrift Fur Physikalische Chemie--Stochiometrie Und Verwandtschaftslehre* **1900**, *34*.

35. Kahlweit, M. Ostwald Ripening of Precipitates. *Adv Colloid Interface Sci* **1975**, *5*, doi:10.1016/0001-8686(75)85001-9.

36. Lifshitz, I.M.; Slyozov, V. V. The Kinetics of Precipitation from Supersaturated Solid Solutions. *Journal of Physics and Chemistry of Solids* **1961**, *19*, doi:10.1016/0022-3697(61)90054-3.

37. Lee, W.R.; Kim, M.G.; Choi, J.R.; Park, J. Il; Ko, S.J.; Oh, S.J.; Cheon, J. Redox-Transmetalation Process as a Generalized Synthetic Strategy for Core-Shell Magnetic Nanoparticles. *J Am Chem Soc* **2005**, *127*, doi:10.1021/ja053659j.

38. Lamer, V.K.; Dinegar, R.H. Theory, Production and Mechanism of Formation of Monodispersed Hydrosols. *J Am Chem Soc* **1950**, *72*, doi:10.1021/ja01167a001.

39. Whitehead, C.B.; Özkar, S.; Finke, R.G. LaMer's 1950 Model of Particle Formation: A Review and Critical Analysis of Its Classical Nucleation and Fluctuation Theory Basis, of Competing Models and Mechanisms for Phase-Changes and Particle Formation, and Then of Its Application to Silver Halide, Semiconductor, Metal, and Metal-Oxide Nanoparticles. *Mater Adv* 2021, *2*.

40. Whitehead, C.B.; Özkar, S.; Finke, R.G. LaMer's 1950 Model for Particle Formation of Instantaneous Nucleation and Diffusion-Controlled Growth: A Historical Look at the Model's Origins, Assumptions, Equations, and Underlying Sulfur Sol Formation Kinetics Data. *Chemistry of Materials* 2019, *31*.

41. Watzky, M.A.; Finke, R.G. Nanocluster Size-Control and "Magic Number" Investigations. Experimental Tests of the "Living-Metal Polymer" Concept and of Mechanism-Based Size-Control Predictions Leading to the Syntheses of Iridium (0)

Nanoclusters Centering about Four Sequential Magic Numbers. *Chemistry of Materials* **1997**, *9*, doi:10.1021/cm9704387.

42. Besson, C.; Finney, E.E.; Finke, R.G. A Mechanism for Transition-Metal Nanoparticle Self-Assembly. *J Am Chem Soc* **2005**, *127*, doi:10.1021/ja0504439.

43. Amirjani, A.; Haghshenas, D.F. Modified Finke-Watzky Mechanisms for the Two-Step Nucleation and Growth of Silver Nanoparticles. *Nanotechnology* **2018**, *29*, doi:10.1088/1361-6528/aae3dd.

44. Pestovsky, Y.S.; Srichana, T. Formation of Aggregate-Free Gold Nanoparticles in the Cyclodextrin-Tetrachloroaurate System Follows Finke–Watzky Kinetics. *Nanomaterials* **2022**, *12*, doi:10.3390/nano12040583.

45. Martin, J.D. Particle Size Is a Primary Determinant for Sigmoidal Kinetics of Nanoparticle Formation: A "Disproof" of the Finke-Watzky (F-W) Nanoparticle Nucleation and Growth Mechanism. *Chemistry of Materials* 2020, *32*.

46. Li, D.; Nielsen, M.H.; Lee, J.R.I.; Frandsen, C.; Banfield, J.F.; De Yoreo, J.J. Direction-Specific Interactions Control Crystal Growth by Oriented Attachment. *Science (1979)* **2012**, *336*, doi:10.1126/science.1219643.

47. Krüger, T. *The Lattice Method Boltzmann Principles and Practice*; 2004;

48. Zheng, L.; Zheng, S.; Zhai, Q. Lattice Boltzmann Equation Method for the Cahn-Hilliard Equation. *Phys Rev E Stat Nonlin Soft Matter Phys* **2015**, *91*, doi:10.1103/PhysRevE.91.013309.

49. Nakanishi, K.; Kanamori, K. Organic-Inorganic Hybrid Poly(Silsesquioxane) Monoliths with Controlled Macro- and Mesopores. *J Mater Chem* **2005**, *15*, 3776–3786, doi:10.1039/b508415f.

50. Itagaki, A.; Nakanishi, K.; Hirao, K. Phase Separation in Sol-Gel System Containing Mixture of 3- and 4-Functional Alkoxysilanes. *J Solgel Sci Technol* **2003**, *26*, 153–156, doi:10.1023/A:1020770209234.

51. Ivanov, P. V.; Mazhorova, N.G. Comparative Analysis of Phase Diagrams of Organochlorosilane/Organoalkoxysilane—Solvent—Water Systems. *Russian Chemical Bulletin* **2020**, *69*, doi:10.1007/s11172-020-2867-7.

52. Uricanu, V.; Donescu, D.; Banu, A.G.; Serban, S.; Olteanu, M.; Dudau, M. Organic-Inorganic Hybrids Made from Polymerizable Precursors. *Mater Chem Phys* **2004**, *85*, doi:10.1016/j.matchemphys.2003.12.024.

53. *Aerogels Handbook*; 2011;

54. *The IUPAC Compendium of Chemical Terminology*; 2019;

55. Buchtová, N.; Budtova, T. Cellulose Aero-, Cryo- and Xerogels: Towards Understanding of Morphology Control. *Cellulose* **2016**, *23*, doi:10.1007/s10570-016-0960-8.

56. Job, N.; Théry, A.; Pirard, R.; Marien, J.; Kocon, L.; Rouzaud, J.N.; Béguin, F.; Pirard, J.P. Carbon Aerogels, Cryogels and Xerogels: Influence of the Drying Method on the Textural Properties of Porous Carbon Materials. *Carbon N Y* **2005**, *43*, doi:10.1016/j.carbon.2005.04.031.

57. Rodríguez-Dorado, R.; López-Iglesias, C.; García-González, C.A.; Auriemma, G.; Aquino, R.P.; Del Gaudio, P. Design of Aerogels, Cryogels and Xerogels of Alginate: Effect of Molecular Weight, Gelation Conditions and Drying Method on Particles' Micromeritics. *Molecules* **2019**, *24*, doi:10.3390/molecules24061049.

58. Groult, S.; Buwalda, S.; Budtova, T. Pectin Hydrogels, Aerogels, Cryogels and Xerogels: Influence of Drying on Structural and Release Properties. *Eur Polym J* **2021**, *149*, doi:10.1016/j.eurpolymj.2021.110386.

59. García-González, C.A.; Budtova, T.; Durães, L.; Erkey, C.; Del Gaudio, P.; Gurikov, P.; Koebel, M.; Liebner, F.; Neagu, M.; Smirnova, I. An Opinion Paper on Aerogels for Biomedical and Environmental Applications. *Molecules* 2019, *24*.

60. Schwan, M.; Rößler, M.; Milow, B.; Ratke, L. From Fragile to Resilient Insulation: Synthesis and Characterization of Aramid-Honeycomb Reinforced Silica Aerogel Composite Materials. *Gels* **2016**, *2*, doi:10.3390/gels2010001.

61. Afroze, J.D.; Tong, L.; Abden, M.J.; Yuan, Z.; Chen, Y. Hierarchical Honeycomb Graphene Aerogels Reinforced by Carbon Nanotubes with Multifunctional Mechanical and Electrical Properties. *Carbon N Y* **2021**, *175*, doi:10.1016/j.carbon.2021.01.002.

62. Xing, S.; Ji, Q.; Jiao, X.; Chen, D. A Two-Step Route to SiO2 Nanofiber-Reinforced Aerogel Composites with Lightweight and High Temperature Resistance for Thermal Insulation. *ACS Appl Nano Mater* **2023**, *6*, doi:10.1021/acsanm.3c01940.

63. Chhetri, K.; Subedi, S.; Muthurasu, A.; Ko, T.H.; Dahal, B.; Kim, H.Y. A Review on Nanofiber Reinforced Aerogels for Energy Storage and Conversion Applications. *J Energy Storage* 2022, *46*.

64. Montes, S.; Maleki, H. Aerogels and Their Applications. In *Colloidal Metal Oxide Nanoparticles*; 2020.

65. Tokudome, Y.; Nakanishi, K.; Kanamori, K.; Fujita, K.; Akamatsu, H.; Hanada, T. Structural Characterization of Hierarchically Porous Alumina Aerogel and Xerogel Monoliths. *J Colloid Interface Sci* **2009**, *338*, doi:10.1016/j.jcis.2009.06.042.

66. Cai, B.; Sayevich, V.; Gaponik, N.; Eychmüller, A. Emerging Hierarchical Aerogels: Self-Assembly of Metal and Semiconductor Nanocrystals. *Advanced Materials* **2018**, *30*, doi:10.1002/adma.201707518.

67. Hofmann, A.; Marschall, R.; Voepel, P.; Rose, A.; Milow, B. Photocatalytic Activity and Electron Storage Capability of TiO 2 Aerogels with Adjustable Surface Area . *ECS Meeting Abstracts* **2023**, *MA2023-02*, doi:10.1149/ma2023-02472283mtgabs.

68. Ratke, L.; Hajduk, A. On the Size Effect of Gelation Kinetics in Rf Aerogels. *Gels* **2015**, *1*, doi:10.3390/gels1020276.

69. Ziff, R.M.; Ernst, M.H.; Hendriks, E.M. Kinetics of Gelation and Universality. *Journal of Physics A: General Physics* **1983**, *16*, doi:10.1088/0305-4470/16/10/026.

70. Jiang, Y.; Gang, H.; Benkun, M. Critical Property and Universality in the Generalized Smoluchovski Coagulation Equation. *Phys Rev B* **1990**, *41*, doi:10.1103/PhysRevB.41.9424.

71. Mellema, M.; Van Opheusden, J.H.J.; Van Vliet, T. Relating Colloidal Particle Interactions to Gel Structure Using Brownian Dynamics Simulations and the Fuchs Stability Ratio. *Journal of Chemical Physics* **1999**, *111*, doi:10.1063/1.479956.

72. Whittle, M.; Dickinson, E. Brownian Dynamics Simulation of Gelation in Soft Sphere Systems with Irreversible Bond Formation. *Mol Phys* **1997**, *90*, doi:10.1080/002689797172101.

73. Gelb, L.D. Simulating Silica Aerogels with a Coarse-Grained Flexible Model and Langevin Dynamics. *Journal of Physical Chemistry C* **2007**, *111*, doi:10.1021/jp0737505.

74. Ferreiro-Rangel, C.A.; Gelb, L.D. Investigation of the Bulk Modulus of Silica Aerogel Using Molecular Dynamics Simulations of a Coarse-Grained Model. *Journal of Physical Chemistry B* **2013**, *117*, 7095–7105, doi:10.1021/jp3128737.

75. Depta, P.N.; Gurikov, P.; Schroeter, B.; Forgács, A.; Kalmár, J.; Paul, G.; Marchese, L.; Heinrich, S.; Dosta, M. DEM-Based Approach for the Modeling of Gelation and Its Application to Alginate. *J Chem Inf Model* **2022**, *62*, doi:10.1021/acs.jcim.1c01076.

76. Martin, J.E.; Wilcoxon, J.; Adolf, D. Critical Exponents for the Sol-Gel Transition. *Phys Rev A (Coll Park)* **1987**, *36*, 1803–1810, doi:10.1103/PhysRevA.36.1803.

77. Hasmy, A. Aerogelation Process Simulation by a Cluster-Cluster Aggregation Algorithm. *J Solgel Sci Technol* **1999**, *15*, doi:10.1023/A:1008787421829.

78. Jullien, R.; Hasmy, A. Fluctuating Bond Aggregation: A Model for Chemical Gel Formation. *Phys Rev Lett* **1995**, *74*, doi:10.1103/PhysRevLett.74.4003.

79. Hasmy, A.; Primera, J.; Woignier, T. Cluster–Cluster Aggregation with Mobile Impurities. *J Solgel Sci Technol* **2019**, *90*, doi:10.1007/s10971-019-04918-3.

80. Pandit, P.; Abdusalamov, R.; Itskov, M.; Milow, B.; Rege, A. Data-driven Inverse Design and Optimisation of Silica Aerogel Model Networks. *PAMM* **2023**, *23*, doi:10.1002/pamm.202200329.

81. Hsieh, K.; Lallet, F.; Olivi-Tran, N. DLCA and Langevin Dynamics Approaches of Sol Gel Transition: A Comparison via the Fractal Dimension during Aggregation. *Fractals* **2008**, *16*, doi:10.1142/S0218348X08004071.

82. Abdusalamov, R.; Pandit, P.; Milow, B.; Itskov, M.; Rege, A. Machine Learning-Based Structure-Property Predictions in Silica Aerogels. *Soft Matter* **2021**, *17*, doi:10.1039/d1sm00307k.

83. Abdusalamov, R.; Pandit, P.; Itskov, M.; Milow, B.; Rege, A. Predictive Modeling and Simulation of Silica Aerogels by Using Aggregation Algorithms. *PAMM* **2021**, *21*, doi:10.1002/pamm.202100165.

84. Weitz, D.A.; Huang, J.S.; Lin, M.Y.; Sung, J. Dynamics of Diffusion-Limited Kinetic Aggregation. *Phys Rev Lett* **1984**, *53*, doi:10.1103/PhysRevLett.53.1657.

85. Borzęcka, N.H.; Kozłowska, I.; Gac, J.M.; Bojarska, M. Anti-Fouling Properties of Poly(Acrylic Acid) Grafted Ultrafiltration Membranes – Experimental and Theoretical Study. *Appl Surf Sci* **2019**, doi:10.1016/j.apsusc.2019.144658.

86. Abdusalamov, R.; Scherdel, C.; Itskov, M.; Milow, B.; Reichenauer, G.; Rege, A. Modeling and Simulation of the Aggregation and the Structural and Mechanical Properties of Silica Aerogels. *Journal of Physical Chemistry B* **2021**, *125*, doi:10.1021/acs.jpcb.0c10311.

87. Morales, R. V.; Da Cunha, C.R.; Rambo, C.R. A Complex Network Approach for the Growth of Aerogels. *Physica A: Statistical Mechanics and its Applications* **2014**, *406*, 131–138, doi:10.1016/j.physa.2014.03.058.

88. Bałdyga, J.; Tyl, G.; Bouaifi, M. Aggregation Efficiency of Amorphous Silica Nanoparticles. *Chem Eng Technol* **2019**, *42*, doi:10.1002/ceat.201900091.

89. Garofalini, S.H.; Martin, G. Molecular Simulations of the Polymerization of Silicic Acid Molecules and Network Formation. *Journal of physical chemistry* **1994**, *98*, doi:10.1021/j100055a044.

90. Pereira, J.C.G.; Catlow, C.R.A.; Price, G.D. Molecular Dynamics Simulation of Methanolic and Ethanolic Silica-Based Sol-Gel Solutions at Ambient Temperature and Pressure. *Journal of Physical Chemistry A* **2002**, *106*, doi:10.1021/jp010078h.

91. Elanany, M.; Selvam, P.; Yokosuka, T.; Takami, S.; Kubo, M.; Imamura, A.; Miyamoto, A. A Quantum Molecular Dynamics Simulation Study of the Initial Hydrolysis Step in Sol-Gel Process. *Journal of Physical Chemistry B* **2003**, *107*, doi:10.1021/jp026816z.

92. Thompson, A.P.; Aktulga, H.M.; Berger, R.; Bolintineanu, D.S.; Brown, W.M.; Crozier, P.S.; in 't Veld, P.J.; Kohlmeyer, A.; Moore, S.G.; Nguyen, T.D.; et al. LAMMPS - a Flexible Simulation Tool for Particle-Based Materials Modeling at the Atomic, Meso, and Continuum Scales. *Comput Phys Commun* **2022**, *271*, doi:10.1016/j.cpc.2021.108171.

93. Dosta, M.; Skorych, V. MUSEN: An Open-Source Framework for GPU-Accelerated DEM Simulations. *SoftwareX* **2020**, *12*, doi:10.1016/j.softx.2020.100618.

94. Aniszewska, D.; Rybaczuk, M. Mechanical Properties of Silica Aerogels Modelled by Movable Cellular Automata Simulations. *Mater Today Commun* **2021**, *27*, doi:10.1016/j.mtcomm.2021.102432.

95. Smolin, A.Y.; Shilko, E. V.; Astafurov, S. V.; Konovalenko, I.S.; Buyakova, S.P.; Psakhie, S.G. Modeling Mechanical Behaviors of Composites with Various Ratios of Matrix–Inclusion Properties Using Movable Cellular Automaton Method. *Defence Technology* **2015**, *11*, doi:10.1016/j.dt.2014.08.005.

96. Davies, C.H.J. Growth of Nuclei in a Cellular Automaton Simulation of Recrystallisation. *Scr Mater* **1997**, *36*, doi:10.1016/S1359-6462(96)00331-4.

97. Wessling, B. Cellular Automata Simulation of Dissipative Structure Formation in Heterogeneous Polymer Systems, Formation of Networks of a Dispersed Phase by Flocculation. *Journal de Physique II* **1996**, *6*, doi:10.1051/jp2:1996184.

98. Scalise, D.; Schulman, R. Emulating Cellular Automata in Chemical Reaction–Diffusion Networks. *Nat Comput* **2016**, *15*, doi:10.1007/s11047-015-9503-8.

99. El Rassy, H.; Pierre, A.C. NMR and IR Spectroscopy of Silica Aerogels with Different Hydrophobic Characteristics. *J Non Cryst Solids* **2005**, *351*, 1603–1610, doi:10.1016/j.jnoncrysol.2005.03.048.

100. Alam, T.M.; Assink, R.A.; Loy, D.A. Hydrolysis and Esterification in Organically Modified Alkoxysilanes: A 29Si NMR Investigation of Methyltrimethoxysilane†. *Chemistry of Materials* **1996**, *8*, 2366–2374, doi:10.1021/cm960183h.

101. Lázár, I.; Forgács, A.; Horváth, A.; Király, G.; Nagy, G.; Len, A.; Dudás, Z.; Papp, V.; Balogh, Z.; Moldován, K.; et al. Mechanism of Hydration of Biocompatible Silica-Casein Aerogels Probed by NMR and SANS Reveal Backbone Rigidity. *Appl Surf Sci* **2020**, *531*, 147232, doi:10.1016/j.apsusc.2020.147232.

102. Depla, A.; Lesthaeghe, D.; Van Erp, T.S.; Aerts, A.; Houthoofd, K.; Fan, F.; Li, C.; Van Speybroeck, V.; Waroquier, M.; Kirschhock, C.E.A.; et al. 29Si NMR and UV-Raman Investigation of Initial Oligomerization Reaction Pathways in Acid-Catalyzed Silica Sol-Gel Chemistry. *Journal of Physical Chemistry C* **2011**, *115*, 3562–3571, doi:10.1021/jp109901v.

103. Seddon, A.B.; Hunt, S.; Rourke, J.P.; Bruce, D.W. Cleavage of Silicon-carbon Bonds and Relative Rates of Hydrolysis of Ormosil Precursors for Optical Materials. *Advanced Materials for Optics and Electronics* **1994**, *4*, doi:10.1002/amo.860040408.

104. Shibayama, M.; Norisuye, T. Gel Formation Analyses by Dynamic Light Scattering. *Bull Chem Soc Jpn* **2002**, *75*, doi:10.1246/bcsj.75.641.

105. Ponton, A.; Warlus, S.; Griesmar, P. Rheological Study of the Sol-Gel Transition in Silica Alkoxides. *J Colloid Interface Sci* **2002**, *249*, doi:10.1006/jcis.2002.8227.

106. Ziff, R.M.; Hendriks, E.M.; Ernst, M.H. Critical Properties for Gelation: A Kinetic Approach. *Phys Rev Lett* **1982**, *49*, doi:10.1103/PhysRevLett.49.593.

107. Ziff, R.M.; Stell, G. Kinetics of Polymer Gelation. *J Chem Phys* **1980**, *73*, doi:10.1063/1.440502.

108. Gelb, L.D. Simulation and Modeling of Aerogels Using Atomistic and Mesoscale Methods. In *Aerogels Handbook*; 2011.

109. Šefčík, J.; McCormick, A. V. Kinetic and Thermodynamic Issues in the Early Stages of Sol-Gel Processes Using Silicon Alkoxides. *Catal Today* **1997**, *35*, doi:10.1016/S0920-5861(96)00158-7.

110. Venkateswara Rao, A.; Bhagat, S.D.; Hirashima, H.; Pajonk, G.M. Synthesis of Flexible Silica Aerogels Using Methyltrimethoxysilane (MTMS) Precursor. *J Colloid Interface Sci* **2006**, doi:10.1016/j.jcis.2006.03.044.

111. Luo, Y.; Li, Z.; Zhang, W.; Yan, H.; Wang, Y.; Li, M.; Liu, Q. Rapid Synthesis and Characterization of Ambient Pressure Dried Monolithic Silica Aerogels in Ethanol/Water Co-Solvent System. *J Non Cryst Solids* **2019**, *503–504*, doi:10.1016/j.jnoncrysol.2018.09.049.

112. Boonstra, A.H.; Bernards, T.N.M. The Dependence of the Gelation Time on the Hydrolysis Time in a Two-Step SiO2 Sol-Gel Process. *J Non Cryst Solids* **1988**, doi:10.1016/0022-3093(88)90309-2.

113. Taylor, S.J.; Haw, M.D.; Sefcik, J.; Fletcher, A.J. Monitoring the Gelation Mechanism of Resorcinol-Formaldehyde Gels by Dynamic Light Scattering. *Langmuir* **2014**, doi:10.1021/la502394u.

114. Gaca, K.Z.; Sefcik, J. Mechanism and Kinetics of Nanostructure Evolution during Early Stages of Resorcinol-Formaldehyde Polymerisation. *J Colloid Interface Sci* **2013**, doi:10.1016/j.jcis.2013.05.062.

115. Borzęcka, N.H.; Nowak, B.; Gac, J.M.; Głaz, T.; Bojarska, M. Kinetics of MTMS-Based Aerogel Formation by the Sol-Gel Method - Experimental Results and Theoretical Description. *J Non Cryst Solids* **2020**, *547*, 120310, doi:10.1016/j.jnoncrysol.2020.120310.

116. Ehgartner, C.R.; Grandl, S.; Feinle, A.; Hüsing, N. Flexible Organofunctional Aerogels. *Dalton Transactions* **2017**, *46*, doi:10.1039/c7dt00558j.

117. Kanamori, K.; Ueoka, R.; Kakegawa, T.; Shimizu, T.; Nakanishi, K. Hybrid Silicone Aerogels toward Unusual Flexibility, Functionality, and Extended Applications. *J Solgel Sci Technol* **2019**, *89*, doi:10.1007/s10971-018-4804-x.

118. Matias, T.; Varino, C.; de Sousa, H.C.; Braga, M.E.M.; Portugal, A.; Coelho, J.F.J.; Durães, L. Novel Flexible, Hybrid Aerogels with Vinyl- and Methyltrimethoxysilane in the Underlying Silica Structure. *J Mater Sci* **2016**, *51*, doi:10.1007/s10853-016-9965-9.

119. Guo, T.; Yun, S.; Li, Y.; Chen, Z.; Cao, C.; Gao, Y. Facile Synthesis of Highly Flexible Polymethylsilsesquioxane Aerogel Monoliths with Low Density, Low Thermal Conductivity and Superhydrophobicity. *Vacuum* **2020**, 109825, doi:10.1016/j.vacuum.2020.109825.

120. Perry, R.H.; Green, D.W. Perry's Chemical Engineering Handbook. *Perrys' chemical engineers' handbook* **2008**.

121. Borzęcka, N.H.; Nowak, B.; Pakuła, R.; Przewodzki, R.; Gac, J.M. Diffusion/Reaction Limited Aggregation Approach for Microstructure Evolution and Condensation Kinetics during Synthesis of Silica-Based Alcogels. *Int J Mol Sci* **2023**, *24*, doi:10.3390/ijms24031999.

122. Borzęcka, N.H.; Nowak, B.; Pakuła, R.; Przewodzki, R.; Gac, J.M. Cellular Automata Modeling of Silica Aerogel Condensation Kinetics. *Gels* **2021**, *7*, doi:10.3390/gels7020050.

123. Ponton, A.; Warlus, S.; Griesmar, P. Rheological Study of the Sol-Gel Transition in Silica Alkoxides. *J Colloid Interface Sci* **2002**, *249*, 209–216, doi:10.1006/jcis.2002.8227.

124. Innocenzi, P. *Measuring the Sol to Gel Transition*; 2019; ISBN 9783030200299.

12. ATTACHMENTS

List of the attachments:

- Attachment A1 - Synthesis recipes for TD-M1
- Attachment A2 - Synthesis recipes for TD-M2, TD-V and TD-D systems
- Attachment A3 - Porosity and volume shrinkage (TD-M1)
- Attachment A4 - The polydispersity index and mean diameter of SP (TD-M1)
- Attachment A5 - The mean size of secondary particles for TD-M2 system and TD-V system
- Attachment A6 - The polydispersity index for secondary particles for TD-M2 system and TD-V system
- Attachment A7 - TD-M2 kinetics curves
- Attachment A8 - TD-V kinetics curves
- Attachment A9 - TD-D kinetics curves
- Attachment A10 - Values of maximum condensation rate for MTMS and VTMS based gels
- Attachment A11 - Values of t_1 for MTMS and VTMS based gels
- Attachment A12 - Values of t_2 for MTMS and VTMS based gels

Attachment A1

Synthesis recipes for TD-M1:

Sample denotation	vol. fractions of the main components of a ternary system [-]				synthesis results*
	precursor	methanol (solvent)	water (anti-solvent)		
			aq. oxalic acid 0.01M	aq. ammonia solution 1M	
TD-M1-1	0.100	0.100	0.400	0.400	p
TD-M1-2	0.100	0.200	0.350	0.350	p
TD-M1-3	0.100	0.300	0.300	0.300	p
TD-M1-4	0.100	0.400	0.250	0.250	p
TD-M1-5	0.100	0.500	0.200	0.200	p
TD-M1-6	0.100	0.600	0.150	0.150	p
TD-M1-7	0.100	0.700	0.100	0.100	p
TD-M1-8	0.100	0.800	0.050	0.050	p
TD-M1-9	0.130	0.330	0.270	0.270	m
TD-M1-10	0.130	0.530	0.170	0.170	m
TD-M1-11	0.175	0.075	0.375	0.375	p/mrf
TD-M1-12	0.200	0.100	0.350	0.350	m
TD-M1-13	0.200	0.200	0.300	0.300	p/mrf
TD-M1-14	0.200	0.300	0.250	0.250	m
TD-M1-15	0.200	0.400	0.200	0.200	m
TD-M1-16	0.200	0.500	0.150	0.150	m
TD-M1-17	0.200	0.600	0.100	0.100	m
TD-M1-18	0.200	0.700	0.050	0.050	p/mrf
TD-M1-19	0.230	0.130	0.320	0.320	m
TD-M1-20	0.230	0.430	0.170	0.170	m
TD-M1-21	0.250	0.575	0.088	0.088	m
TD-M1-22	0.275	0.275	0.225	0.225	m
TD-M1-23	0.300	0.100	0.300	0.300	m
TD-M1-24	0.300	0.200	0.250	0.250	m
TD-M1-25	0.300	0.300	0.200	0.200	m
TD-M1-26	0.300	0.400	0.150	0.150	m
TD-M1-27	0.300	0.500	0.100	0.100	m
TD-M1-28	0.300	0.600	0.050	0.050	m
TD-M1-29	0.330	0.330	0.170	0.170	m
TD-M1-30	0.400	0.100	0.250	0.250	m
TD-M1-31	0.400	0.200	0.200	0.200	m
TD-M1-32	0.400	0.300	0.150	0.150	m
TD-M1-33	0.400	0.400	0.100	0.100	m
TD-M1-34	0.400	0.500	0.050	0.050	m
TD-M1-35	0.475	0.075	0.225	0.225	m
TD-M1-36	0.500	0.100	0.200	0.200	m
TD-M1-37	0.500	0.200	0.150	0.150	m
TD-M1-38	0.500	0.300	0.100	0.100	m
TD-M1-39	0.500	0.400	0.050	0.050	m
TD-M1-40	0.600	0.100	0.150	0.150	m
TD-M1-41	0.600	0.200	0.100	0.100	m
TD-M1-42	0.600	0.300	0.050	0.050	m
TD-M1-43	0.650	0.100	0.125	0.125	m
TD-M1-44	0.675	0.150	0.088	0.088	m
TD-M1-45	0.700	0.100	0.100	0.100	m
TD-M1-46	0.700	0.200	0.050	0.050	m
TD-M1-47	0.725	0.050	0.113	0.113	m

TD-M1-48	0.750	0.100	0.075	0.075	m
TD-M1-49	0.800	0.100	0.050	0.050	m

**p - precipitation, x - no condensation, mrf - macroscopic phase separation (or not interlinked gel), m - monolith, r - raisin*

Attachment A2

Synthesis recipes for TD-M2, TD-V and TD-D systems:

Sample denotation	mass fractions of the main components of a ternary system [-]			additives concentrations [M]			comments on the reaction results		
	precursor(s)	methanol (solvent)	water (anti-solvent)	oxalic acid	ammonia solution	*CTAB	TD-M2	TD-V	TD-D
							p - precipitation, x - no condensation, mrf - macroscopic phase separation (or not interlinked gel), m - monolith, r - raisin		
1	0.09	0.1	0.81	0.002	0.904	0.0915	p	p	p
2	0.18	0.1	0.72			*	mrf	p	mrf
3	0.27	0.1	0.63				m	mrf	mrf
4	0.36	0.1	0.54				m	mrf	m
4.5*	0.41	0.1	0.50				m	-	-
5	0.45	0.1	0.45				m	m	m
6	0.54	0.1	0.36				m	m	m
7	0.63	0.1	0.27				m	m	m
8	0.72	0.1	0.18				m	m	mrf
8.5*	0.77	0.1	0.14				m	-	-
9	0.81	0.1	0.09				x	x	r
10	0.08	0.2	0.72				p	p	p
11	0.16	0.2	0.64				m	p	mrf
12	0.24	0.2	0.56				m	mrf	mrf
13	0.32	0.2	0.48				m	m	m
13.5*	0.36	0.2	0.44				m	-	-
14	0.40	0.2	0.40				m	m	m
15	0.48	0.2	0.32				m	m	m
16	0.56	0.2	0.24				m	m	m
17	0.64	0.2	0.16				m	m	m
17.5*	0.68	0.2	0.12				m	-	-
18	0.72	0.2	0.08				p	x	r
19	0.07	0.3	0.63				p	p	p
20	0.14	0.3	0.56				m	p	m
21	0.21	0.3	0.49				m	mrf	m
22	0.28	0.3	0.42				m	m	m
22.5*	0.32	0.3	0.39				m	-	-
23	0.35	0.3	0.35				m	m	m
24	0.42	0.3	0.28				m	m	m
25	0.49	0.3	0.21				m	m	m
26	0.56	0.3	0.14				m	m	mrf
26.5*	0.60	0.3	0.11				m	-	-
27	0.63	0.3	0.07				x	x	r
28	0.06	0.4	0.54				p	p	mrf
29	0.12	0.4	0.48				mrf	p	m
30	0.18	0.4	0.42				m	mrf	m
31	0.24	0.4	0.36				m	m	m
31.5*	0.27	0.4	0.33				m	-	-
32	0.30	0.4	0.30				m	m	m
33	0.36	0.4	0.24				m	m	m
34	0.42	0.4	0.18				m	m	m
35	0.48	0.4	0.12				m	m	mrf
35.5*	0.51	0.4	0.09				m	-	-
36	0.54	0.4	0.06				x	x	r
37	0.05	0.5	0.45				p	p	-

38	0.10	0.5	0.40	mrf	p	-
39	0.15	0.5	0.35	m	mrf	-
40	0.20	0.5	0.30	m	m	-
40.5*	0.23	0.5	0.28	m	-	-
41	0.25	0.5	0.25	m	m	-
42	0.30	0.5	0.20	m	m	-
43	0.35	0.5	0.15	m	m	-
44	0.40	0.5	0.10	m	m	-
44.5*	0.43	0.5	0.08	m	-	-
45	0.45	0.5	0.05	x	-	-
46	0.04	0.6	0.36	p	p	-
47	0.08	0.6	0.32	p	p	-
48	0.12	0.6	0.28	mrf	mrf	-
49	0.16	0.6	0.24	mrf	mrf	-
50	0.20	0.6	0.20	m	m	-
51	0.24	0.6	0.16	m	m	-
52	0.28	0.6	0.12	m	m	-
53	0.32	0.6	0.08	m	m	-
54	0.36	0.6	0.04	x	-	-
55	0.03	0.7	0.27	p	p	-
56	0.06	0.7	0.24	p	o	-
57	0.09	0.7	0.21	p	mrf	-
58	0.12	0.7	0.18	mrf	m	-
59	0.15	0.7	0.15	m	mrf	-
60	0.18	0.7	0.12	m	mrf	-
61	0.21	0.7	0.09	m	mrf	-
62	0.24	0.7	0.06	p	mrf	-

**p - precipitation, x - no condensation, mrf - macroscopic phase separation (or not interlinked gel), m - monolith, r - raisin*

Attachment A3

Porosity and volume shrinkage (TD-M1):

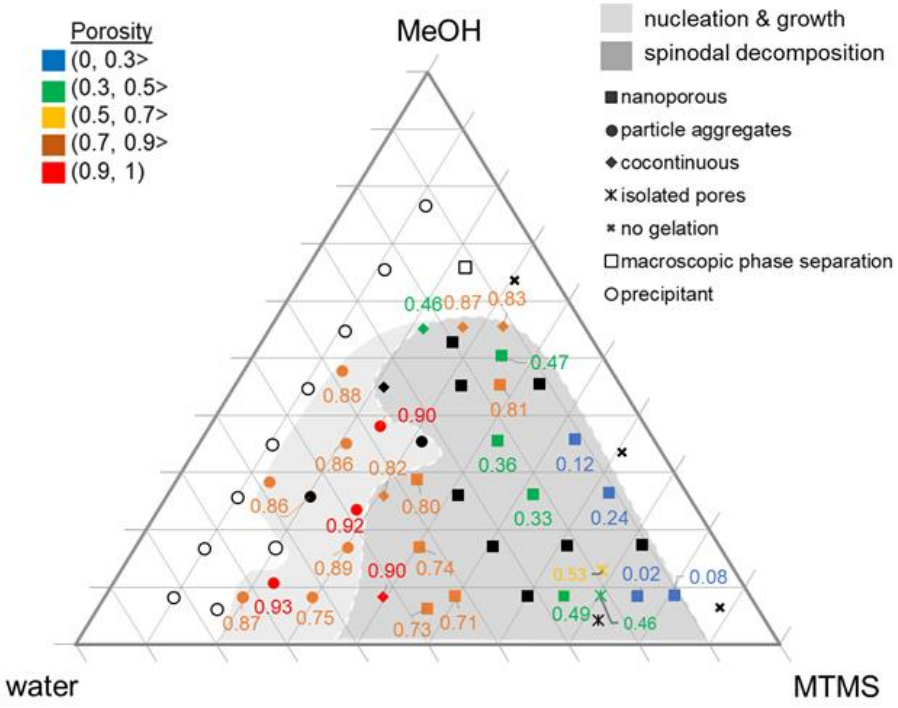

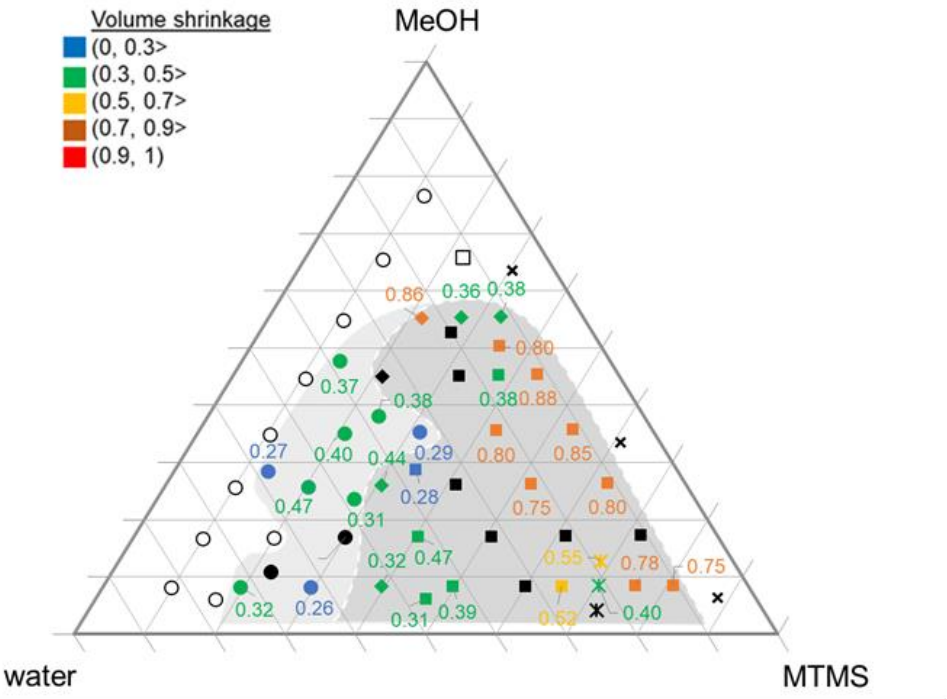

Attachment A4

The polydispersity index (upper) and mean diameter of SP (bottom) (TD-M1):

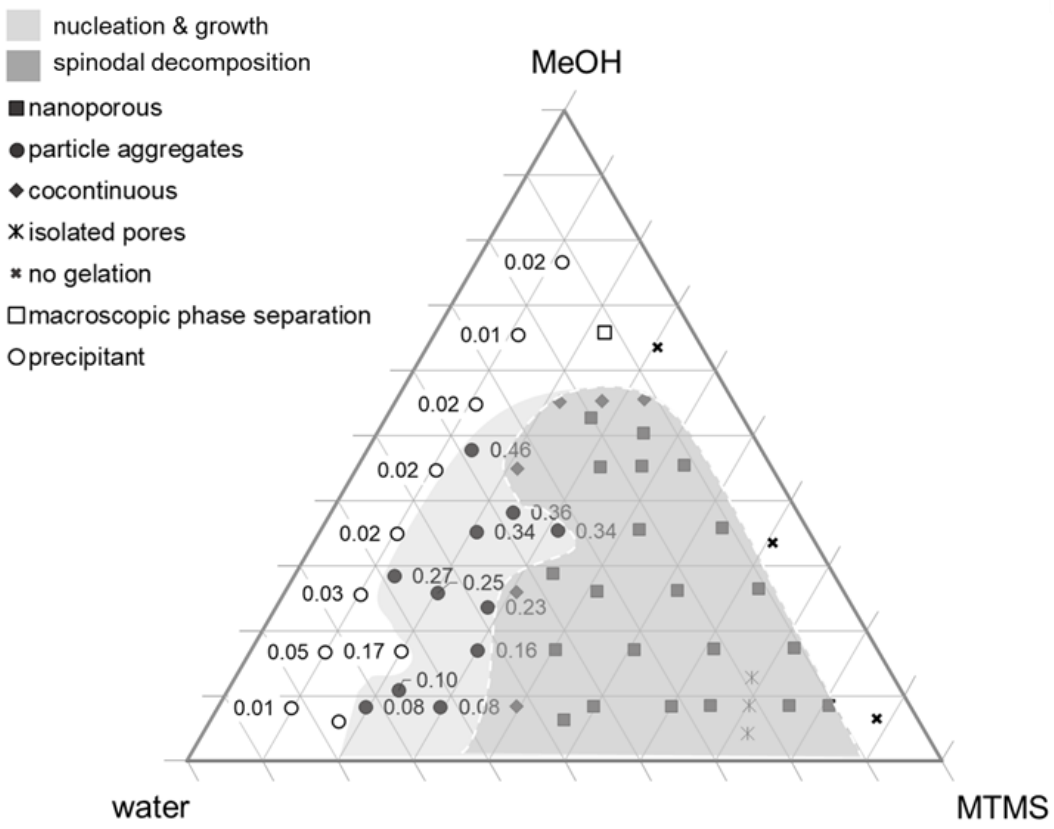

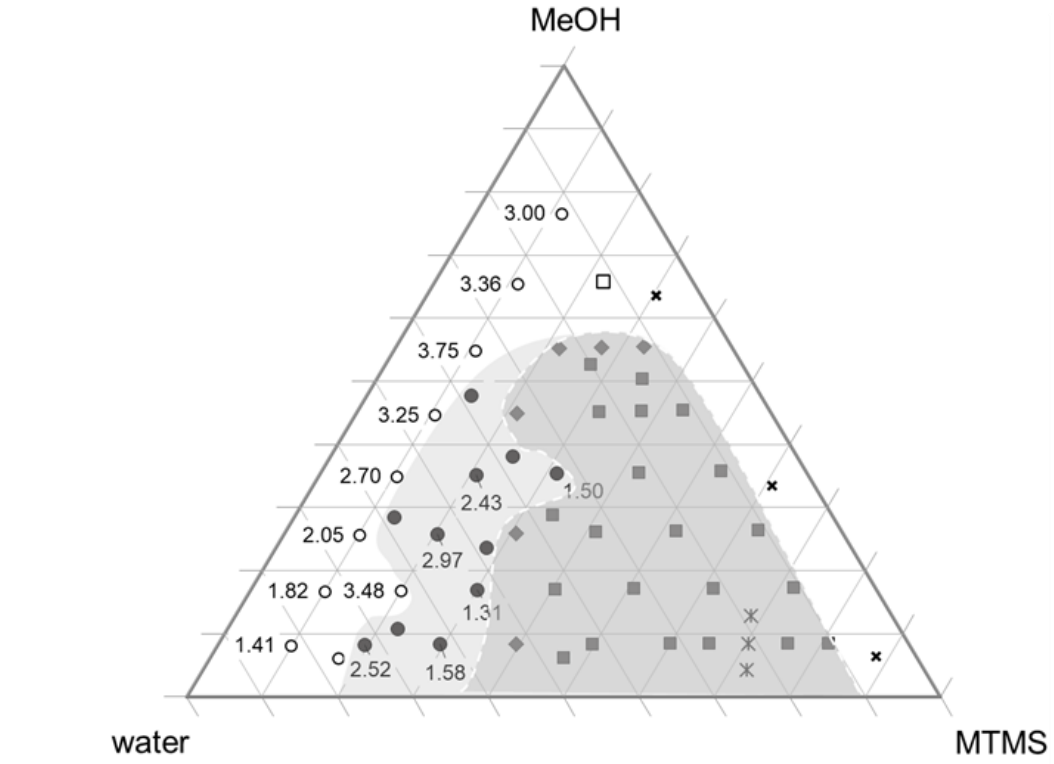

Attachment A5

The mean size of secondary particles for TD-M2 system (upper) and TD-V system (bottom):

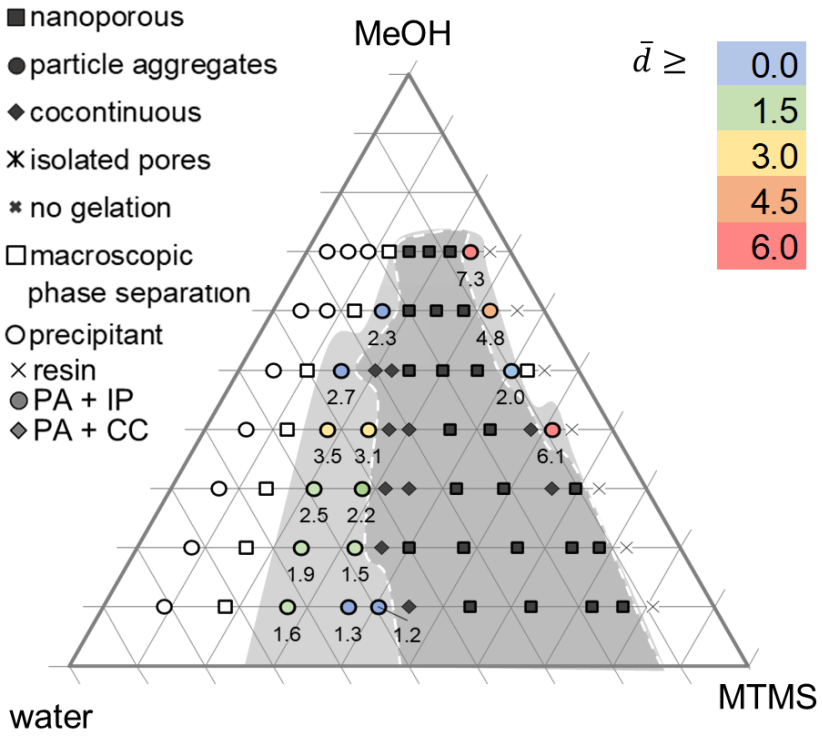

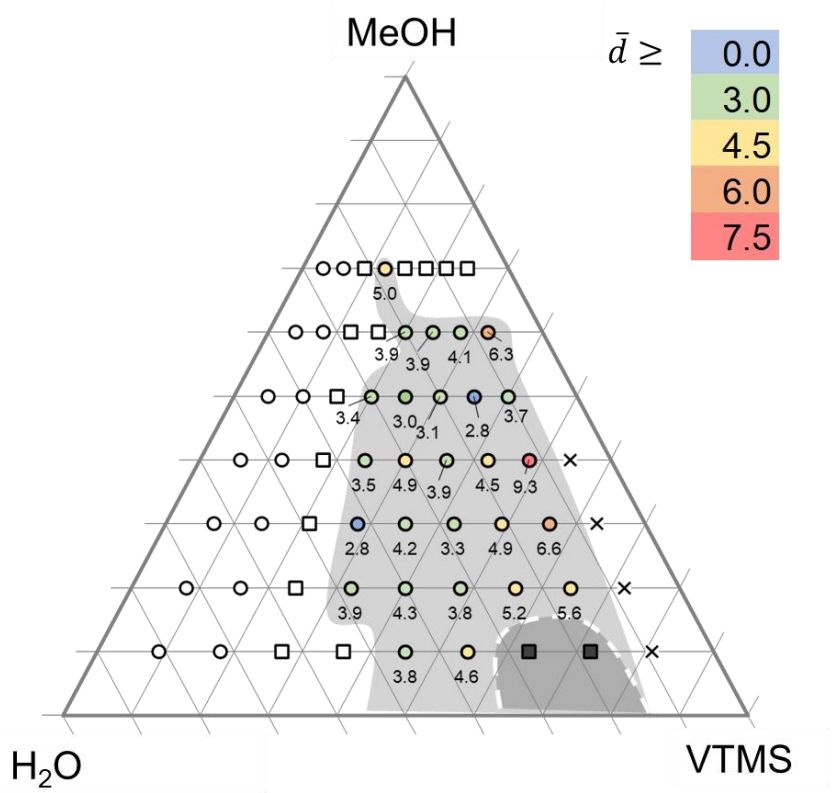

Attachment A6

The polydispersity index for secondary particles for TD-M2 system (upper) and TD-V system (bottom):

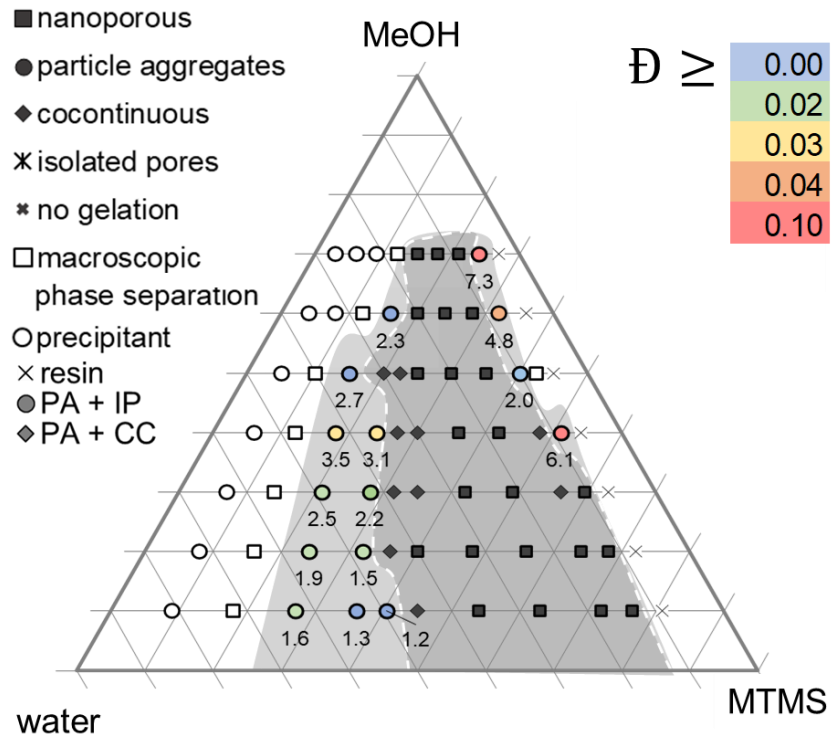

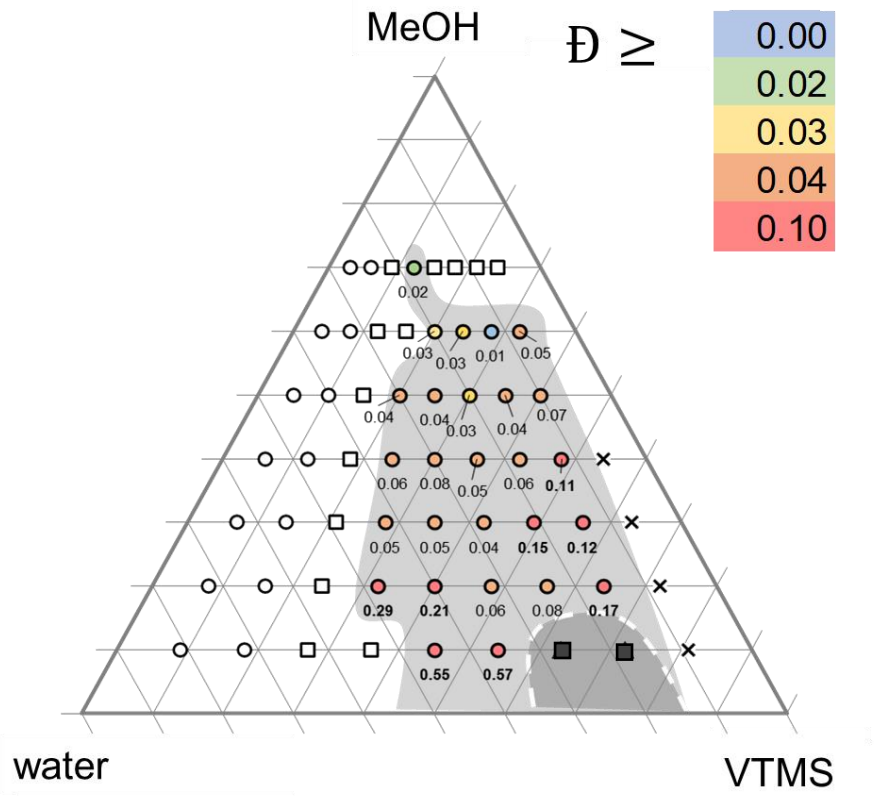

Attachment A7

TD-M2 kinetics curves:

MeOH=10%$_{mas}$

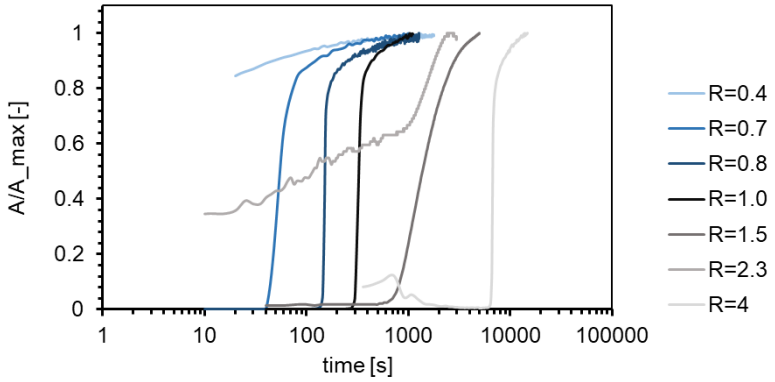

MeOH=20%$_{mas}$

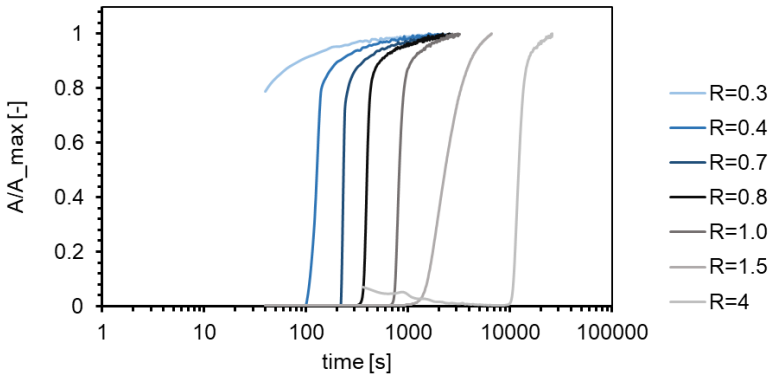

MeOH=30%$_{mas}$

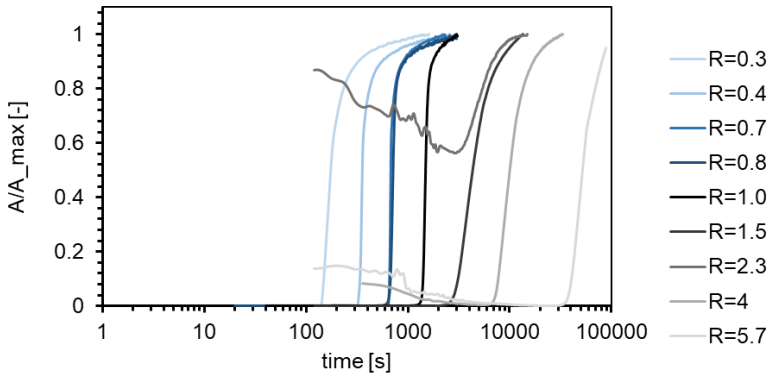

MeOH=40%$_{mas}$

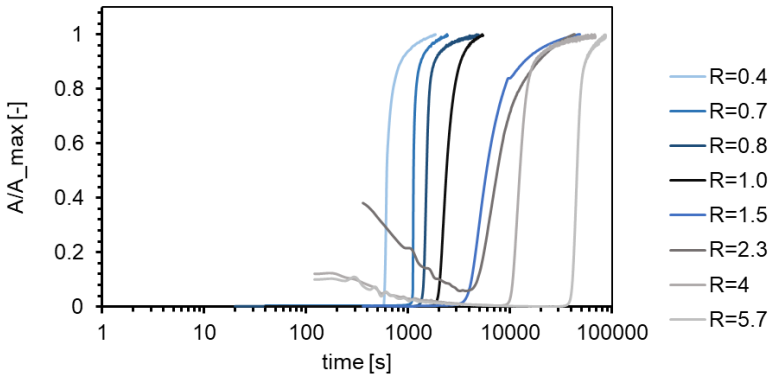

MeOH=50%$_{mas}$

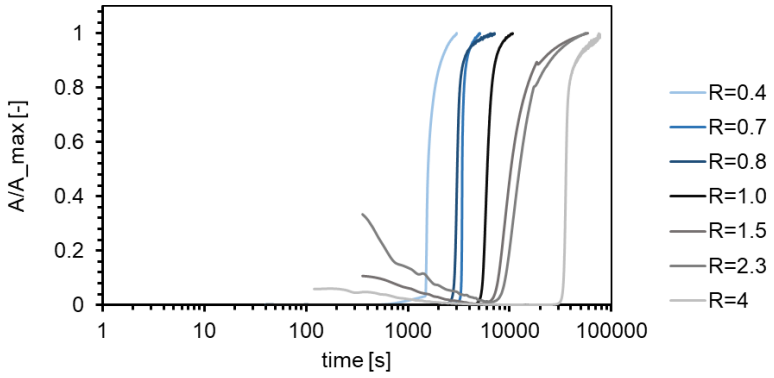

MeOH=60%$_{mas}$

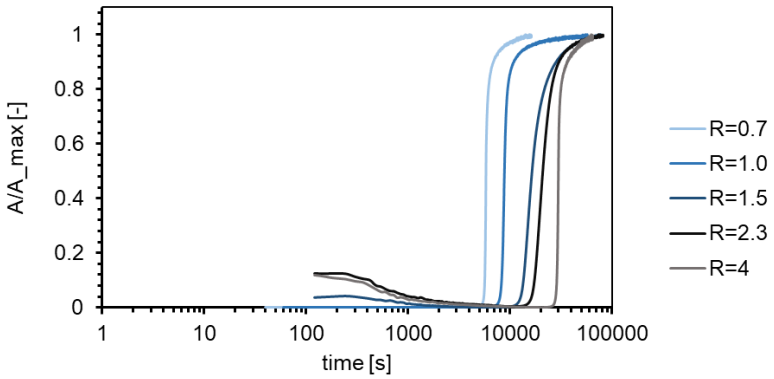

MeOH=70%$_{mas}$

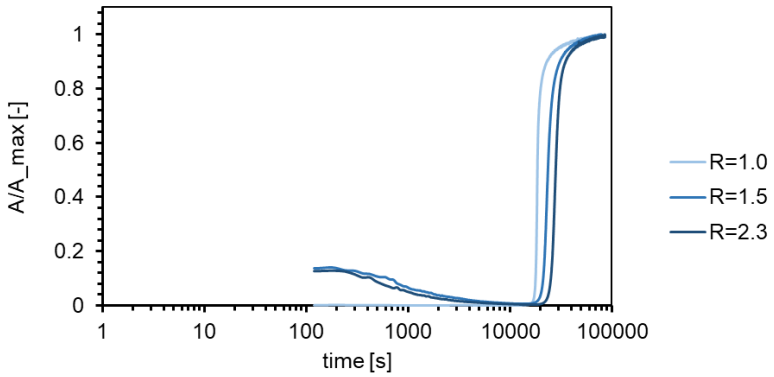

Attachment A8

TD-V kinetics curves:

MeOH = 10%$_{mas}$

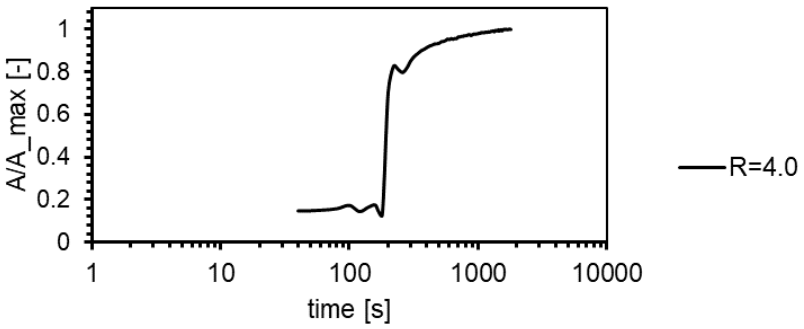

MeOH = 20%$_{mas}$

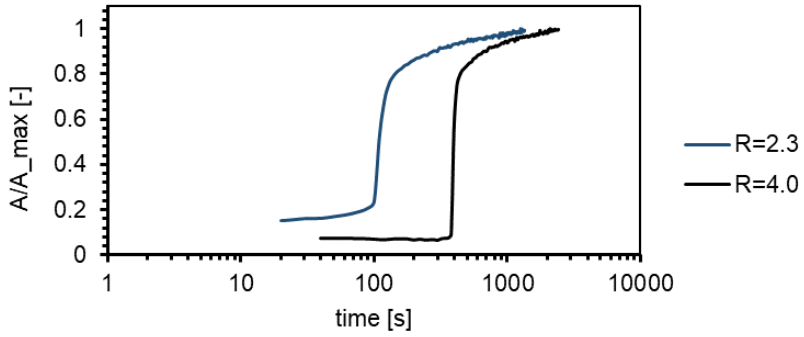

MeOH = 30%$_{mas}$

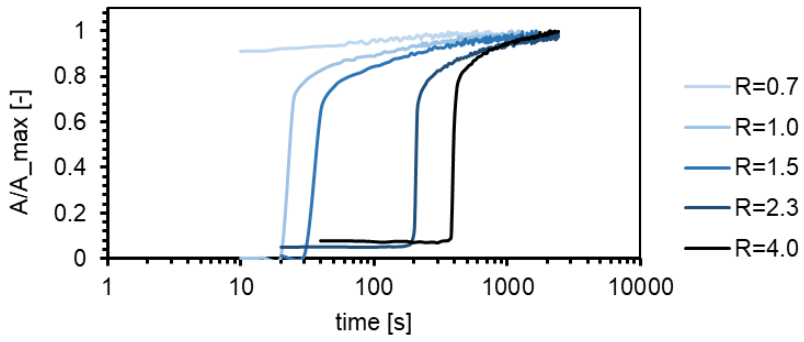

MeOH = 40%$_{mas}$

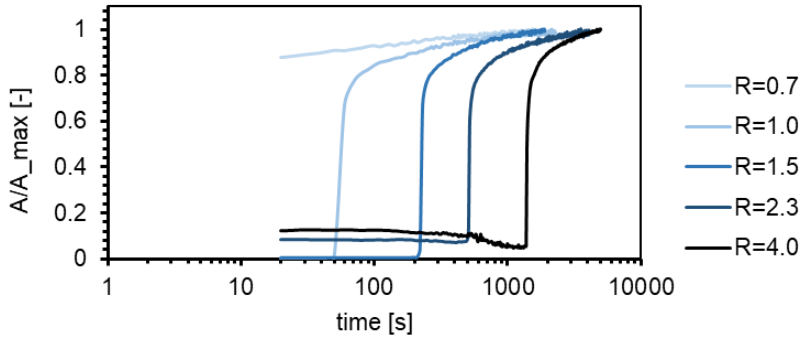

MeOH = 50%$_{mas}$

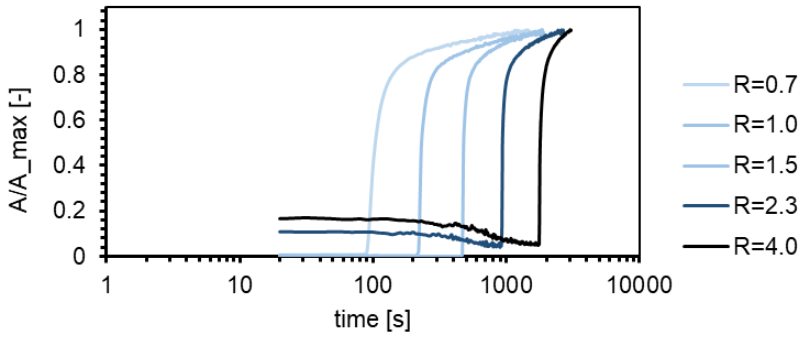

MeOH = 60%$_{mas}$

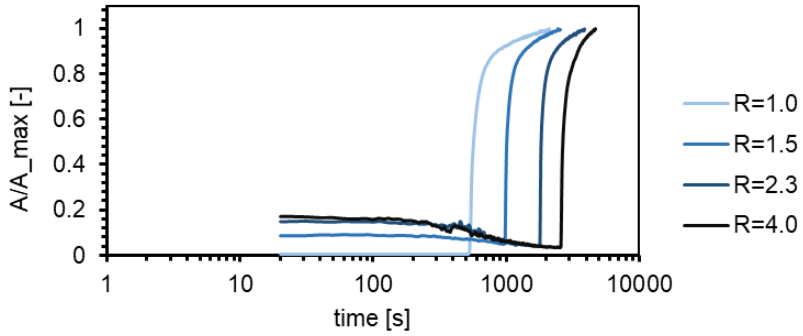

Attachment A9

TD-D kinetics curves:

MeOH = 10%$_{mas}$

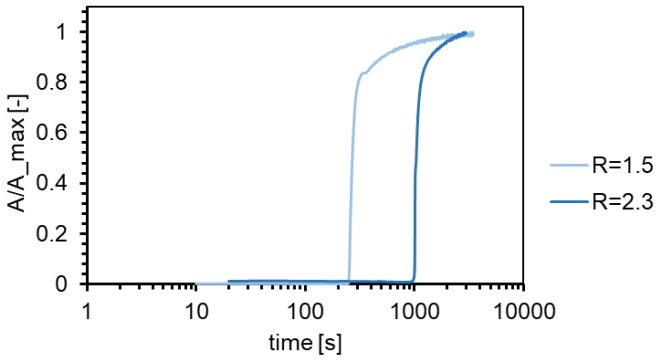

MeOH = 20%$_{mas}$

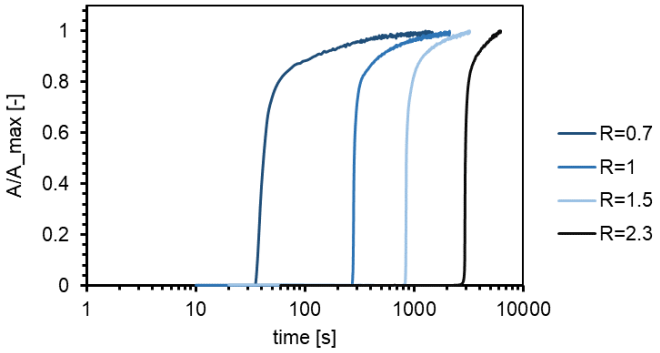

MeOH = 30%$_{mas}$

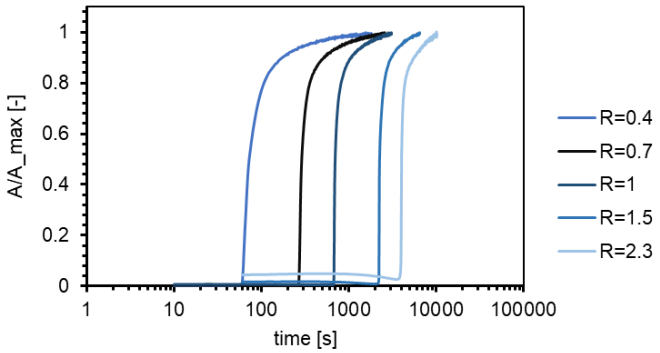

MeOH = 40%$_{mas}$

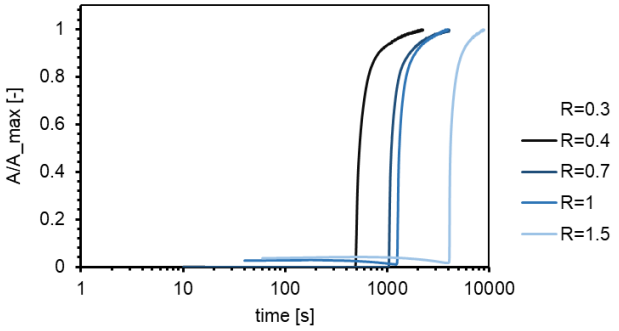

Attachment A10

Values of maximum condensation rate for MTMS based gels (for the readability, the binodal and spinodal area were omitted in the graphs below):

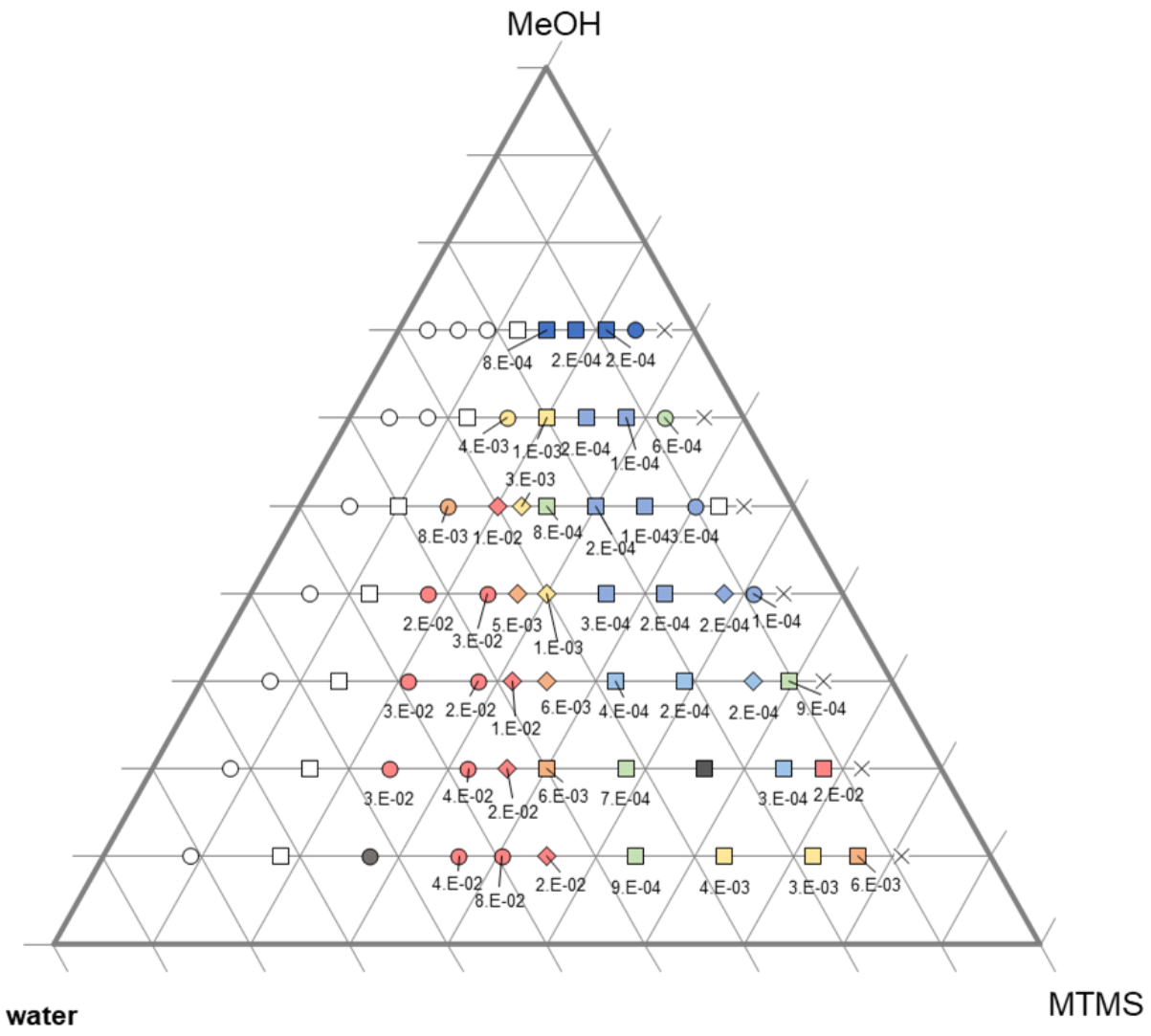

Values of maximum condensation rate for MTMS and VTMS based gels (for the readability, the binodal and spinodal area were omitted in the graphs below):

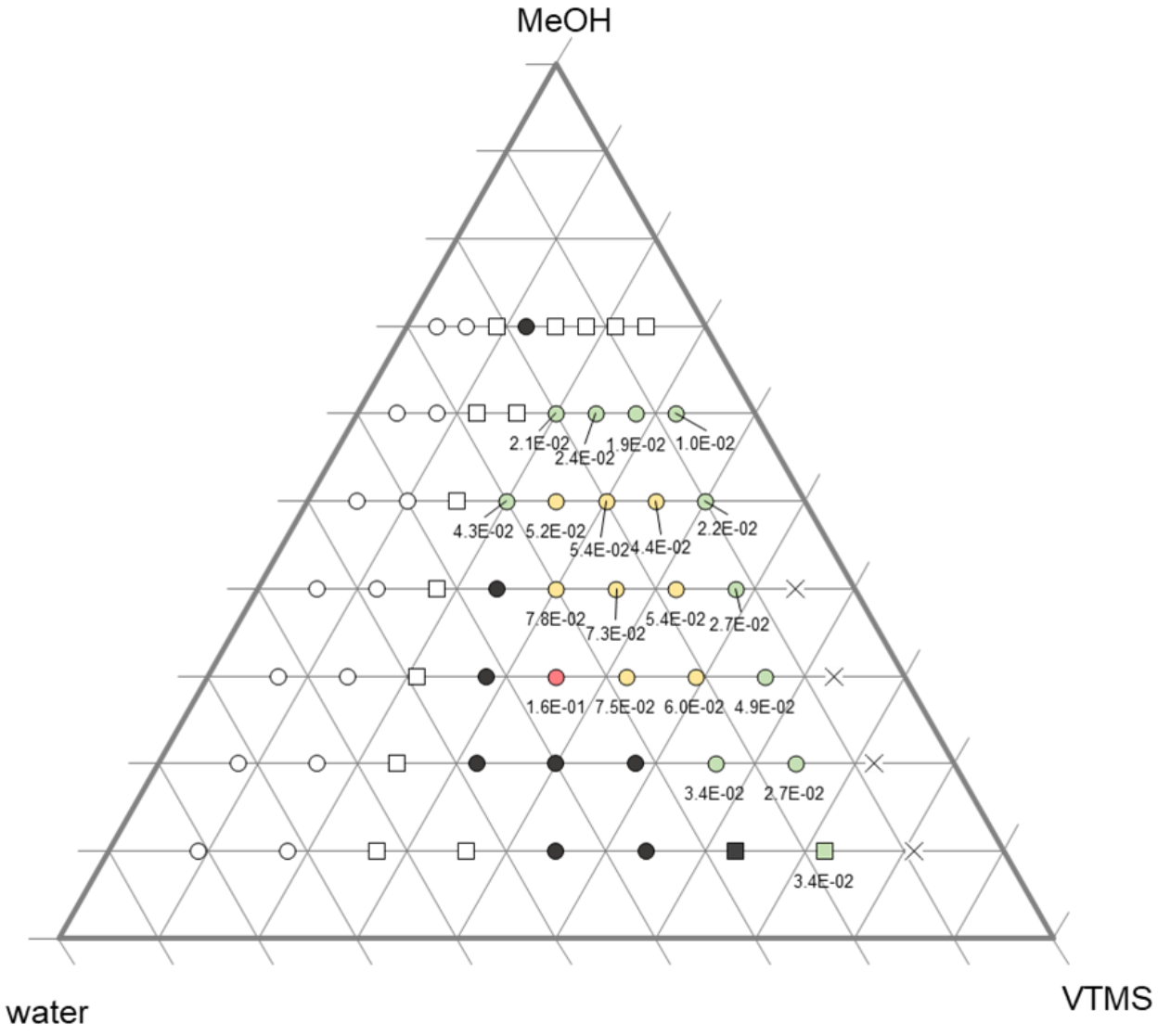

Attachment A11

Values of t_1 for MTMS based gels (for the readability, the binodal and spinodal area were omitted in the graphs below):

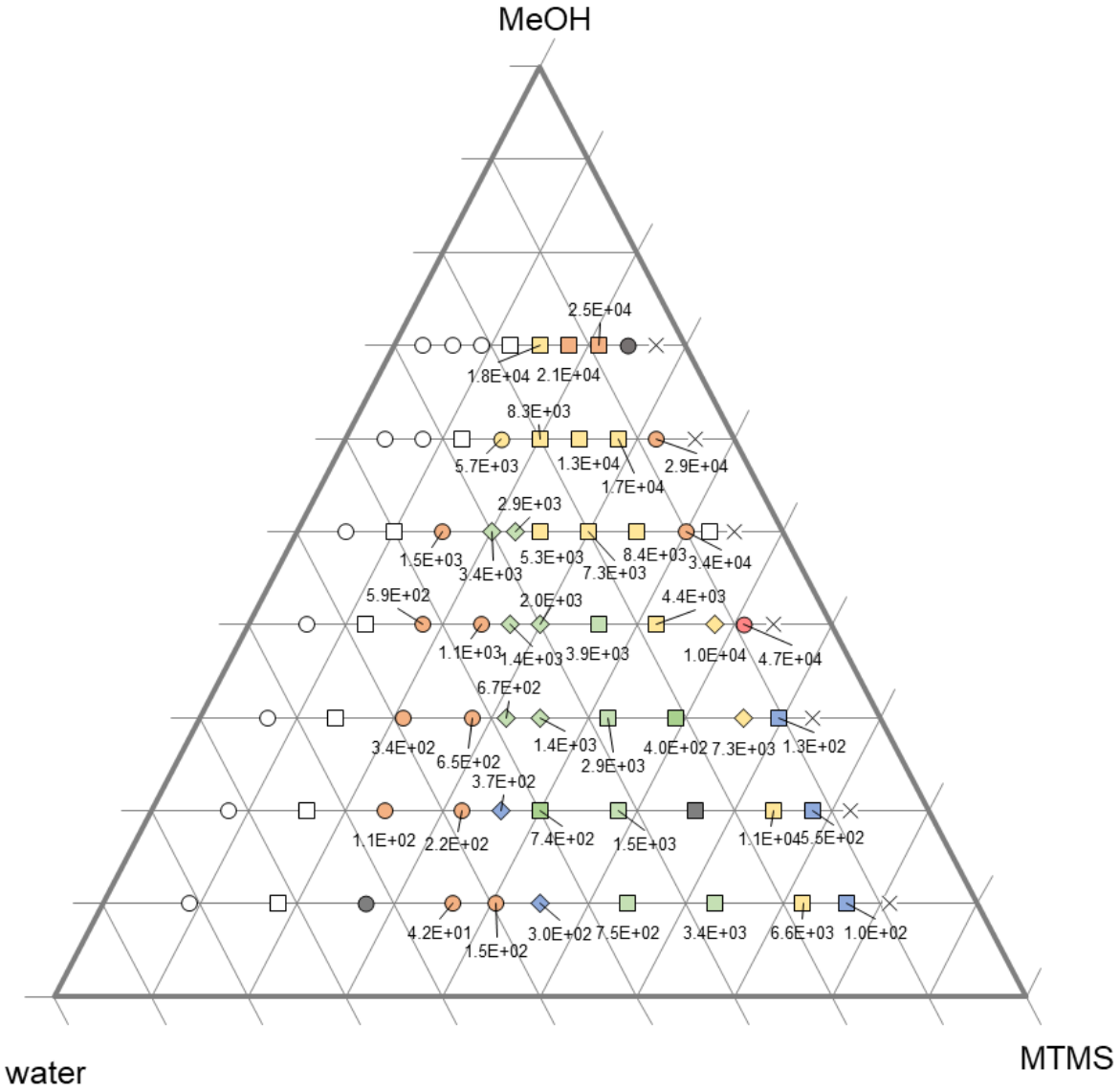

Values of t_1 for VTMS based gels (for the readability, the binodal and spinodal area were omitted in the graphs below)

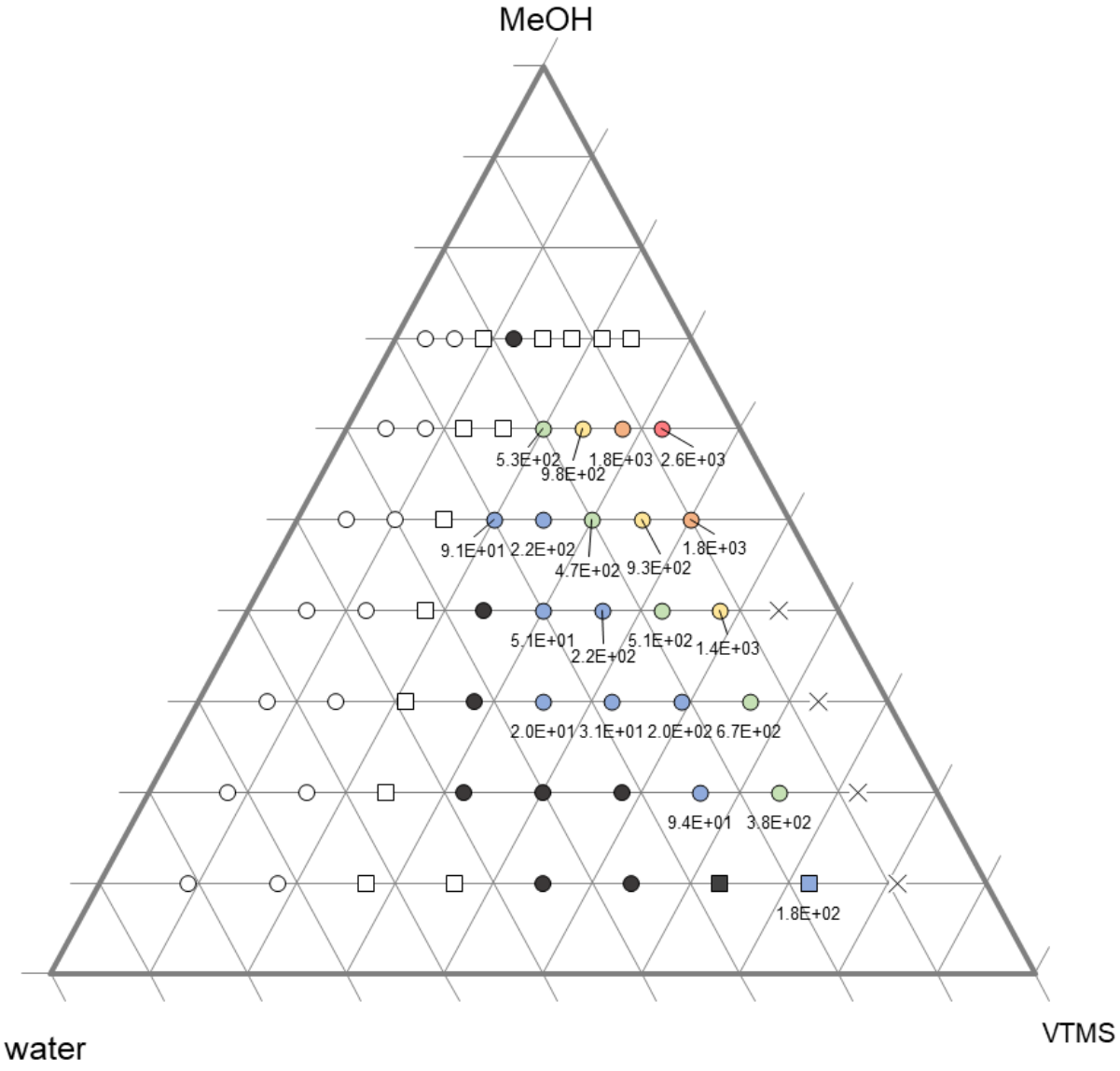

Attachment A12

Values of t_2 for MTMS based gels (for the readability, the binodal and spinodal area were omitted in the graphs below)

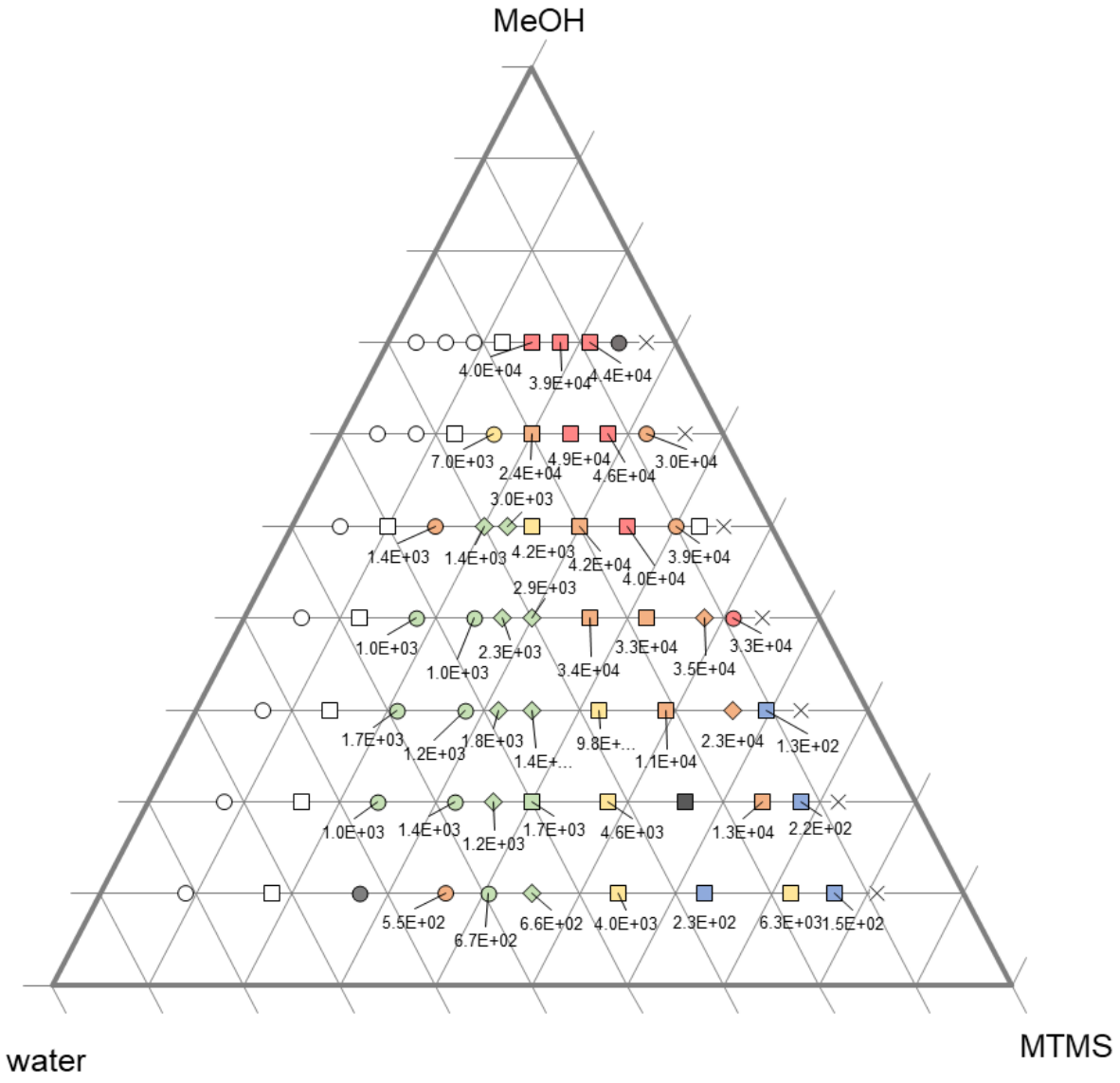

Values of t_2 for VTMS based gels (for the readability, the binodal and spinodal area were omitted in the graphs below)